UNIVERSITY OF CALIFORNIA,
IRVINE

Carbon Nanotube and Graphene Biosensing with Liquid Potential Control

DISSERTATION

submitted in partial satisfaction of the requirements
for the degree of

DOCTOR OF PHILOSOPHY

in Physics

by

Jeffrey Jae Taulbee

Dissertation Committee:
Professor Philip G. Collins, Chair
Professor Zuzanna Siwy, Ph. D.
Professor Javier Sanchez-Yamagishi, Ph. D.

2021

DEDICATION

To my father, Gary Taulbee.

TABLE OF CONTENTS

LIST OF FIGURES

LIST OF TABLES

LIST OF EQUATIONS

ACKNOWLEDGEMENTS

First and foremost, I thank Professor Philip Collins for his unwavering support and guidance throughout my Ph.D. journey. Over the past five years, I have undergone an immense amount of intellectual and professional growth, both of which he has been instrumental in. He has taught me the true meaning of focus and diligence. He has shown me how to learn from my shortcomings and that there is always room for improvement. He is never short of guidance and has always found a way to maximize my growth and success. I could not have envisioned a better graduate experience, and I am forever indebted to him for that.

Next, I thank the past members of the Collins research group for their contributions in making my work possible. Dr. Mackenzie Turvey, Dr. Calvin Lau, and Dr. Wonbae Lee have all played vital roles in my academic journey. Beyond fulfilling their duties as senior members, they have always gone above and beyond to provide the tools, knowledge, and support I have needed to achieve success. Through our shared journey in the Collins Lab, we have built a longstanding camaraderie that I hold dearly. Without them, I would not be the scientist that I am today.

I thank Professor Gregory Weiss and the members of his research group here at UCI for their contributions in our collaborative work involving single-molecule biosensing. I thank Rebekah Dyer, Kristin Gabriel, and Cynthia Chen for their tireless preparation of enzymes and biological reagents that enabled our collaborative research. Specifically, I thank Kristin Gabriel for her insight and knowledge of biochemistry to supplement my understanding throughout our experimental studies.

I thank Dr. Brett Goldsmith and the entire Cardea organization for allowing me the opportunity to perform research as a part of their team. I thank Dr. Francie Barron, Dr. Yingning Gao and Ken Dickerson for providing a myriad of different approaches, broadening my thought process and abilities as a scientist. I am extremely grateful to have had the rare graduate experience of working in an industrial environment with scientists of diverse backgrounds.

I thank Jon Celesia and Mark Wong, who have both provided invaluable mentorship from the beginning of my academic journey in physics, pre-dating my college education. They supplied me with knowledge and opportunities that were not otherwise readily available. They effectively enabled my pursuit of this Ph.D., and none of this would have been possible without them.

I thank my family and friends for their support. Their unconditional support and encouragement have been the backbone to my Ph.D. They have always been able to instill excitement in me, even in times that I lacked the excitement myself.

Lastly, I thank my beautiful fiancée, Cari Tam, for her unconditional love and support throughout my Ph.D. I would not have been able to accomplish any of this without her by my side.

The work in Chapters 2 and 3 was made possible by funding from the NSF INTERN program. The work in Chapters 4 and 5 was funded by NIH.

CURRICULUM VITAE

Jeffrey Jae Taulbee

2014	B.S. in Physics, University of California, Los Angeles
2016-17	Teaching Assistant, University of California, Irvine
2017-21	Graduate Student Researcher, University of California, Irvine
2019	M.S. in Physics, University of California, Irvine
2019-20	NSF INTERN Program, Cardea, San Diego
2021	Ph.D. in Physics, University of California, Irvine

FIELD OF STUDY

Single-Molecule Biophysics, Carbon Nanotube Bioelectronics, Graphene Bioelectronics

---

PUBLICATIONS

Balderston, S., Taulbee, J., *et al.* Discrimination of single-point mutations in unamplified genomic DNA via Cas9 immobilized on a graphene field-effect transistor. *Nat. Biomed. Eng.* (2021).

POSTERS & PRESENTATIONS

Taulbee J., *et al.* "Single-Molecule Bioelectronics." Poster presented at Gordon Research Conference Bioelectronics, Andover, NH (2019).

Taulbee J., *et al.* "Distinguishing Catalytic and Noncatalytic Motions of Individual Taq Polymerase Molecules." Presented at APS March Meeting, Virtual (2021).

ABSTRACT OF THE DISSERTATION

Carbon Nanotube and Graphene Biosensing with Liquid Potential Control

By

Jeffrey Jae Taulbee

Doctor of Philosophy in Physics

University of California, Irvine, 2021

Professor Philip G. Collins, Chair

Bioelectronics is a rapidly expanding technology that has seen much success across the field of biosensing. This dissertation explores the biosensing application of graphene field-effect transistors (gFETs) and single-walled carbon nanotube field-effect transistors (SWCNT-FETs). Liquid potentials are methodically controlled throughout the experiments performed herein to demonstrate the importance of electrostatics in gFET sensor responses and biomolecular processes such as receptor-ligand binding and enzyme catalysis.

After a brief introduction to the field of biosensing and current methods, the dissertation is organized into two halves. Chapters 2 and 3 describe testing of a commercial gFET biosensor in a collaboration with Cardea, a startup company in San Diego, CA. Chapters 4 and 5 describe single-molecule measurements of Taq polymerase using SWCNT-FETs.

Two main experiments were completed with the gFET biosensors. First, Chapter 2 details measurements of interleukin-6 (IL-6) antibody-antigen binding. Measurements using externally applied liquid potentials ranging from -0.1 V to 0.4 V revealed that changes in source-drain current (I_{sd}) previously attributed to specific antibody-antigen binding were instead a result of electrochemical charging effects. After proper characterization and subtraction of electrochemical

charging signals, changes in I_{sd} due to antigen adsorption on the graphene surface were found to decrease monotonically from 0 % to -5 % with increasing applied potentials, indicating that applied liquid potentials play a critical role in sensor output signals and proper interpretation of those signals.

Chapter 3 describes the use of Cardea gFETs in the sensing of single-nucleotide polymorphisms (SNPs). This experiment involved immobilizing Cas9 molecules on gFET biosensors then incubating them with target-specific guide RNA (gRNA) related to sickle cell disease (SCD). When incubated with target genomic DNA, the gFET biosensor produced signals twice as large on average as when incubated with genomic DNA varying by a SNP, demonstrating successful discrimination between the two genomic DNA samples. Follow-up experiments instead using gRNA related to familial amyotrophic lateral sclerosis (fALS) achieved similar discrimination between genomic DNA varying by a SNP, as did experiments instead using a Cas9 orthologue from *Mycoplasma gallisepticum* (MgaCas9). These results establish Cardea's gFET biosensor as a viable platform for rapid and highly programmable SNP detection without the need for DNA amplification.

In the second half of this dissertation, SWCNT-FETs were used to study individual Taq polymerase molecules. Chapter 4 introduces the use of SWCNT-FETs as biosensors with experimental procedures, sample signals, and subsequent signal analysis methods specific to the study of Taq polymerase all contained therein. Various analyses confirmed the Poisson-like behavior of free-running Taq polymerase, with catalysis occurring at a rate of approximately 4 s^{-1} at T = 27 °C.

Chapter 5 expands on the study of Taq with additional external potentials. Taq only generated electrical signals in a narrow 200-mV range of liquid potentials, V_{lg}. Outside that

potential range, the devices became quiet. Follow-up experiments showed that Taq polymerase catalysis deviated from its Poisson-like behavior when subjected to time-varying potentials with one boundary lying within the active range of V_{lg} and the other outside. More specifically, when subjected to time-varying potentials, Taq generated signals that lasted longer, occurred more frequently, and less randomly than when subjected to time-independent potentials. These results indicate the importance of external potential control in single-molecule SWCNT-FET studies and provide evidence that external potentials can even be tuned to influence the timing of enzyme motions.

Chapter 1

Introduction

The utilization of physical sensors to better understand biological and chemical processes and interactions has been a fruitful multidisciplinary endeavor [1-3]. Over the past 60 years, biosensing research has contributed to everything from drug development and biomedicine to environmental monitoring [2,4,5]. Biosensing studies generally fall into one of two categories: ensemble studies and single-molecule studies.

Beginning with a brief overview of current methods in ensemble studies, a few of the most widely used techniques are surface plasmon resonance (SPR), enzyme-linked immunosorbent assays (ELISA) and solid-state transistor biosensors. SPR is an optical technique that measures changes at the surface of a planar material, such as molecular adsorption or receptor-ligand binding, via plasmon generation [6,7]. SPR-based sensors often allow for long measurement durations and label-free detection but may require expensive materials or complex procedures to achieve high detection specificity [4,6,7]. In an ELISA, an antigen is immobilized on a microplate and then complexed with an antibody that is linked to a reporter enzyme, which produces a measurable product, via fluorescence or chemiluminescence for example, upon incubation with substrates. ELISA is a versatile method with a wide range of customizability but often requires careful experimental design to avoid nonspecific signal and false positives. Additionally, the required use of antibodies in ELISA comes with additional concerns regarding reagent instability. Lastly, solid-state transistor biosensors, such as the graphene field-effect transistors used in the work of this dissertation, measure changes in electrical properties of solid-state transistor devices in response to biomolecular interactions [4,8-12].

Cardea, a small startup company in San Diego, California, has invented a solid-state transistor biosensor using graphene field-effect transistors (gFETs). Graphene has a unique 2D carbon nanostructure that can be functionalized using both covalent and noncovalent methods, which in combination with its large surface area, allow for a wide range of biosensing applications [10]. Studies have also shown that graphene is biocompatible with many biomolecules such as antibodies, enzymes, DNA, and proteins, depending on the graphene synthesis method [8,13-16]. The high sensitivity of graphene to electric fields makes it an ideal material for applications sensing charged biomolecules and biomolecular interactions [11,17]. Cardea's gFET biosensors also do not require expensive additional reagents or biomolecular labeling as in other techniques such as SPR, ELISA, and fluorescent methods [16].

Cardea continues to refine their technology and explore more applications of their gFET biosensor in ensemble studies. Recently, Cardea has realized wafer-scale production of their gFET biosensors and subsequently tested device performance in a commercial biosensing application involving interleukin-6 (IL-6) antibody-antigen binding [12]. However, these batch-processed gFET biosensors still suffer from an array of defects including polymer contamination and graphene tearing, which leads to device-to-device biosensing variation. Nonetheless, Cardea's gFET biosensors have been implemented in recent studies involving Zika virus detection and genomic DNA detection with CRISPR-Cas9 molecules and continue to find applications in ensemble biosensing [14,15].

One aspect of experiments using solid-state transistor biosensors, such as Cardea's gFET biosensors, that is often overlooked is the role of applied potentials. Biosensing experiments using solid-state transistors are performed in electrolytic solutions. The electrolytic solution also serves as the gate electrode for the transistor and involves control of the liquid potential. In general, sensor

response optimization requires proper tuning of liquid potential, which varies between devices. The entire liquid potential drop occurs over a few ion layers at the channel-liquid interface where biomolecules are generally immobilized. Therefore, the liquid potential strongly dictates the electrostatic environment immediately surrounding the biomolecules. The applied potentials may affect both biological and non-biological processes and therefore need careful consideration when interpreting biosensing signals.

The work described in the first half of this dissertation explored the device-to-device variation of Cardea's gFET biosensors by measuring sensor outputs under a variety of liquid potentials, which led to improved signal processing and analysis methods to reduce or eliminate the variation in biosensing signals. With a better understanding of device-to-device variation and improved signal analysis methods, additional work using Cardea's gFET biosensors expanded on the use of CRISPR-Cas9 molecules for successful detection of single-nucleotide polymorphisms (SNPs) in genomic DNA.

Contrary to ensemble studies, single-molecule studies provide more detailed information of individual molecules such as conformational dynamics or molecular substructure. There are a handful of effective methods throughout single-molecule science. Fluorescence methods, such as Förster resonance energy transfer (FRET), utilize light emission of fluorophores to study biomolecular interactions and processes via fluorophore-labeling, often to observe conformational motions at the single-molecule level [2,18]. FRET has a tradeoff between temporal resolution and measurement duration due to the photobleaching of fluorophores. Additionally, FRET generally involves fluorophore-labeling of biomolecules, which must be carefully selected to not interfere with biomolecular function. Probe and tunneling microscopy techniques employ atomic force microscopy (AFM) or scanning tunneling microscopy (STM), respectively, to measure

biomolecular interactions [6,19]. These microscopy techniques are widely applicable with nanoscale spatial resolution but often suffer from poor temporal resolution. Solid-state transistor biosensors are also implemented in single-molecule studies in the form of nanowire devices, such as the single-walled carbon nanotube field-effect transistors (SWCNT-FETs) used in the latter half of this dissertation.

SWCNT-FETs boast single-molecule sensitivity due to their quasi-one-dimensional structure. SWCNTs can be idealized as a single sheet of graphene rolled into a cylinder. The single-layered structure of SWCNTs ensures that all charge carriers in the conductive channel are influenced by local changes at the SWCNT sidewall. Like gFETs, SWCNT-FETs are easily biofunctionalized for a wide range of biosensing applications [20-23]. SWCNT-FETs also allow for dynamic real-time measurements with microsecond time resolution and measurement durations lasting hours [20,21]. Additionally, SWCNT-FETs are largely insensitive to temperature, which enables studies at elevated temperatures that are inaccessible to other methods such as FRET due to fluorophore quenching. The Collins group has successfully used SWCNT-FETs to measure single-molecule dynamics and catalytic activity of various enzymes, including lysozyme, protein kinase A (PKA), DNA polymerase, and dihydrofolate reductase (DHFR) [24-26]. More recently, the Collins lab has shifted its focus to single-molecule measurements of Taq polymerase.

Taq polymerase is a thermostable DNA polymerase from the thermophilic bacteria Thermus aquaticus. Due to its thermostability, Taq is widely used in polymerase chain reaction (PCR), which puts it at the forefront of genomics. However, because Taq polymerase is most enzymatically active at around 75 °C, it has been primarily studied at the ensemble level and has been elusive to other single-molecule techniques. SWCNT-FETs are largely insensitive to temperature, making them an ideal candidate to study Taq at the single-molecule level. By

studying Taq with single-molecule resolution, we can try to demonstrate a new method of single-molecule science that is compatible with a wider range of temperature.

Like all experiments using solid-state transistor biosensors, the effects of applied potentials must be properly characterized and accounted for in these single-molecule Taq polymerase experiments. In addition to non-biological effects like electrostatic attraction or repulsion of charged substrates, the applied potentials may directly influence the enzyme itself. There is substantial work regarding the role of electrostatics in enzyme catalysis. For example, the electrostatic theory of enzyme catalysis suggests that preorganized active sites of enzymes promote reactions by reducing barriers via electrostatics such as protein charges, permanent dipoles, induced dipoles, and solvation by bound water molecules [27-35]. Furthermore, external electric fields have been shown to enhance catalytic rates, most often by field-induced stabilization of transition states [34,36-39]. Therefore, the liquid potential control may have significant effects on enzyme catalysis.

Beyond simply characterizing the effects of applied potentials, they may also be used as a tool, enabling a wider range of biosensing experiments. As mentioned previously, the liquid potential dictates the immediate electrostatic environment of the enzyme, which is often uncontrollable using other biosensing techniques. If the enzyme exhibits some dependence on its external electrostatic environment and therefore liquid potential, then control of that liquid potential may enable enzymatic control. If possible, a feature such as electrostatic enzymatic control using the SWCNT-FET platform would be a powerful tool for future applications. For example, one of the underlying goals of the work of the Collins lab is to utilize the SWCNT-FET platform biofunctionalized with DNA polymerase to sequence DNA. While there is preliminary evidence that each base-pair incorporation produces different signals, we currently cannot

discriminate between them with greater than 80 % accuracy [24]. However, electrostatic enzymatic control via liquid potential modulation could enable more accurate discrimination between base-pair incorporations. Additionally, an ideal DNA sequencing platform would benefit from dictating the rate of base-pair incorporations, which would also be within the scope of electrostatic enzymatic control.

The work in the second half of this dissertation tested the use of SWCNT-FETs to monitor the activity of individual Taq polymerase molecules. Moreover, the work presented here studied individual Taq polymerase molecules with various liquid potentials and investigated the effects of both constant and alternating potentials on the timing of catalytic motions.

Chapter 2

Controlling Applied Potentials to Explore and Reduce Signal Variation Using Cardea's Biosensor

Biosensing is a powerful field of study, constantly exploring new ways to probe and understand biology, with critical impacts in drug discovery, environmental monitoring, medical science, and more. Electronic biosensors are a new technology that enable electronic interrogation of biological interactions, rivaling current leading methods such as SPR and fluorescence. Many electronic biosensors boast a low detection limit with high specificity, which allow for experiments at the frontier of biosensing [1-3].

Cardea's gFET biosensor functions by monitoring the electrical conductance of the device in real time. gFET channel conductance can be affected by biomolecules through three distinct mechanisms. First, charged biomolecules that come into proximity with the graphene channel, by adsorption for example, can cause changes to local potentials at the graphene surface and electrostatically gate the device, altering channel conductance. The spatial sensitivity to changes in local potentials is primarily determined by the ionic strength of the liquid, which defines the Debye screening length. Second, immobilization of biomolecules on the graphene surface may modify the interfacial capacitance between the graphene channel and ionic liquid, which also contributes to channel conductance. Third, when biomolecules adsorbed or immobilized to the graphene surface are ionizable, there is an additional degree of freedom and pH sensitivity to electrostatic effects [40].

To calibrate the effectiveness of their gFET biosensors, Cardea developed an assay that reports binding measurements using an antibody-antigen pair from a commercially available

interleukin-6 (IL-6) ELISA kit [12]. Cardea chose the IL-6 antibody-antigen pair as a model system to test their biosensor because of its success and high sensitivity of < 5 pg/mL in ELISA measurements. In Cardea's IL-6 assay, monoclonal antibodies against human interleukin-6 (Anti-IL6) are immobilized onto the graphene surface, then recombinant human IL-6 (IL-6) antigens are introduced to bind with the immobilized antibodies. Using their gFET biosensor, Cardea reported reproducible results with a comparable sensitivity of 7.8 pg/mL [12].

Although Cardea has shown comparable performance to ELISA measurements, their gFET biosensors still have unaddressed issues. First, because there are multiple mechanisms by which biomolecules can affect gFET conductance, some biomolecules produce positive signals, others produce negative signals, and some appear to generate no signal at all. This variation makes it difficult to predict gFET biosensor signals when preparing new experiments. Furthermore, many biomolecules generate signals from nonspecific binding to the graphene surface, which must be measured and separated from signals resulting from specific binding of interest, such as antibody-antigen binding for example. There is also significant variation in gFET biosensor signals between measurements using different devices, otherwise referred to as signal variation. Signal variation may result from device fabrication variability, graphene synthesis variability, and even variation in biological reagents such as antibodies, antigens and linking reagents.

Signal variation is seen using 10 gFET biosensors from the same fabrication batch with the same reagents, indicating that device-to-device differences are important [12]. Further investigation using optical and atomic force microscopy show that the graphene composing each gFET have varying degrees of wrinkling, tearing and residual contamination from earlier fabrication steps, each of which contribute to varying surface potentials of the graphene. It is

possible that different gFETs will respond differently to changes in local potentials due to varying surface potentials of the graphene.

Variation in surface potentials may also affect biological interactions. Electrostatic effects on receptor-ligand binding, such as the antibody-antigen binding in Cardea's IL-6 assay, have been studied previously in a few different ways. Radic et al. explored electrostatic effects on the binding of cationic and neutral ligands to acetylcholinesterase (AChE) by varying ionic strengths and altering local potentials via AChE residue substitutions [41]. Dell'Orco et al. explored calbindin D_{9k} reconstitution with various fragment mutants, pH and salt concentrations [42]. Vainrub & Pettitt modeled DNA hybridization and melting at electrically charged surfaces [43]. Erbas et al. modeled the ionic effects on kinetics of both spontaneous and facilitated receptor-ligand dissociation [44].

Variation in surface potentials of the graphene can have significant effects on gFET responses and requires proper characterization. In this chapter, Cardea's IL-6 assay will be adapted with externally applied potentials to explore signal and, more specifically, device-to-device surface potential variation. Furthermore, applying external potentials may be able to correct for the surface potential variation, presenting a viable strategy to reduce or eliminate overall signal variation.

2.1 Graphene Biosensors by Cardea Bio

All measurements in this chapter were performed on commercially fabricated gFET biosensors from Cardea, depicted in **Figure 2.1**. Each packaged chip consists of three gFETs with separate Pt source electrodes and a common Pt drain electrode. Each gFET comprises five strips of monolayer graphene, measuring approximately 10 μm wide by 270 μm long, electrically

connected in parallel. All lithography is passivated with a silicon nitride (Si_3N_4) layer, with an additional epoxy window for on-chip liquid containment up to 100 µL. There are also Pt counter and reference electrodes on chip.

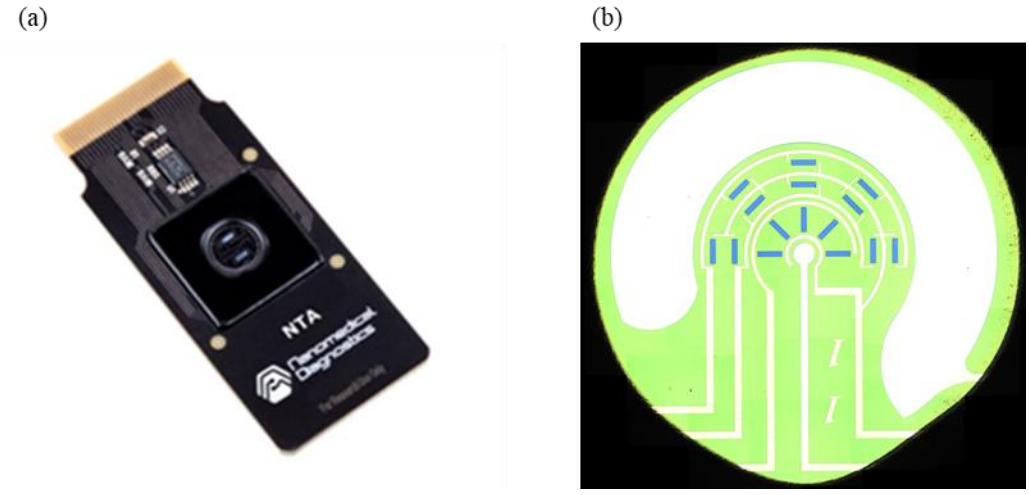

Figure 2.1: (a) Image of a fully fabricated, packaged chip from Cardea. (b) Top-down optical microscopy image of the chip surface. Chip lithography is shown in white. The large outer electrode is the counter electrode. The entire chip surface is passivated with silicon nitride (green), with windows (dark blue) to expose the graphene channels. Each of the three transistors consists of five concentric graphene channels, equidistant from the reference electrode at the center, electrically connected in parallel.

Measurements using Cardea's gFET biosensors were conducted in aqueous liquids with an ionic-liquid gate to allow real-time biosensing. When operating in the linear region away from the Dirac point, the current through an individual gFET is governed by

$$I_{sd} \approx \frac{W}{L}\mu C_g V_{sd}\left(V_0 - V_g + 2.3\phi_{th}\alpha\Delta pH + (1-\alpha)\Delta\varphi_D\right) \tag{2.1}$$

which relates source-drain current (I_{sd}) to width (W) and length (L) of the graphene channel, charge carrier mobility (μ), capacitance per unit area to the gate (C_g), source-drain voltage (V_{sd}), Dirac voltage (V_0), gate voltage (V_g), pH, and Donnan potential (φ_D) [12]. This equation is formulated from a combination of gFET and ion-sensitive field-effect transistor (ISFET) models [45,46].

The capacitance term, C_g, is a series combination of the graphene quantum capacitance [47], double layer capacitance [48], and capacitance due to the Donnan effect, which arises from a pseudo-membrane comprising immobilized polyethylene glycol (PEG) molecules. The surface pH sensitivity factor (α) is a material dependent value. For clean, isolated graphene, α is approximately 0.02 [40], but α has been measured to be about 0.37 for fully fabricated graphene transistors, due to alterations from the fabrication process [12,49]. This factor scales the thermal voltage (ϕ_{th}), about 26 mV, and the pH shift from a neutral surface (ΔpH) to produce the equivalent gate voltage due to pH. The Donnan potential is defined by

$$\Delta\varphi_D = \phi_{th} \ln\left(\frac{\sqrt{4c_s^2 + c_x^2} + c_x}{2c_s}\right) \tag{2.2}$$

where c_x is the ion concentration in the ion permeable layer and c_s is the ion concentration in bulk solution.

Biomolecular interactions at or near the graphene surface can affect multiple terms in **Eq. (***2.1*). Biomolecules on the graphene surface can affect the capacitance between the graphene channel and the ionic liquid. If the biomolecules on the graphene surface are charged, they will also electrostatically gate the graphene channel. Furthermore, charged biomolecules at the graphene surface influence the Donnan potential by altering the ion concentration in the pseudo-membrane of PEG molecules. If the biomolecules on the graphene surface are ionizable, they also introduce an additional degree of pH sensitivity, effectively changing α. To measure these effects, I_{sd} was acquired real-time throughout biosensing assays and changes in I_{sd} could be analyzed and attributed to biological or biochemical interactions. However, variation in graphene surface potentials also affect gFET conductance. While the Dirac voltage is primarily controlled by doping, variations in the graphene surface also create variations in the graphene surface potential,

and therefore the Dirac voltage. This variation in Dirac voltage also translates to varying effects due to pH, as ΔpH is calculated with respect to the charge neutrality point. Therefore, effects due to varying surface potentials need further investigation, isolation, and removal for proper interpretation of signals due to biological interactions.

2.1.1. IL-6 Assay by Cardea Bio

Before electrical measurement, each gFET is prepared by functionalizing the graphene surfaces with linker molecules. To do so, gFETs are submerged in a solution of pyrenylbutyric acid (PBA) dissolved in methanol. PBA molecules in solution noncovalently attach to the graphene surface via π-π stacking. Weakly bound, excess PBA molecules are subsequently rinsed away in ethanol, then isopropanol, then deionized water.

The standard protocol for performing an IL-6 assay with a Cardea gFET biosensor is outlined in **Table 2.1**. At each step, 50 µL of solution is dispensed with a manual pipette into the measurement well and left for a specific duration, depending on the step. At the end of each step, the liquid is aspirated off and 50 µL of solution for the next step is dispensed into the measurement well. After preparation with linker, the assay protocol begins at Step 1 with a 5-minute soak in 50 mM MES to allow for surface equilibriation. In Step 2, the functionalized carboxyl group is activated with EDC and stabilized with NHS. The antibody is introduced in Step 4 to chemically bind to the immobilized linker molecules through carbodiimide chemistry. In Steps 5 and 6, any residual, unbound carboxyl groups are quenched with amino-PEGs followed by ethanolamine. The remainder of the assay following the quench steps is performed in the same buffer to eliminate effects due to differences in pH and ionic strength. The next five steps involve rinsing with assay buffer to dissociate non-specifically bound molecules and allow for surface equilibriation after

protein immobilization. For the first three rinse steps, four 50 µL volumes of assay buffer are successively dispensed on and aspirated off the chip surface, then the fifth 50 µL volume of assay buffer is left on-chip for five minutes. The final two rinse steps forgo the four initial rinses, with a 5-minute soak using only a single 50 µL volume of assay buffer. Each 5-minute soak allows for equilibriation of longer timescale processes, if any exist. IL-6 antigen is introduced at Step 13 to bind with the immobilized anti-IL6 antibody. Subsequently, a single rinse using 50 µL of assay buffer is performed to presumably dissociate non-specifically bound IL-6 antigen, leaving only antigen that is bound to antibody.

In between buffer rinsing and antigen binding, a critical calibration measurement is performed at Step 12. In this step, the gFET is measured over five minutes while in assay buffer. The multiple rinse steps prior to the calibration are presumably sufficient for the device to equilibriate. If the device has reached equilibrium, I_{sd} should be constant in time throughout this calibration measurement. The end of this step, immediately prior to the introduction of antigen, is defined to be the zero-calibration point (ZCP). The 30 s average of $I_{sd}(t)$ leading up to the ZCP is defined to be the ZCP current. I_{sd} measurements from Steps 10 to 14 are analyzed as percent change from the ZCP current to reduce signal variation due to device-to-device variability.

Step	Time (min)	Description	Buffer	Analyte
1	5	Initial Calibration	50 mM MES	-
2	5	Linker Activation	50 mM MES	2 mM EDC + 5.5 mM NHS
3	1	Rinse 2x	50 mM MES	-
4	15	Antibody Association	Coating Buffer	1µg/mL Anti-Human IL-6
5	10	Amino-PEG Quench	PBS	1 mM Amino-PEG5-Alcohol
6	10	Ethanolamine Quench	PBS	1M Ethanolamine
7	5	Rinse 5x	Assay Buffer	-
8	5	Rinse 5x	Assay Buffer	-
9	5	Rinse 5x	Assay Buffer	-
10	5	Rinse 1x	Assay Buffer	-
11	5	Rinse 1x	Assay Buffer	-
12	5	Calibration	Assay Buffer	-
13	10	Antigen Association	Assay Buffer	5,000 pg/mL Recombinant Human IL-6
14	10	Antigen Dissociation	Assay Buffer	-

Table 2.1: Measurement protocol for the Cardea IL-6 assay.

The experimental architecture during antigen association (Step 13) is shown in **Figure 2.2**, adapted from [12]. The entire assay, as described in **Table 2.1**, is performed during electrical measurement using Cardea's Agile R100. I_{sd} is continuously acquired while V_{sd} is held constant and applied across the graphene channel. V_{lg} is swept continuously with a symmetric triangle wave from -100 mV to +100 mV using on-chip Pt counter and reference electrodes. I_{sd} is averaged over each 3-second period of the triangle wave to average out I_{sd} fluctuations. Measurements with continuous V_{lg} sweeping also allow real-time calculations of gate sensitivity, dI_{sd}/dV_{lg}. During

association, the antigens in solution specifically bind to antibody, as well as nonspecifically adhere to the graphene surface, both of which cause changes in the gFET conductance.

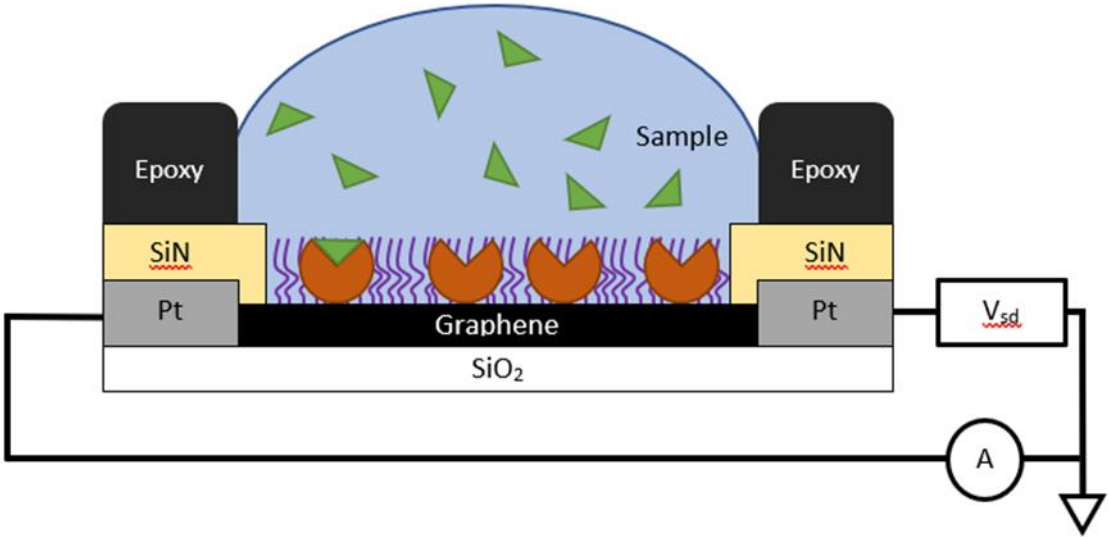

Figure 2.2: Diagram of the experiment. The graphene channel (black) is contacted by platinum source and drain electrodes (grey). The source and drain electrodes are passivated with silicon nitride (yellow) with an additional epoxy layer (black) for liquid containment. During target association, the antigen (green) in solution (blue) binds with an antibody (brown) immobilized to the graphene surface. The PEG molecules (purple) form a membrane that allows for the Donnan effect. V_{sd} is held constant while I_{sd} is continuously acquired.

Characteristic plots of I_{sd} over time are shown in **Figure 2.3**. **Fig. 2.3a** shows $I_{sd}(t)$ for an entire assay, outlined in **Table 2.1**, with key assay steps highlighted and time offset such that t = 0 s coincides with the ZCP. $I_{sd}(t)$ has a large response to the antibody, resulting from a combination of specific binding and nonspecific adsorption of antibodies on the graphene surface. $I_{sd}(t)$ also has a large response to the subsequent quench steps due to the different ionic strengths and pH values of each solution. Following the second quench step, the plot shows the long duration of repeated rinses, allowing $I_{sd}(t)$ to flatten and reach equilibrium for proper calibration immediately preceding t = 0 s, Step 12.

Fig. 2.3b shows a characteristic trace of $I_{sd}(t)$ specifically during Steps 10 through 14. The steps of interest are the final two steps involving antigen association and dissociation. $I_{sd}(t)$ decreases in the presence of antigen and increases back towards the ZCP current following the single buffer rinse at the beginning of Step 14, though it never fully restores to the ZCP current. The signals at the end of antigen association and dissociation are henceforth referred to as total surface adsorption (TSA) and residual binding (RB), respectively. TSA is measured at t = 600 s and RB is measured at t = 1200 s. To account for device variability, TSA and RB are calculated as percent change in I_{sd} from the ZCP current.

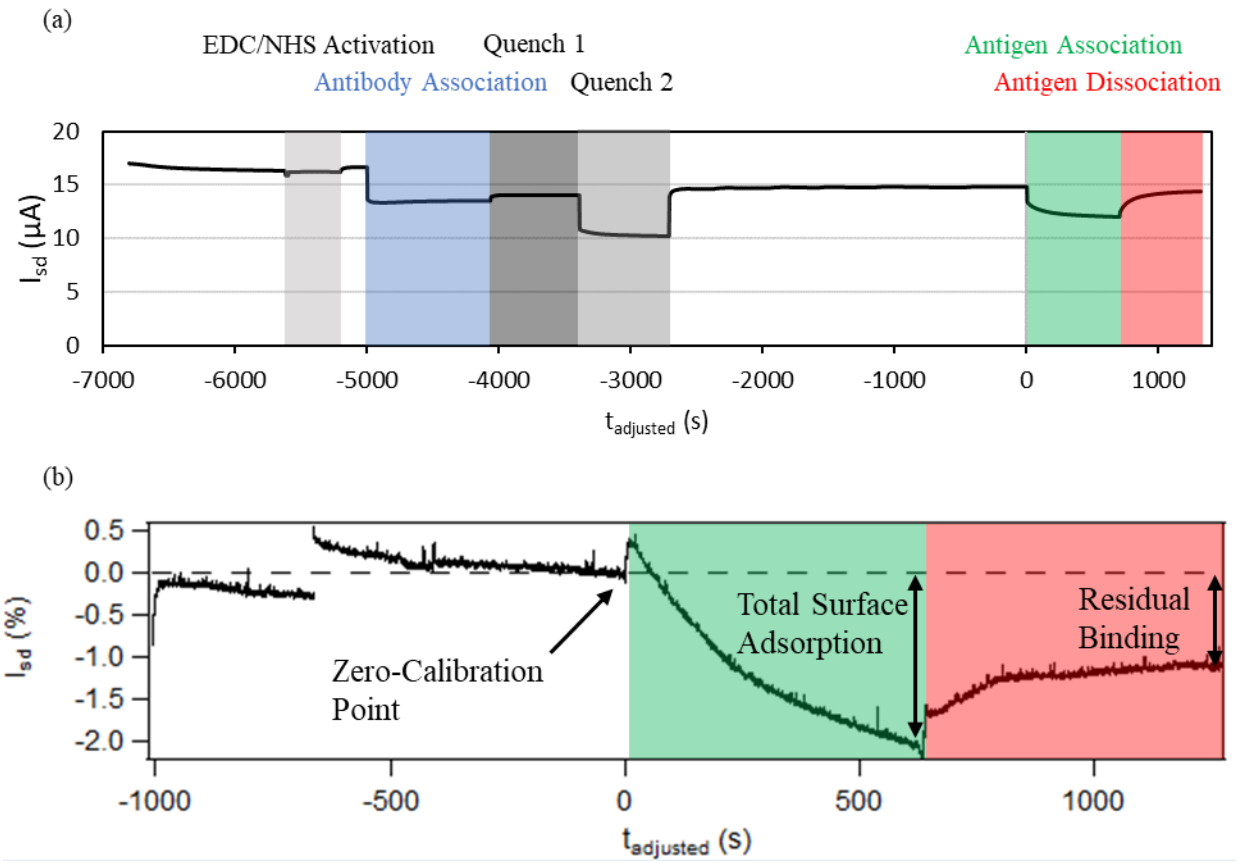

Figure 2.3: (a) Source-drain current, I_{sd}, throughout the assay with key steps highlighted. In chronological order: EDC/NHS activation (grey), antibody immobilization (blue), linker and surface quenching (grey), antigen association (green), then antigen dissociation (red). (b) I_{sd} during antigen association, dissociation, and the preceding rinse steps. TSA and RB are measured as % change at the end of the association and dissociation steps from the ZCP current, as depicted.

2.1.2 Interpretation of Key IL-6 Assay Signals

The two key measurements from Cardea's IL-6 assay are TSA and RB. These gFET responses occur when antigens interact with the graphene surface and surface immobilized antibodies. TSA is interpreted as the equilibrium surface loading that occurs in the presence of 5 ng/mL antigen concentration. TSA consists of two components: (i) the specific antibody-antigen binding and (ii) multiple nonspecific surface adhesion processes. TSA is measured approximately 600 seconds after antigen introduction, enough time for both association processes to equilibriate.

Antibody-antigen pairs typically have high binding affinities, so nearly all the antibody binding sites will be bound to antigen. However, nonspecific binding processes may be in a more dynamic, steady state equilibrium with significantly less than 100% surface loading. Antigens that nonspecifically adhere to the graphene surface are also assumed to be weakly bound to the surface.

RB is interpreted as the residual antigen that remains at the end of Step 14. Much of the nonspecifically adhered antigens should desorb during and following the buffer rinse because they are assumed to be weakly bound. Alternatively, only a small portion of specifically bound antigens should dissociate due to their high binding affinity to antibody. RB is measured approximately 600 seconds after the buffer rinse, enough time for both dissociation processes to equilibriate. Because the majority of residual antigen is presumably bound to antibody, RB is a more specific measure of the antibody-antigen binding than TSA.

2.2 Experimental Methods

This experiment investigated the effects of liquid potential V_{lg} control on Cardea's IL-6 antibody-antigen binding assay. To ensure fair comparison to Cardea's internal database of results, the experiment used Cardea's stock materials (**Fig. 2.1**), protocols (**Table 2.1**), and analysis methods (**Fig. 2.3**). Five sensor chips were selected from Cardea batch RG2H-06 and inspected optically and electrically to confirm that they were typical samples.

To achieve manual control over the applied potentials, Cardea's Agile R100 measurement system was replaced by a manual probe station. Packaged sensor chips were contacted using a breakout board and recorded with a current preamplifier (Keithley 428) and computer-controlled data acquisition board (NI PCIe-6361) [50]. V_{sd} was held constant at 100 mV.

Control of V_{lg} was introduced to the IL-6 assay using the external electronics depicted in **Figure 2.4**. The ends of two Pt wires (0.2 mm diameter, Alfa #00263) contacted the measurement

buffer and served as counter and pseudo-reference electrodes. These external wires were used instead of the on-chip Pt electrodes because they provided larger surface areas for better control of V_{lg} during liquid exchanges. The two Pt wires were connected to a Keithley 2400 SourceMeter in 4-wire mode, which provided continuous monitoring and control of V_{lg} and the counter electrode current I_{lg}. The stability and calibration of the Pt pseudoreference was checked against a standard Ag/AgCl reference electrode each day before measurements. During measurements, the on-chip Pt electrodes stayed electrically disconnected and floated to some equilibrium potential.

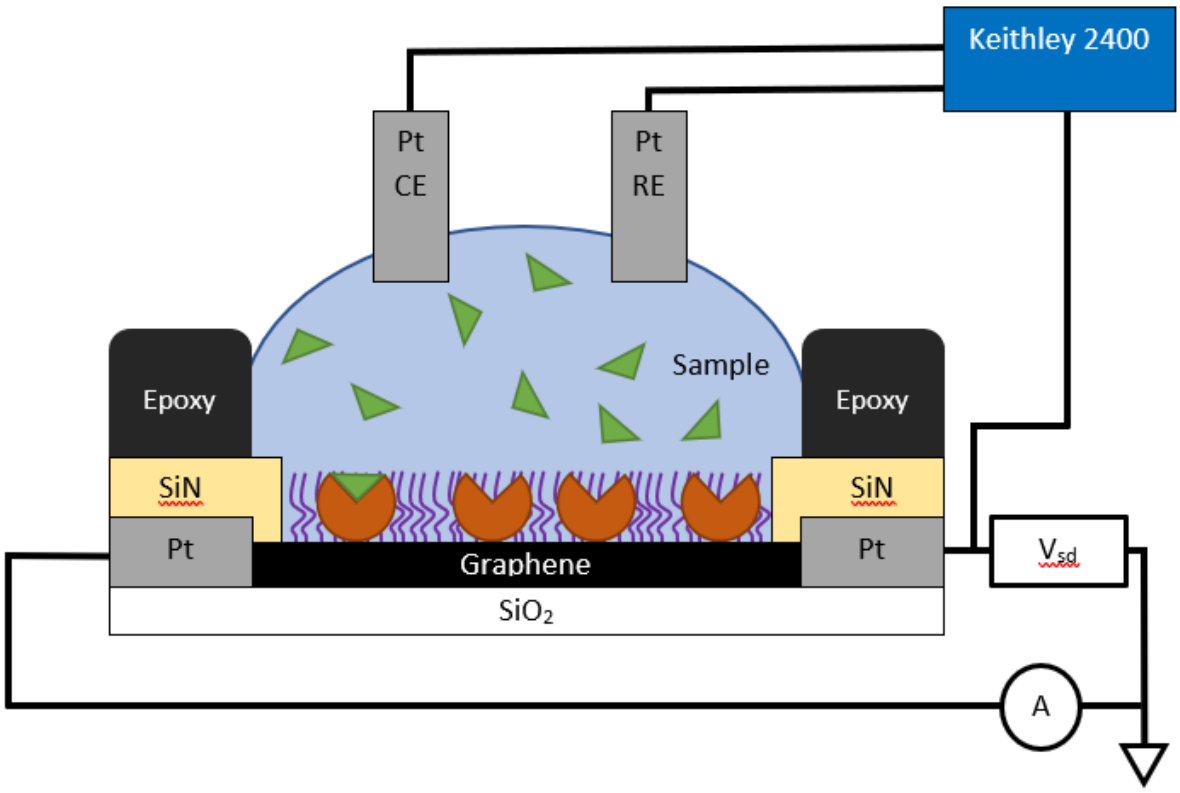

Figure 2.4. Diagram of the experiment with external control of V_{lg}. Pt wires as counter and reference electrodes were controlled by a Keithley 2400 in 4-wire mode. Its PID feedback controlled the counter electrode voltage to maintain the desired potential difference between the working electrode (graphene device) and the Pt pseudo-reference.

Measurements followed the Cardea protocol (**Table 2.1**) except with a DC bias applied continuously to V_{lg} instead of the normal triangle wave. Buffer rinsing and calibration, antigen

association and dissociation, and subsequent rising were all accomplished with a manual pipette and mechanical aspirator, using approximately 50 µL of solution for each step. At the end of this sequence, the device was continuously rinsed with an additional 2 mL of buffer solution to dissociate any remaining antigen. Then, as outlined in **Table 2.2**, V_{lg} was set to a new value and the process was repeated on the same device.

Step	Description
1 to 9	Device preparation
10	1x Rinse in Buffer
11	1x Rinse in Buffer
12	Calibration in buffer
13	IL-6 Antigen Association
14	IL-6 Antigen Dissociation
15	2 mL buffer rinse
16	Change V_{lg} and repeat Steps 10 to 15

Table 2.2. Modified protocol for the Cardea IL-6 assay at multiple V_{lg} values.

The protocol in **Table 2.2** was repeated on the same device at three or four V_{lg} values. The initial antibody functionalization and PEG passivation steps 1 thru 9 were not repeated on each cycle since these covalent linkages were assumed to be stable against buffer rinsing. Despite this stability, a single gFET was not measured at more than four V_{lg} values to protect against errors from gradual degradation or surface fouling. Furthermore, a single IL-6 assay required multiple liquid exchanges and rinses over the course of one hour; reproducibility of the manual pipetting could not be assured over more than four V_{lg} cycles. More typically, the measurement was concluded after three V_{lg} cycles because antigen lifetime in ambient was limited to 4 hours.

The experiment was completed on five independent devices listed in **Table 2.3**. For the entire measurement performed on device RG2H-06-194, $I_{sd}(t)$ remained within 1 % of the ZCP current. The lack of significant I_{sd} responses at key assay steps such as antigen association and dissociation at all V_{lg} was anomalous and specific to RG2H-06-194 and the device has been omitted from further discussion.

Date	Device	V_{lg} Values (V vs. Pt)
02/04/2020	RG2H-06-183	0.1, 0.3, -0.1
02/21/2020	RG2H-06-185	0.0, 0.2, 0.4
02/25/2020	RG2H-06-194	0, 0.1, 0.2, 0.3
03/04/2020	RG2H-06-196	0.1, 0.2, 0.3, 0.4
03/05/2020	RG2H-06-197	0.0, 0.2, 0.3

Table 2.3: Chronological order of measurements.

Since this research was exploratory, V_{lg} values were chosen somewhat at random and with consideration to the contemporaneous assay responses being produced by each gFET device. The starting V_{lg} value was chosen by measuring the resting potential of the Pt pseudoreference electrode with respect to the device, which typically equilibrated in the 0.0 to 0.1 V range. After the measurement on RG2H-06-183 confirmed strong V_{lg} effects, subsequent testing ramped V_{lg} more deliberately in monotonically increasing sequences and exclusively at positive potentials. Preliminary analysis indicated that steps of ΔV_{lg} = 0.2 V were larger than necessary to observe V_{lg} effects, so the final two devices RG2H-06-196 and -197 were measured with a smaller increment of ΔV_{lg} = 0.1 V.

Hysteresis and repeatability could not be investigated because measurements were limited to three or four V_{lg} values. For this initial study, probing a range of V_{lg} values was prioritized over test sequences like {0.0, +0.2, 0.0, +0.2 V} or {0.0, +0.1, +0.2, +0.1, 0.0 V} that might have revealed hysteresis and history-dependent instabilities in the assay response. For example, slow surface charging effects occur during long-duration V_{lg} stresses, and quasi-irreversible contamination of the gFET surface or the Pt electrodes readily shift the absolute V_{lg} calibration by up to ±0.15 V. Having no measurement of these effects, the following analysis makes a simplifying assumption that the assay response is single-valued in V_{lg}. Consequently, a significant uncertainty of at least ±0.05 V should be understood for all V_{lg} values reported here, far exceeding the ±0.005 V instrumental uncertainty. A combination of automated fluid delivery and longer test durations will enable future research to probe the reproducibility of assay response as V_{lg} sweeps in different directions with respect to the surface potentials.

2.3 Results of IL-6 assays with varying V_{lg}

Figure 2.5 shows measurements performed using Device RG2H-06-183. The initial $I_{sd}(t)$ recording collected at V_{lg} = 0.1 V was presented in **Fig. 2.3** as an example assay response, and it is reproduced in **Fig. 2.5a** for easy comparison to $I_{sd}(t)$ recordings collected at V_{lg} = 0.3 and -0.1 V (**Fig. 2.5b**). The three $I_{sd}(t)$ recordings are aligned to have their ZCPs at t = 0 s. Per the Cardea protocol, TSA and RB are measured at t = 600 and 1200 s, respectively.

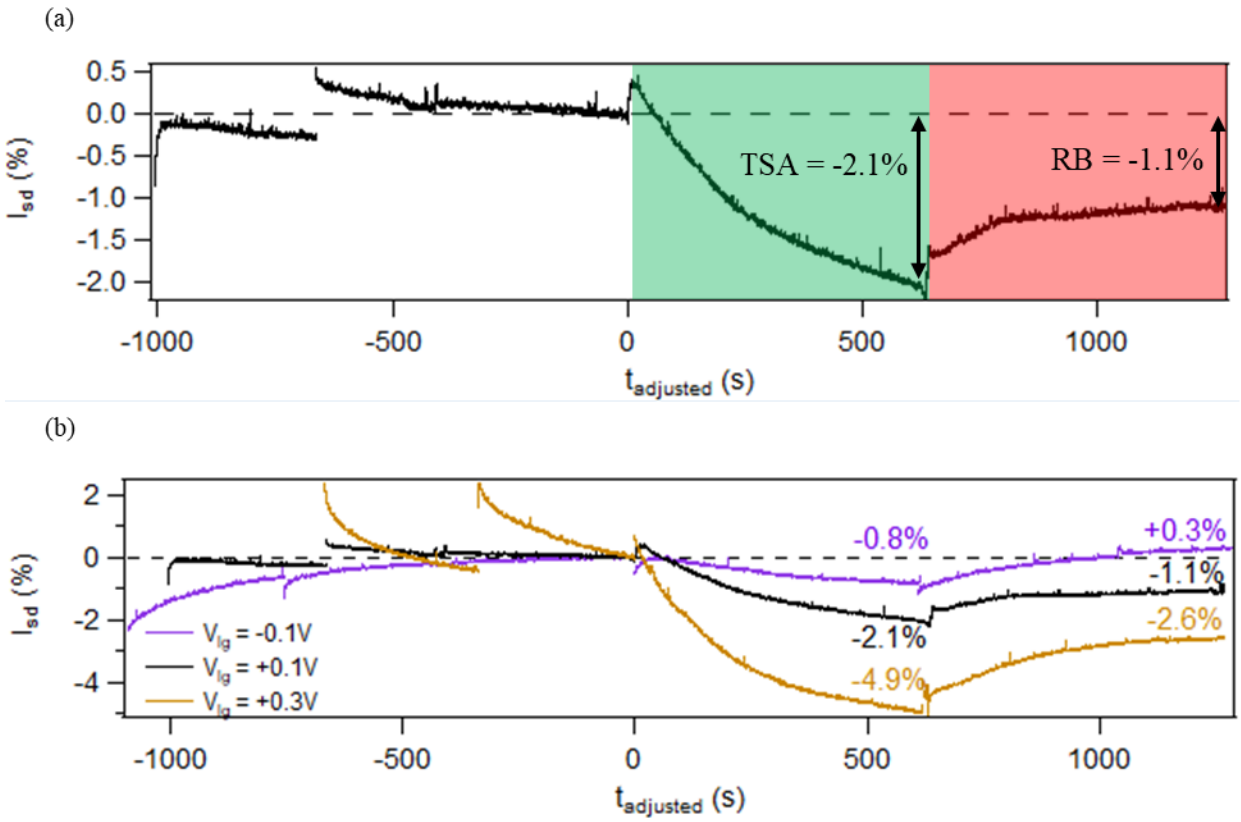

Figure 2.5. IL-6 assay recordings using Device RG2H-06-183, beginning from buffer rinse (Step 10) through antigen dissociation (Step 14). (a) $I_{sd}(t)$ at V_{lg} = 0.1 V. (b) Same data overlaid with subsequent assays at V_{lg} = 0.3 V (purple) and V_{lg} = -0.1 V (gold).

Fig. 2.5b shows that the main assay results, TSA and RB, depend strongly on the value of V_{lg}. The TSA value of -2.1 % obtained at V_{lg} = 0.1 V is comparable to other IL-6 assay results in the Cardea database, as expected for an applied V_{lg} potential that is close to the device's equilibrium resting potential. Raising V_{lg} by 0.2 V more than doubles the TSA response to 4.9 %, and lowering V_{lg} by 0.2 V dropped the TSA response to 0.8 %, and TSA appears to increase monotonically with V_{lg}. The RB response, though smaller, varied by similar proportions.

Quantitatively, the slope of this dependence, d(TSA)/dV_{lg}, was approximately -10 % per volt, a significant magnitude that merited further investigation. Extrapolating this dependence to the context of a typical measurement, ΔV_{lg} uncertainties of ±0.05 V cause variations ΔTSA = ±0.5

%, which is a large fraction of the TSA response normally reported for this assay. Stated differently, the assay result TSA = -2.1 ± 0.5 % has as much uncertainty than can be estimated just from the noise or slope of the $I_{sd}(t)$ recording.

Similar results were observed from three additional devices (**Figure 2.6**). Every test produced similar results: (1) a monotonic dependence on V_{lg}, (2) average sensitivities d(TSA)/dV_{lg} = -12 %/V and d(RB)/dV_{lg}. = -8 %/V, (3) negligible TSA and RB values at low V_{lg} (i.e. < 0.1 V), and (4) the largest TSA and RB observations at V_{lg} > 0.2 V. **Table 2.4** enumerates the raw $I_{sd}(t)$ values obtained at each protocol Step for all four devices, along with a summary of the final TSA and RB values calculated from the data after each test. The unnormalized $I_{sd}(t)$ values in **Table 2.4** illustrate the magnitude of device-to-device variations in DC conductance. ZCP currents ranged from 7 µA to 36 µA because of differences in Cardea's gFET devices. Normalization of the TSA and RB values appears to account for this variation.

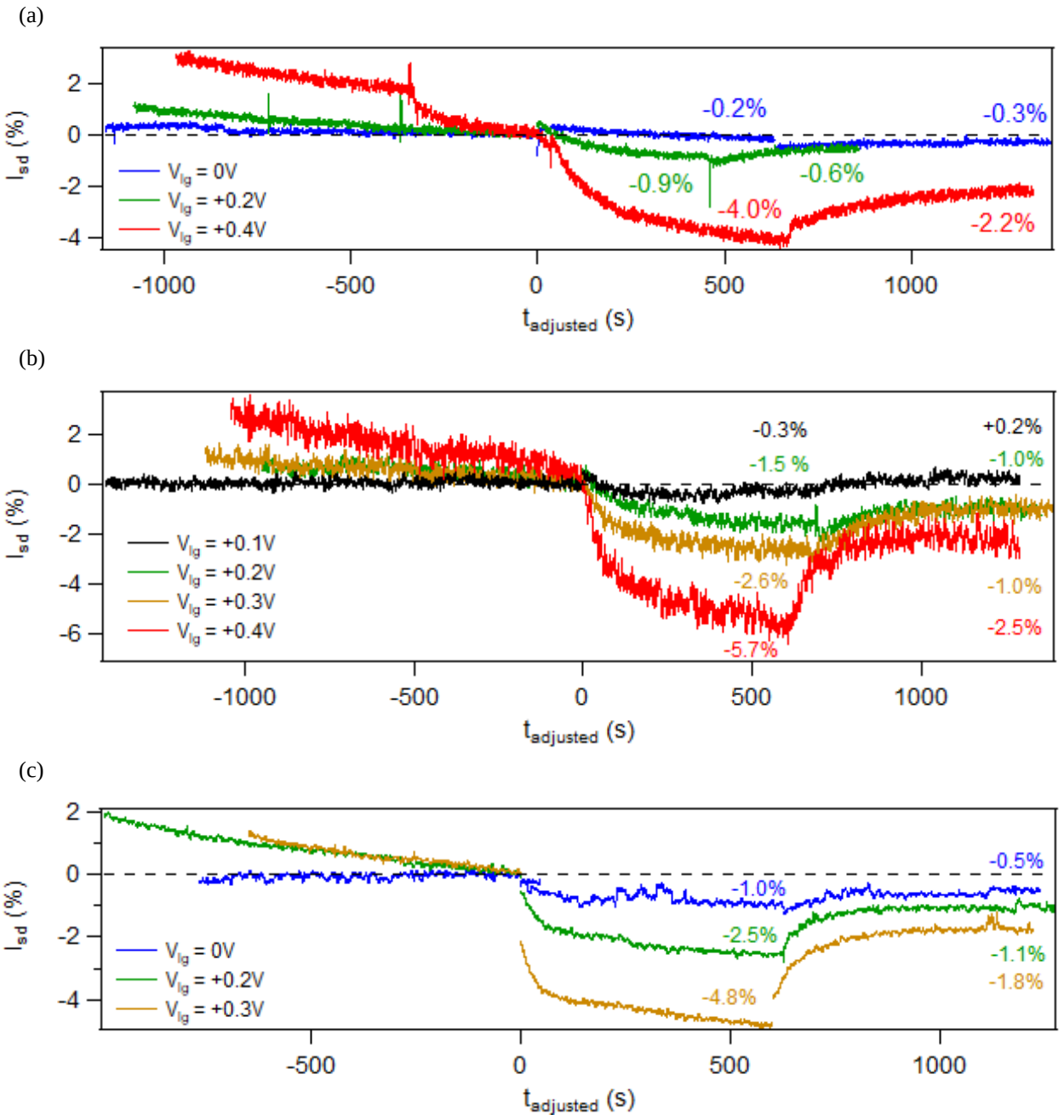

Figure 2.6. IL-6 assay recordings from (a) Device RG2H-06-185, (b) -196, and (c) -197. Curves are color coded according to the V_{lg} value, with 0 V (blue), +0.1 V (black), +0.2 V (green), +0.3 V (gold), and +0.4 V (red).

	V_{lg} (V)	ZCP Current (µA)	ΔI_{sd} (µA) at TSA	ΔI_{sd} (µA) at RB	TSA (%)	RB (%)
RG2H-06-183	-0.1	36.37	-0.29	0.11	-0.8 %	+0.3 %
	0.1	31.46	-0.67	-0.35	-2.1 %	-1.1 %
	0.3	23.51	-1.16	-0.61	-4.9 %	-2.6 %
RG2H-06-185	0.0	24.89	-0.04	-0.07	-0.2 %	-0.3 %
	0.2	20.15	-0.18	-0.12	-0.9 %	-0.6 %
	0.4	12.89	-0.52	-0.29	-4.0 %	-2.2 %
RG2H-06-196	0.1	18.52	-0.06	0.04	-0.3 %	+0.2 %
	0.2	16.37	-0.25	-0.17	-1.5 %	-1.0 %
	0.3	13.04	-0.34	-0.13	-2.6 %	-1.0 %
	0.4	9.15	-0.52	-0.23	-5.7 %	-2.5 %
RG2H-06-197	0.0	11.74	-0.12	-0.06	-1.0 %	-0.5 %
	0.2	9.04	-0.23	-0.10	-2.5 %	-1.1 %
	0.3	7.13	-0.34	-0.13	-4.8 %	-1.8 %

Table 2.4. I_{sd} values at ZCP, TSA, and RB steps, and the calculated, normalized assay results.

Two other aspects of the raw data were noteworthy. First, 2 out of 13 $I_{sd}(t)$ recordings finished at slightly positive values of +0.2 and +0.3 %. As noted above, signals of this magnitude were smaller than the experimental errors and indistinguishable from zero. Drift of the Pt pseudo-reference by $\Delta V_{lg} < 0.04$ V could account for the entire RB signal measured in these traces, and drift of this magnitude is reasonable given that 20 minutes elapse between the ZCP and RB measurements.

Secondly, the measurements highlight the failure of devices to achieve equilibrium in the Cardea protocol. While dI_{sd}/dt approached zero in some instances, $I_{sd}(t)$ was changing continuously when most values of ZCP current, TSA, and RB were recorded. This lack of equilibriation complicates physical interpretation of the TSA and RB signals and raises questions about the validity of comparing these signals from different V_{lg} conditions. Furthermore, varying degrees of electrochemical charging were observed in $I_{sd}(t)$ during the buffer exchanges preceding the

measurement of ZCP current, and this charging might offset the measurement of ZCP current or affect antibody-antigen binding. By varying V_{lg} to new values, this experiment revealed all of these effects as possible causes of variation and irreproducibility in electronic biosensing.

2.4 Analysis and discussion of V_{lg} dependence and its effects on the IL-6 assay

Some of the issues raised above can be investigated using the existing data in **Fig. 2.6** and **Table 2.3**. First, the following discussion provides a more quantitative summary of the V_{lg} trends observed in the IL-6 assay. Second, an analysis method is proposed to account for some of the electrochemical effects of V_{lg} that confound interpretation of the antibody-antigen binding results. Following the discussion of these effects, the section concludes with a re-analysis of the IL-6 data that obtains more reliable TSA and RB values.

2.4.1 Summary of TSA and RB results

Figure 2.7 provides different graphical representations of the TSA and RB results in **Table 2.4**. Scatterplots of TSA (**Fig. 2.7a**) and RB (**Fig. 2.7b**) versus V_{lg} show the range of results and the device-to-device variation. The V_{lg} trend for each device is emphasized with added coloring and a solid line connecting the device's data points.

The solid lines also reveal similarities in the V_{lg} dependence among the devices. Shifting these curves along the *x*-axis appears to align them, emphasizing the underlying trend. Artificial shifts of +0.15 V, -0.05 V, and -0.02 V for data from Devices RG2H-06-183, -185, and -197, respectively, appear to produce the best agreement. Shifted curves for TSA (**Fig. 2.7c**) and RB (**Fig. 2.7d**) indicate that the assay results are more similar than different.

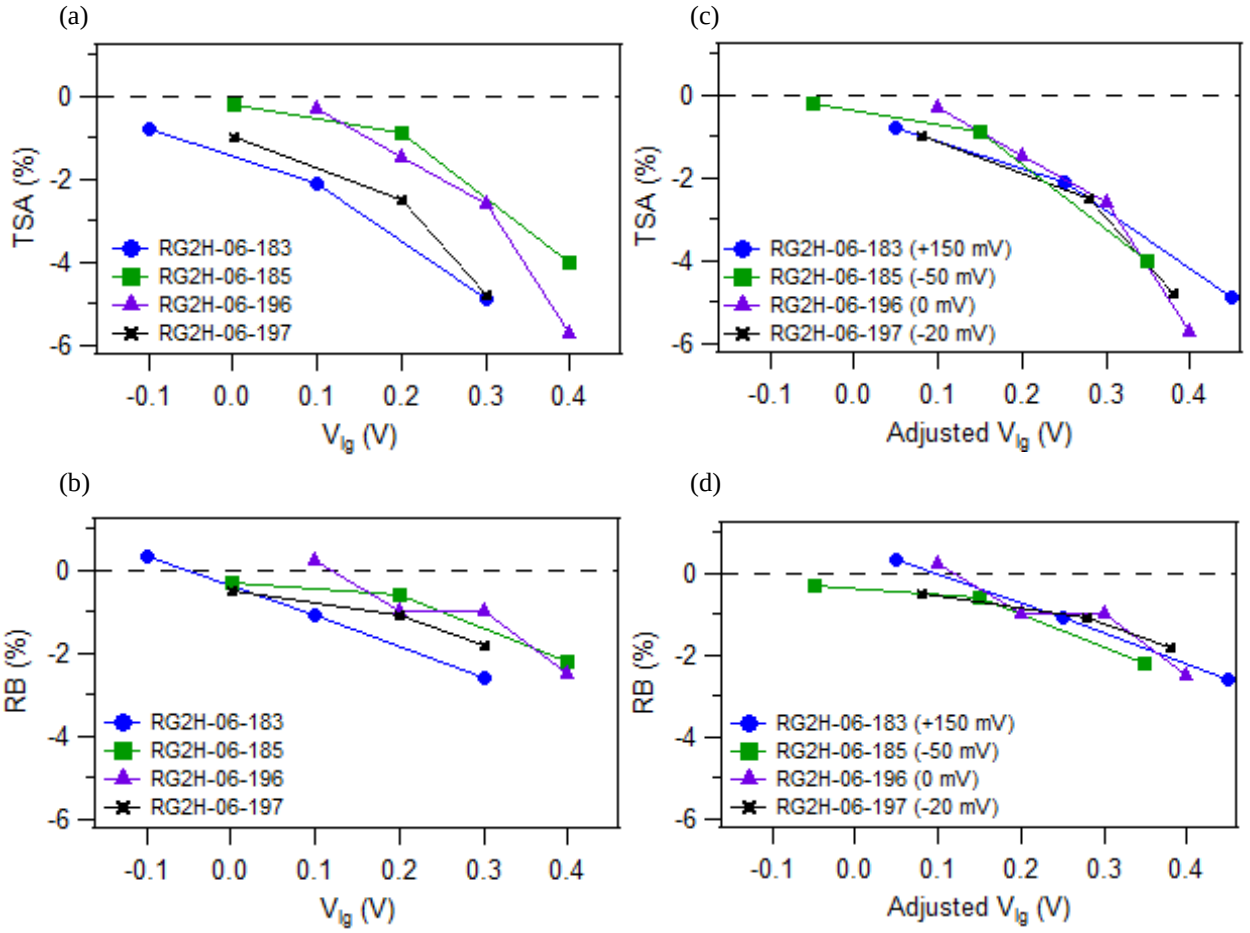

Figure 2.7. (a) TSA and (b) RB, expressed as % change in I_{sd}, at all V_{lg}. (c) TSA and (d) RB, shifted in V_{lg} to artificially account for gating variation between devices. Device names and amount of V_{lg} shift are annotated.

Two effects might account for the apparent shifting of response curves along the V_{lg} axis. Shifts (ΔV_{lg}) as large as ±0.1 V lay within the range caused by contamination of the Pt pseudo-reference electrode, and this type of shift would reasonably be different from one device to another. Moreover, the gFET fabrication produces devices with surface potentials varying by up to ±0.3 eV. This variation is most well known in the graphene literature as a shift in the *Dirac point* of graphene's bandstructure, a doping level at which graphene has a cusp of minimum conductance. Each gFET has a slightly different Dirac point voltage, so under identical V_{lg} conditions each

device will have different local surface potentials, carrier concentrations, and sensitivities. Shifting the curves in **Fig. 2.7** is an artificial method to correct for this variability. Given the magnitude of the underlying mechanisms, the shifts needed to find alignment in **Fig. 2.7** seem well justified.

After alignment, the TSA and RB curves appear to retain different functional dependence on V_{lg}. All of the TSA plots exhibit curvature, with TSA dropping to an asymptotic limit of 0 % for $V_{lg} < 0$ V. The average RB dependence, on the other hand, appears to be linear in V_{lg}.

2.4.2 Background electrochemical currents

Applying an external potential V_{lg} can induce new contributions to $I_{sd}(t)$ that affect normalization and interpretation of the IL-6 assay. For example, large V_{lg} values will produce Faradaic currents from exposed Pt electrodes and graphene defects and edges. Below the threshold for Faradaic processes, changes in V_{lg} induce currents $C\mathrm{d}V_{lg}/\mathrm{d}t$, where C is capacitance of the sensing surface, the electrochemical double layer, or any other element susceptible to charging. $C\mathrm{d}V_{lg}/\mathrm{d}t$ transients were observed at every liquid exchange in $I_{sd}(t)$ recordings like those shown in **Fig. 2.5**.

To guard against these transients, the IL-6 assay protocol (**Table 2.1**) was designed with a 300 s equilibriation period before measurement of ZCP current, and 600 s equilibriation periods before measurements of TSA and RB. These long durations were chosen for antibody-antigen binding and dissociation processes to reach steady state, but it should also be sufficient for most electrochemical charging processes to complete. After all, Cardea's biosensing element is an unpassivated, single-atom-thickness graphene sheet with rapid charging kinetics.

Nevertheless, **Fig. 2.6** shows numerous cases in which $dI_{sd}(t)/dt$ does not flatten to zero at the designated measurement time. While visibly obvious at the highest V_{lg} values, the slope $dI_{sd}(t)/dt$ was nonzero at the ZCP in every $I_{sd}(t)$ recording. Inspection also suggests that $dI_{sd}(t)/dt$ was often the same at ZCP, TSA, and RB measurement points, indicating that it was independent of antibody-antigen dynamics.

Electrochemically induced currents with constant slope $dI_{sd}(t)/dt$ are indicative of charging processes with characteristic times much longer than the measurement period. In **Fig. 2.6**, this characteristic time exceeded 1 hour. Similar effects are well established for conventional ion-sensitive FET (ISFET) sensors, in which an insulating dielectric is very slow to equilibriate with the surrounding chemical potential [45,46]. In ISFETs, the slowest processes arise from reactive sites and charge traps in either the gate dielectric or the bulk SiO_2 substrate supporting the FET [51,52]. Proper interpretation of ISFET data must properly account for these slow processes, in addition to faster charging transients and Faradaic leakage currents.

A similar accounting for the IL-6 assay was accomplished by defining a background surface equilibriation (BSE) current. BSE was defined empirically, without any reference to the underlying mechanisms, by measuring the residual $dI_{sd}(t)/dt$ in buffer at the ZCP. In practice, combining the ZCP current (magnitude) with BSE (slope) converted the current normalization factor from a scalar to a two-component function of time. For convenience, BSE is evaluated with units of current % change per 600 s. In these units, BSE explicitly predicts the contribution of electrochemically induced currents expected at t = 600 s, the moment of TSA measurement. Doubling BSE extrapolates its value by another 600 s to the RB measurement at t = 1200 s.

The BSE current defined above was calculated for every $I_{sd}(t)$ recording. BSE values are tabulated in **Table 2.5** alongside the TSA value from each recording. BSE produced signals as

large as -2% at t = 600 s. On average, the BSE contribution was one-quarter to one-third of the corresponding TSA value, indicating that the uncorrected TSA values overstate the effects of antigen binding and adsorption. At t = 1200 s, the doubled value of BSE was comparable to, and sometimes larger than, the reported RB values. Therefore, the RB values were deemed to be incorrect without more careful consideration of the BSE contributions.

Device Name	V_{lg}	BSE (% / 600 s)	TSA (%)	2x BSE (% / 1200 s)	RB (%)
RG2H-06-183	-0.1 V	1.2 %	-0.8 %	2.4 %	+0.3 %
	0.1 V	-0.5 %	-2.1 %	-1.0 %	-1.1 %
	0.3 V	-2.1 %	-4.9 %	-4.2 %	-2.6 %
RG2H-06-185	0.0 V	-0.3 %	-0.2 %	-0.6 %	-0.3 %
	0.2 V	-0.5 %	-0.9 %	-1.0 %	-0.6 %
	0.4 V	-1.6 %	-4.0 %	-3.2 %	-2.2 %
RG2H-06-196	0.1 V	-0.1 %	-0.3 %	-0.2 %	+0.2 %
	0.2 V	-0.6 %	-1.5 %	-1.2 %	-1.0 %
	0.3 V	-0.6 %	-2.6 %	-1.2 %	-1.0 %
	0.4 V	-1.9 %	-5.7 %	-3.8 %	-2.5 %
RG2H-06-197	0.0 V	0.2 %	-1.0 %	0.4 %	-0.5 %
	0.2 V	-1.1 %	-2.5 %	-2.2 %	-1.1 %
	0.3 V	-1.3 %	-4.8 %	-2.6 %	-1.8 %

Table 2.5. Comparison of BSE and 2x BSE to TSA and RB values.

Figure 2.8 graphically demonstrate BSE adjustments using the $I_{sd}(t)$ recording from Device RG2H-06-196 at V_{lg} = 0.3 V. First, the BSE value was determined from a linear fit to $I_{sd}(t)$ from t = -600 s up to the ZCP at t = 0 s (**Fig. 2.8a**). The fit of -0.6 % per 600 s was then extrapolated (**Fig. 2.8c**) and subtracted from the entire $I_{sd}(t)$ trace. Inspection of the residual data showed the success of this subtraction in flattening $I_{sd}(t)$ for a more precise evaluation of ZCP (**Fig. 2.8b**) and for revised evaluation of TSA and RB (**Fig. 2.8d**). In this example, accounting for the BSE current shrank the TSA signal from -2.6 % to -2.0 %. The flat, residual $I_{sd}(t)$ provided a much greater

confidence that the revised TSA value was obtained in equilibrium and interpreted correctly. The RB value, which was originally assigned to be -1.0 %, was more accurately evaluated to be 0.2 % ± 0.3 %, statistically indistinguishable from zero.

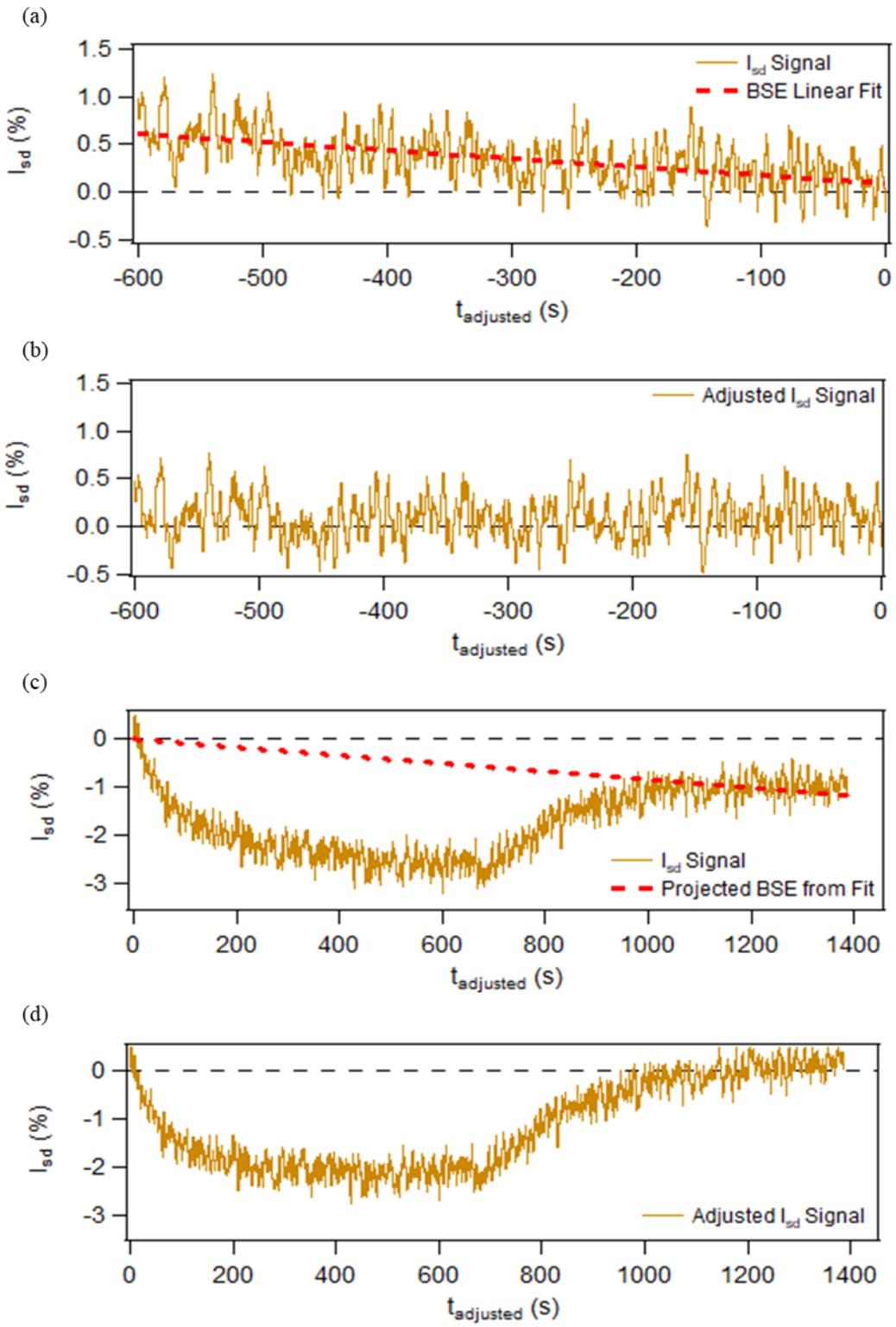

Figure 2.8. Device RG2H-06-196 at V_{lg} = 0.3 V with fitting to correct for BSE currents. (a) Raw $I_{sd}(t)$ leading up to the ZCP at t = 0 s, overlaid with a linear fit representing BSE. (b) Residual $I_{sd}(t)$ after subtracting the BSE. (c) $I_{sd}(t)$ during antigen association and dissociation, overlaid with an extrapolation of the BSE current. (d) Residual $I_{sd}(t)$ during antigen association and dissociation.

One notable error introduced by the BSE correction will occur if the antigen's specific and nonspecific binding times are comparable. The TSA and RB measurements assume that specific antigen-antibody binding and dissociation reach steady state equilibrium. Dissociation of nonspecific fouling, on the other hand, can have different populations with short, long, and semi-infinite time scales. While long-duration fouling is not a significant problem for a differential comparison of TSA and RB, it is a dynamic that certainly affects accurate ZCP current and BSE evaluation when a device is being reused. Ongoing surface dissociation of antigen from a previous test will cause subsequent effects in $I_{sd}(t)$ that compromise ZCP current and BSE measurements. For repeated assays probing V_{lg} dependence, reliable use of the BSE correction may require special attention to dissociation dynamics between trials.

Finally, it is useful to consider the source of the long time constants in Cardea's devices. In ISFETs, the sensing channel is separated from the measurement solution by a dielectric, the entire surface of which is exposed to charge injection, migration, and slow trapping dynamics. Cardea's gFET channel is not similarly passivated, but it does sit upon an SiO_2 support that will support trapping mechanisms. Furthermore, the graphene is noncovalently bound to the SiO_2 by van der Waals forces, and this binding is an incomplete barrier to interlayer ion migration. The unprotected edges of Cardea's gFET may provide a pathway for ions to insert themselves and then slowly equilibriate across the 10 μm channel width. Passivation of the gFET edges might be a successful strategy for eliminating this migration pathway.

2.4.3 Functional dependence of background surface equilibriation (BSE) on V_{lg}

Figure 2.9 plots the BSE values listed in **Table 2.6** versus the liquid potential V_{lg}. In general, BSE was approximately linear in V_{lg} and closest to zero in the range of 0.0 to 0.1 V.

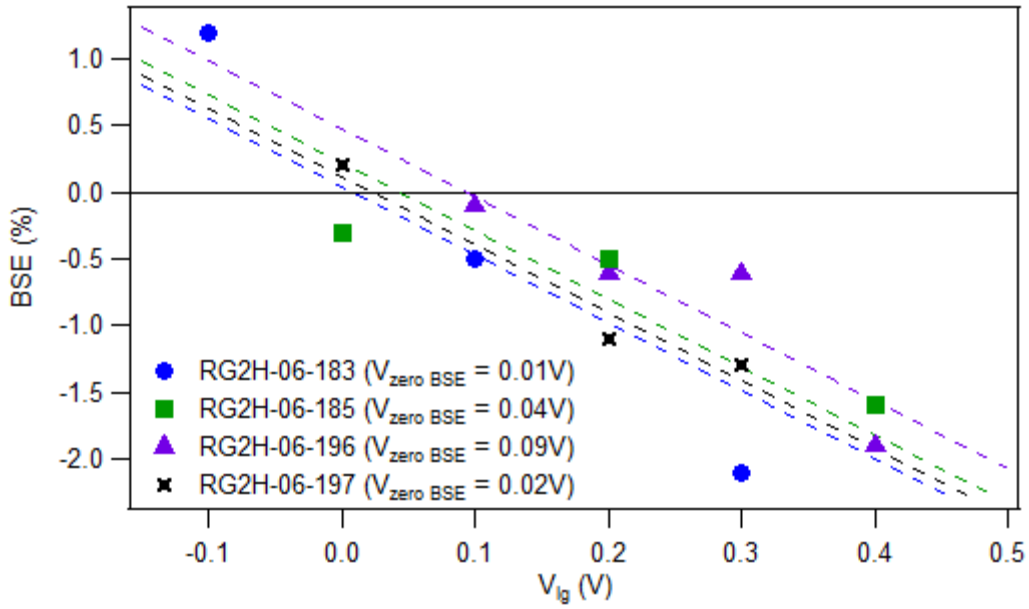

Figure 2.9. BSE versus V_{lg} for all devices. Dashed lines depict linear fits for each device with a slope constrained to the average value of -5.5 %/V per 600 s.

Two methods were used to evaluate the linear slope of BSE versus V_{lg}. In the first case, a least-squares linear fit was calculated for the data from each device. This fitting resulted in slopes d(BSE)/dV_{lg} of -3 to -8 % per volt per 600 s (**Table 2.6**). In this method, each fitting was done with only 3 or 4 data points per device, and the variance and uncertainty in slope were further increased by apparent outliers. Consequently, a second method was developed in which an average was calculated for the entire data set from the slopes of every pair of adjacent data points. This second method calculated an average slope d(BSE)/dV_{lg} = -5.5 % per volt per 600 s. Inspection of **Fig. 2.9** suggests that this slope fairly represented the entire data set and its functional dependence on V_{lg}. Finally, a device-dependent intercept was calculated by constraining the fitting of each device to this average slope. Those fits are depicted as dashed lines in **Fig. 2.9**, and the corresponding intercepts are listed in **Table 2.6**.

Device	Unconstrained linear fits		Constrained linear fits	
	Slope d(BSE)/dV_{lg} (% per V per 600 s)	Intercept (V)	Slope d(BSE)/dV_{lg} (% per V per 600 s)	Intercept (V)
RG2H-06-183	-8.2	0.04	-5.5	0.01
RG2H-06-185	-3.2	-0.05	-5.5	0.04
RG2H-06-196	-5.4	0.10	-5.5	0.09
RG2H-06-197	-5.2	0.03	-5.5	0.02

Table 2.6. Device-dependent linear fits of BSE versus V_{lg} with and without constraints.

For either method, the V_{lg} intercept at which BSE was reduced to zero varied by less than 0.15 V from one device to another. This small range suggests systematic error, such as shifts that arise from device-to-device variability, surface contamination, or V_{lg} uncertainties caused by shifts of the Pt pseudo-reference potential.

Similar mechanisms were suggested in §2.4.1 Summary of TSA and RB results to describe *ad hoc* shifting to align the TSA vs. V_{lg} curves (**Fig. 2.7c**). However, the V_{lg} intercepts in **Table 2.5** do not follow the same pattern as those *ad hoc* shifts, which also extended over a larger range of 0.2 V. The lack of any obvious correspondence between the two types of adjustment is noteworthy because both effects presumably result from the same lack of control over chemical potential. The fact that two different methods suggest different amounts and directions of shift might simply reflect the quality of the limited data set. Alternately, the difference might indicate the presence of two distinct mechanisms. Specifically, the dominant BSE mechanism is likely the slow charging of SiO_2 traps under the gFET, whereas the (normalized) TSA and RB are results are most influenced by antigen dynamics in solution over the gFET. In any case, both methods reflected small shifts in chemical potential that were in agreement with the stated uncertainty of V_{lg}.

2.4.4 Re-analysis of the IL-6 assay with corrected TSA and RB values

The BSE adjustments described in §2.4.2 Background electrochemical currents were performed for every IL-6 assay result. Corrected TSA and RB values are tabulated in **Table 2.7** and **Table 2.8**, respectively. Since the BSE adjustment resulted in relatively flat $I_{sd}(t)$ recordings at the time of measurement, quantitative error bars for TSA and RB could also be calculated from the peak-to-peak fluctuations in $I_{sd}(t)$. An additional error was observed in which some $I_{sd}(t)$ traces were not successfully flattened by the BSE adjustment procedure, perhaps because of a discontinuous change in current during the experiment. **Table 2.7** and **Table 2.8** include additional measurements of the "residual slope", dI_{sd}/dt, remaining after BSE adjustment to denote added uncertainty in some values.

In general, correction for BSE currents reduced the apparent TSA values (**Table 2.7**). The smallest corrections occurred for V_{lg} = 0.0 or 0.1 V, where BSE currents were negligible. For V_{lg} > 0.1 V, TSA values were -2 to -4 %. Despite being reduced in magnitude, the values were ten times larger than the remaining errors and (much reduced) measurement uncertainties, and they represented significant positive detections by the IL-6 sensor. The results are depicted graphically in **Fig. 2.10**, with the curves shifted by small amounts (noted in the legend) to match **Fig. 2.7c**. As in **Fig. 2.7c**, **Fig. 2.10** shows good agreement among overlapping curves and a response that approached zero asymptotically at $V_{lg} < 0$.

Device	V_{lg}	Raw TSA	Corrected TSA	Error	Residual Slope (% per 600 s)
RG2H-06-183	-0.1 V	-0.8 %	-1.2 %	± 0.1 %	-0.3 %
	0.1 V	-2.1 %	-1.9 %	± 0.1 %	-0.5 %
	0.3 V	-4.9 %	-3.3 %	± 0.1%	0.0 %
RG2H-06-185	0 V	-0.2 %	-0.1 %	± 0.1 %	-0.2 %
	0.2 V	-0.9 %	-0.5 %	± 0.1 %	0.0 %
	0.4 V	-4.0 %	-2.9 %	± 0.2 %	0.0 %
RG2H-06-196	0.1 V	-0.3 %	-0.4 %	± 0.3 %	0.0 %
	0.2 V	-1.5 %	-1.2 %	± 0.4 %	0.0 %
	0.3 V	-2.6 %	-2.0 %	± 0.4 %	0.0 %
	0.4 V	-5.7 %	-4.5 %	± 0.7 %	0.0 %
RG2H-06-197	0 V	-1.0 %	-1.0 %	± 0.1 %	0.0 %
	0.2 V	-2.5 %	-1.6 %	± 0.1 %	+0.2 %
	0.3 V	-4.8 %	-3.9 %	± 0.1 %	0.0 %

Table 2.7. Raw and corrected TSA values, with calculated errors.

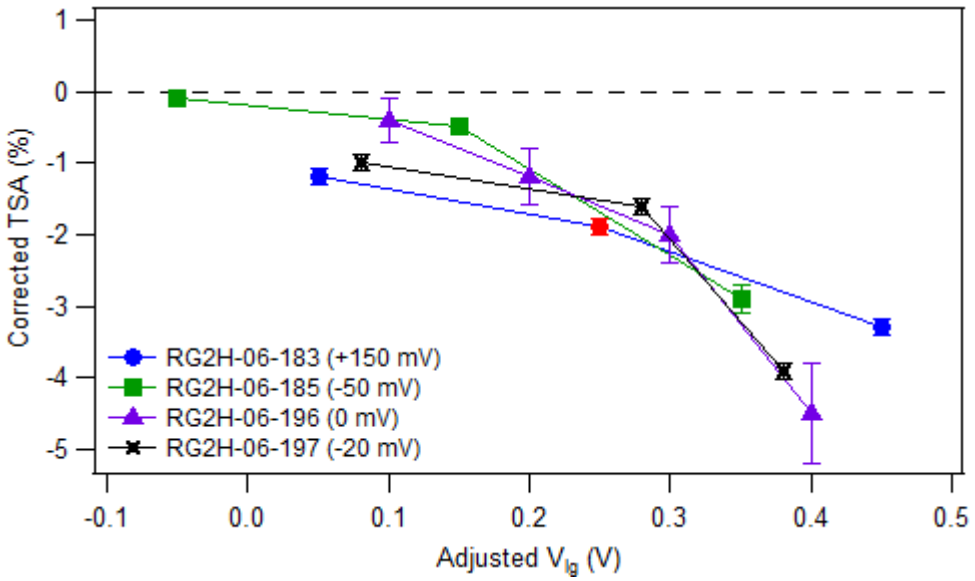

Figure 2.10. Corrected TSA versus adjusted V_{lg}, with the amount of each V_{lg} shift noted in the legend. Red point denotes one measurement having a residual slope error dI_{sd}/dt = -0.5 % per 600 s.

Device	V_{lg}	Raw RB	Corrected RB	Error	Residual Slope (% per 600 s)
RG2H-06-183	-0.1 V	0.3 %	-0.5 %	± 0.1 %	0.0 %
	0.1 V	-1.1 %	-0.7 %	± 0.1 %	+0.1 %
	0.3 V	-2.6 %	0.7 %	± 0.1 %	+1.0 %
RG2H-06-185	0 V	-0.3 %	-0.2 %	± 0.1 %	0.0 %
	0.2 V	-0.6 %	0.1 %	± 0.1 %	+0.5 %
	0.4 V	-2.2 %	0.3 %	± 0.2 %	+0.7 %
RG2H-06-196	0.1 V	0.2 %	0.2 %	± 0.2 %	0.0 %
	0.2 V	-1.0 %	-0.1 %	± 0.3 %	0.0 %
	0.3 V	-1.0 %	0.2 %	± 0.3 %	0.0 %
	0.4 V	-2.5 %	0.0 %	± 0.7 %	0.0 %
RG2H-06-197	0 V	-0.5 %	-0.5 %	± 0.1 %	0.0 %
	0.2 V	-1.1 %	0.7 %	± 0.1 %	+0.5 %
	0.3 V	-1.8 %	-0.5 %	± 0.2 %	+0.8 %

Table 2.8. Raw and corrected RB values, with calculated errors.

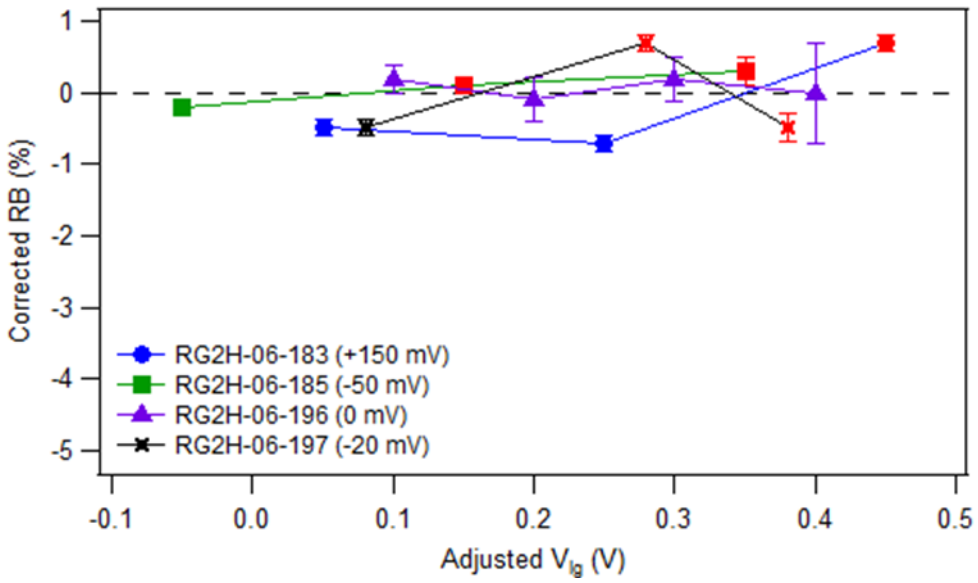

Figure 2.11. Corrected RB versus adjusted V_{lg}, with the amount of each V_{lg} shift noted in the legend. Red points denote measurements with residual dI_{sd}/dt > 0.5% per 600 s.

Figure 2.11 shows a similar plot of the corrected RB values (**Table 2.8**). The corrected RB signal was less than 1 % for all devices at all V_{lg} values, with no appreciable difference from zero. These results signify *no residual binding* of IL-6 antigens on Cardea's sensor. Nearly half of the RB values in **Fig. 2.11** are colored red to denote residual slopes dI_{sd}/dt ranging from 0.5 to 1.0 % per 600 s. The larger errors observed here are probably caused by the 20-minute delay between BSE calibration at t = 0 s and RB measurement. Nevertheless, the residual slope is only notable because it equals or exceeds the RB value produced by the sensor. As before, curves in **Fig. 2.11** are shifted by small amounts (noted in the legend) for direct comparison to **Fig. 2.10** and **Fig. 2.7d**, but the shifts are irrelevant since no RB was detected.

This analysis clarified numerous ways that Device RG2H-06-183 was anomalous. Bringing its data points into a range comparable to the other devices required an *ad hoc* shift of 0.15 V that cannot be justified in comparison to the other offset magnitudes or the intercepts reported in **Table 2.6**. Device RG2H-06-183 also had the highest residual slope in $I_{sd}(t)$ at the conclusion of correcting for BSE currents, though slope errors only partly accounted for remaining disagreements with other devices' results. The possible causes of these differences are varied. On one hand, Device RG2H-06-183 had the highest current of the four sensors and the weakest response to gating (**Table 2.4**), perhaps indicating intrinsic differences among gFET sensors that requires device-specific normalization. Device RG2H-06-183 was also the first device probed, the only device measured at a negative V_{lg}, and the only device measured in a nonmonotonic order, all of which add uncertainty to its data.

2.4.5 Interpretation of the IL-6 assay results

To summarize, correction of the $I_{sd}(t)$ recordings to account for slow, electrochemical currents induced by V_{lg} produced new results for TSA and RB. TSA was successfully detected at all $V_{lg} > 0$ V, with an asymptotic decrease to zero response for $V_{lg} < 0$ V. After correcting for the electrochemical currents, no RB was observed under any condition.

The absence of RB forces one of two conclusions about IL-6 antibody-antigen interactions: either (1) antigen dissociation ran to completion in the 600 s period allowed for dissociation, or (2) specific antigen binding to IL-6 antibodies was inhibited or undetectable by the Cardea sensor. The former hypothesis of fast dissociation is contradicted by other assay results [12,53], and there is no clear evidence of a second exponential decay (i.e. slower than electrochemical charging) in the BSE-corrected $I_{sd}(t)$. The latter hypothesis, on the other hand, is supported by the successful reuse of devices over 3 or 4 cycles of testing and, more generally, by Cardea's long-term success reproducing IL-6 assay results.

This analysis concludes that weakly-bound, nonspecific surface adsorption generated the entire TSA signal. The strong dependence of TSA on V_{lg} suggests an electrostatic mechanism in which the applied potential inhibited surface adsorption at $V_{lg} < 0$ V and enhanced adsorption at $V_{lg} > 0$ V. The turning point at 0 V was a consequence of the measuring apparatus, which defined potential with respect to the gFET channel. At $V_{lg} < 0$ V, the liquid is negative relative to the graphene surface and antigen is electrostatically repelled. At $V_{lg} > 0$ V, the liquid is positive relative to the graphene, enhancing antigen concentration and nonspecific adsorption at the surface. If correct, opposite results should be observed with other antigen-antibody pairs having negatively charged antigens.

In principle, applied potentials might also affect the association and dissociation rate constants for specific binding, but no evidence of specific binding was observed in this study.

Probing the binding kinetics will require conclusive RB signals, in which case sensor reuse and controlled variation of V_{lg} both become more challenging experimental aspects.

2.5 Conclusions and Future Work

Initial measurements of TSA and RB demonstrated the signal variation between devices (see **Fig. 2.7**). At all V_{lg}, raw TSA and RB values varied by up to 2 % between devices. However, measurements at multiple V_{lg} revealed that the signal variation could be corrected for with artificial shifts in V_{lg}. After shifts in V_{lg} were applied, results between different devices aligned, confirming that the primary source of signal variation was variation in response to applied V_{lg}, likely resulting from variation in graphene surface potentials. Furthermore, the amount of V_{lg} shift required for alignment of results is a quantitative measure of the variation in graphene surface potentials.

Measurements at different V_{lg} also revealed the need to consider and account for electrochemically induced currents. Raw $I_{sd}(t)$ contained dI_{sd}/dt as large as -2 % per 600 s at most ZCP, TSA and RB measurement points (See **Table 2.5**). This nonzero dI_{sd}/dt resulted from slow electrochemical charging and indicated that the gFET, whether it be the graphene channel surface or underlying SiO_2, had not reached equilibrium at each measurement time. As a measure of these electrochemically induced currents, BSE was empirically defined to be dI_{sd}/dt at the ZCP. When projected to t = 600 s and t = 1200 s, BSE currents were one quarter to one third as large as raw TSA values and equal to or larger than raw RB values. Corrected TSA and RB values were calculated by subtracting projected BSE from raw TSA and RB values, resulting in a more reliable measure of TSA and RB. Variation in BSE currents between devices also appeared to result from variation in graphene surface potentials (see **Fig. 2.9**), though the differences in BSE currents were not in complete agreement with the variation seen in TSA and RB values.

After correcting for electrochemically induced currents and variation in gating between devices, (i) TSA was found to depend on applied potentials and (ii) there is no measurable RB (See **Table 2.7** and **Table 2.8** and **Fig. 2.10** and **Fig. 2.11**). Corrected TSA magnitudes monotonically increase with increasing applied potentials, with an average d(TSA)/dV_{lg} of -17 % per volt at $V_{lg} \geq 0.2$ V, and asymptotically decrease to zero at $V_{lg} \leq 0.1$V. This indicates that increasing applied potentials promote total antigen adsorption to the graphene channel surface. This is possibly explained by a simple electrostatic mechanism: $V_{lg} > 0$ V causes the liquid to be positively charged with respect to the graphene channel and electrostatically drives antigen to the surface, while $V_{lg} < 0$ V instead causes the liquid to be negatively charged and antigen is electrostatically repelled from the surface. Furthermore, the dependence of TSA on V_{lg} confirms that applied potentials can be tuned to produce similar TSA values between devices, reducing or eliminating signal variation.

On the other hand, raw RB signals were found to result entirely from BSE signals. The absence of measurable RB indicates that specific antigen binding to IL-6 antibodies was inhibited or undetectable by Cardea's biosensor. At first glance, this result appears to disagree with past results using Cardea's IL-6 protocol where nonzero RB signals are reported. However, the work here shows that BSE currents are present at all V_{lg} (See **Table 2.5**), which means that BSE currents are also present in Cardea's reported results, which are not accounted for. Furthermore, corrections for BSE currents reduce RB signals to zero. Since Cardea does not perform this correction, it is likely that similar corrections for BSE currents will reduce their reported RB signals to zero as well.

While this work was successful investigating the signal variation and effects of applied potentials in performing Cardea's IL-6 assay on their biosensor, there are still concerns to be

addressed. First, Cardea's Agile R100 typically reports TSA magnitudes of 15 % ± 3 %, while the measurements here had a maximum TSA magnitude of 5 %. The choice was made here to use an external liquid probe to control V_{lg}, and future measurements instead using the on-chip Pt electrodes to control liquid potential may be able to attribute the discrepancy in TSA values to the method of V_{lg} control. Alternatively, applying higher potentials (V_{lg} > 0.4 V) may produce TSA values in better agreement with Cardea's Agile R100 system if the dependence on V_{lg} continues.

Secondly, while Cardea's biosensor did not report any significant RB signals (corrected RB magnitude < 1 % at all V_{lg}, see **Table 2.8**), it is unclear if this results from device limitations or if this result is specific to the IL-6 antibody-antigen pair. A different antibody-antigen pair should be used to test the ability of Cardea's biosensor to measure specific antibody-antigen binding. Furthermore, measurements using an oppositely charged target antigen will also test the postulated electrostatic mechanism of V_{lg} dependence.

Lastly, it would be beneficial to better characterize and correct for electrochemically induced currents (BSE), as they proved to be quite significant in the proper measurement and interpretation of the signals of interest, TSA and RB (see **Table 2.5**). The corrections applied here for electrochemically induced currents assumed that BSE was constant in time, which appeared to be correct in most cases through t = 600 s (see **Table 2.7**), but resulted in residual dI_{sd}/dt at t = 1200 s. Longer calibration times (Δt > 2400 s) in buffer following voltage changes will allow more accurate measurement of BSE currents over time, which in turn, may lead to more accurate corrections. The longer calibration periods may also inherently eliminate the need for corrections if BSE currents reduce to zero over longer time periods.

Chapter 3

Discrimination of Single-Point Mutations in Unamplified Genomic DNA via Cas9 Immobilized on a Graphene Field-Effect Transistor

Simple and fast methods for the detection of target genes with single-nucleotide specificity could open up genetic research and diagnostics beyond laboratory settings. We recently reported a biosensor for the electronic detection of unamplified target genes using liquid-gated graphene field-effect transistors employing an RNA-guided catalytically deactivated CRISPR-associated protein 9 (Cas9) anchored to a graphene monolayer. Here, using unamplified genomic samples from patients and by measuring multiple types of electrical response, we show that the biosensors can discriminate within one hour between wild-type and homozygous mutant alleles differing by a single nucleotide. We also show that biosensors using a guide RNA–Cas9 orthologue complex targeting genes within the protospacer-adjacent motif discriminated between homozygous and heterozygous DNA samples from patients with sickle cell disease, and that the biosensors can also be used to rapidly screen for guide RNA–Cas9 complexes that maximize gene-targeting efficiency.[1]

3.1 Introduction

Single-nucleotide polymorphisms (SNPs) account for over 50 % of disease-causing mutations in humans [54-56]. In addition to residing at the core of human health genetics, SNPs

[1] Reprinted with permission from "Discrimination of Single-Point Mutations in Unamplified Genomic DNA via Cas9 Immobilized on a Graphene Field-Effect Transistor" by S. Balderston, J. Taulbee, E. Celaya, et al. *Nature Biomedical Engineering* (2021). Copyright, Springer Nature.

play a considerable role in infectious disease prevention [57-59], ageing [60], pharmacology [61-63] and agriculture [64] and are a driving force in evolutionary change. Specific SNPs have been associated with reducing the rubella vaccine's effectiveness by impinging on key cytokine pathways [65,66]. SNPs were also implicated in an outbreak of coronavirus, causing severe acute respiratory syndrome (SARS) [67-69]. It was discovered that the virus was replicating in populations of palm civets in China [70,71], and sequencing of the gene transcribing the spike protein (that is, the protein necessary for the virus infection of host cells) revealed 27 nucleotide variations, which were indicative of the virus's new ability to infect humans [71]. A correlation between the hallmarks of human ageing and three SNPs in the circadian rhythm *CLOCK* gene has also been reported [60]. Furthermore, SNPs resulting in amino acid variations in proteins, which interact with a mutant protein, may affect a patient's prognosis, as exemplified in cystic fibrosis [72]. In drug metabolism, SNPs are particularly important for personalizing pharmaceutical therapy as they can serve as markers for a patient's metabolic capacity for a specific drug [73]. One example of this is two concomitant SNPs in two cytochrome p450 (*CYP*) genes that have been implicated in paediatric drug-resistant epilepsy [74]. In the agriculture industry, it is crucial for crop yield to plant seeds with the highest possible resistance to common pathogens. SNPs play an essential role in determining breeding procedures as they serve as markers for resistance screening [75-77]. Furthermore, SNPs can be used as genome stability markers for quality control of genetically modified seeds before their release [78]. Although the applications for SNP detection are abundant across many research disciplines and industries, current methods for SNP genotyping have limited their widespread employment outside of a traditional laboratory.

The current gold standards for massive SNP genotyping involve SNP microarrays, TaqMan SNP genotyping or next-generation sequencing [79-83]. Although many of these technologies are

high throughput and have allowed for advancement in research and industry, they all require DNA amplification, experienced technical staff, tedious design of paired primer systems, and fluorescent probes, all of which are not amenable with mass testing at the point of care or in the field. Furthermore, all of these methods require sophisticated optical equipment, which restricts the capability of laboratories for DNA sequence determination, thus severely limiting the ability to design hand-held, rapid, point-of-testing instrumentation. Amplification-free electronic detection of a target gene with SNP specificity has the potential to streamline this process, allowing for mass testing for SNPs outside of a traditional laboratory.

We have previously reported on a label-free technology based on a graphene field-effect transistor (gFET) that is capable of discriminating between target and non-target genes from unamplified genomic DNA samples [14]. Here, we report a new CRISPR-based gFET system, termed CRISPR-SNP-Chip, referred to as SNP-Chip hereafter, which is capable of detecting single-nucleotide mutations in a given DNA sequence without the need for target amplification. This was accomplished by: (1) expanding the types of electrical measurements taken; and (2) incorporating different Cas9 variants and orthologues to improve SNP discrimination. In this work, we record I, C and V responses to be able to detect SNPs. This expansion of measurement type has allowed us to reach single-nucleotide specificity. Furthermore, the incorporation of a novel Cas9 orthologue has allowed us to distinguish between samples with different zygosity of a particular SNP. SNP-Chip consists of a liquid-gated gFET where the graphene channel between the source and drain electrodes is functionalized with a CRISPR-associated (Cas) enzyme complexed with a target-specific guide RNA (gRNA) to capture a specific DNA sequence contained within unamplified genomic DNA [81-83]. Electrical measurements are obtained by sweeping the liquid gate voltage from −100 mV to +100 mV while the source–drain current is

measured continuously at constant source–drain voltage. Molecular adsorption and electrostatic interactions at the graphene surface create local potentials that effectively gate and alter gFET electrical properties, such as conductance, source–drain current, transconductance and the effective gate potential seen by the graphene channel. As a result, the interaction between the RNA-guided Cas nuclease and its DNA target is detectable as a change in one or more of these gFET properties, which are measured simultaneously and in real time.

The sensitivity and specificity of SNP-Chip depend on the DNA-targeting capability of Cas enzymes anchored to the graphene channel. Cas9, the most widely used Cas enzyme, is complexed with a gRNA molecule with a spacer of ~20 nucleotides complementary to a specific DNA sequence [84,85]. This complex interacts with DNA by recognizing protospacer-adjacent motifs (PAMs). When the RNA-guided Cas9 interacts with its PAM, it begins to unwind the DNA upstream of the PAM, and hybridization between the spacer sequence of the gRNA and the DNA target occurs, followed by cleavage of the DNA strand. In the absence of complementarity between the spacer and the DNA, the DNA is more likely to dissociate from the Cas9–gRNA complex [86,87].

We previously reported a DNA sequence-detecting device that used dCas9, a dead variant of Cas9 that is nuclease inactive [14,88,89]. Except for DNA cleavage, this general mechanism is consistent between dCas9 and Cas9 [84-86]. Studies have shown that Cas9 remains bound to its target DNA after cleavage [90]. Therefore, the nuclease-active wild-type Cas9 and high-fidelity Cas9 enzymes can also be used within the SNP-Chip construct to detect a specific DNA sequence. Incorporating different Cas enzymes can improve this technology's performance by tuning the SNP-Chip specificity and selectivity [91-95]. For example, high-fidelity Cas9 has been reported

to mediate highly specific correction of the sickle cell disease (SCD)-associated SNP mutation in haematopoietic stem and progenitor cells of patients with SCD [96].

SNP-Chip was constructed by expanding the electronic analysis of the gFET and utilizing dCas9, Cas9 or a Cas9 orthologue to enable amplification-free electronic detection of point mutations. These studies indicated that the accuracy and SNP discrimination efficiency of Cas enzymes could be captured by accurate analysis of the gFET electrical responses. In the present study, we utilized these Cas enzymes to detect SNPs in target genes in two human disease models. In the first disease model, we tested an SCD-associated point mutation in the *HBB* gene of patients with and without the disease. SCD is a recessive heritable disease caused by an adenine to thymine base substitution within exon 1 of the *HBB* gene [97], resulting in a glutamate to valine amino acid switch in β-globin (E6V). This mutation renders β-globin prone to polymerization, causing the characteristic misshapen sickle red blood cells (RBCs) [98,99]. Sickle RBCs damage blood vessels and cause blockages, resulting in symptoms such as chronic pain, swelling, organ damage and stroke. Furthermore, patients often suffer from chronic anaemia due to the shortened lifespan of sickle RBCs [100]. These complications result in a reduction of life expectancy for patients with SCD by approximately 30 years [101,102]. Despite the associated decrease in quality of life and life expectancy, the sickle RBC trait (mutant haemoglobin S (HbS)) has persisted, particularly in malaria-endemic regions of the world such as East Africa [103]. We also tested amyotrophic lateral sclerosis (ALS) as an additional disease model by detecting a SNP in the *superoxide dismutase type 1* (*SOD1*) gene in genomic DNA extracted from human induced pluripotent stem cells (hiPSCs) from a healthy individual and an individual with familial ALS (fALS). ALS is a neurodegenerative disease characterized by the progressive loss of motor neurons in the cortex and spinal cord. This degeneration leads to death due to respiratory failure within 3–5 years [104].

Approximately 90 % of all ALS cases are sporadic, occurring randomly without known specific causes and genetic background. However, about 10 % of cases are hereditary and familial and are caused by single-gene mutations [105]. fALS is deeply associated with *SOD1* missense mutants such as A4V (where alanine is switched to valine at codon 4), A89V (where alanine is switched to valine at codon 89), H44R (where histidine is switched to arginine at codon 44) and G93A (where glycine is switched to alanine at codon 93). Any of these mutations may trigger a toxic mechanism involving redox catalysis, which results in misfolding of the SOD1 protein [106,107].

Recently, CRISPR-based gene editing has been utilized for the potential treatment of both SCD and ALS [108-112]. Although promising, CRISPR-based gene editing requires careful assessment of CRISPR complex design and editing efficiency [113,114]. Therefore, technologies that can detect, quantify and discriminate between different wild-type and mutated gene targets in a facile and high-throughput manner can be essential in designing better CRISPR complexes with optimal efficiency to improve the effectiveness of ex vivo genome editing in cell populations before they are reintroduced to a patient's body [109,115].

In recent years, technologies have been developed for SNP genotyping to bypass the need for advanced sequencing techniques. Although some of these technologies have removed the need for expensive and bulky optical equipment [116] and have bypassed the need for amplification [117], none have done both. SNP-Chip is a CRISPR-powered transistor capable of amplification-free detection of target DNA sequences with SNP specificity by combining the power of CRISPR and gFET technology, overcoming the limitations associated with other amplification and optical-based SNP genotyping methods. SNP-Chip is a flexible, label-free technology that can easily be reconfigured through the programmability of CRISPR to target other point mutations, broadening SNP-Chip's potential applications beyond SCD and ALS.

3.2 Methods

3.2.1 AFM

AFM images of the graphene FET chip surfaces were acquired in 20 μm × 20 μm areas with 512 pixel × 512 pixel resolution and a scan rate of 0.5 Hz in non-contact, tapping mode using the Pacific Nanotechnology Nano-R2 scanning probe microscope. Images were analysed using Gwyddion.

3.2.2 dCas9, Cas9 and MgaCas9 gRNA Design

Multiple gRNAs were designed for SCD detection on SNP-Chip. gRNA-HTYa targets the sequence 5′-GTAACGGCAGACTTCTCCTC-3′ and is specific to the wild-type HbA *HBB* allele, which does not contain the single-point mutation associated with SCD. Briefly, it has previously been reported that gRNA-HTYa facilitates the cleavage of the *HBB* target sequence [118]. gRNA-SCDa targets the sequence 5′-GTAACGGCAGACTTCTCCAC-3′ and is specific to the HbS sickle cell trait, which contains the single-point mutation associated with SCD. For both gRNA-HTYa and gRNA-SCDa, the SCD-associated SNP locus occurs in the second nucleotide of the protospacer sequence proximal to the PAM. Both gRNA-HTYa and gRNA-SCDa are compatible with dCas9 and Cas9 [88]. The third gRNA, which is compatible with MgaCas9 (CasZyme), targets the wild-type HbA allele. This MgaCas9 gRNA targets the sequence 5′-GACACCATGGTGCATCTGACTC-3′. The MgaCas9 gRNAs used in this study were synthesized by in vitro transcription using HiScribe T7 Quick High Yield RNA Synthesis kits (New England Biolabs (NEB)) and purified using the Monarch RNA Cleanup Kit (NEB). RNA concentration and purity were measured using a NanoPhotometer NP80 (Implen), and RNA

integrity was visualized by 2 % agarose electrophoresis. One gRNA was designed for the ALS model. This gRNA targets the sequence 5′-CATGAACATGGAATCCAAGC-3′ and was ordered from Synthego without modification.

3.2.3 DNA Cleavage Assay

MgaCas9 (CasZyme) was purified and 50 µl MgaCas9–gRNA complex was assembled by incubating 0.08 µM MgaCas9 and 0.16 µM Cas9 gRNA in assembly buffer (10 mM Tris-HCl, 100 mM NaCl, 1 mM ethylenediaminetetraacetic acid (EDTA) and 1 mM dithiothreitol (pH 7.5)) at 20 °C for 1 h. Then, 50 µl 5 nM target DNA in 1× CutSmart Buffer (NEB) was also prepared and heated to 37 °C. A 20 µl 1:1 vol/vol mix of preheated target DNA mix and MgaCas9–gRNA complex was incubated for 30 min at 37 °C. Afterwards, 5.6 µl 6× Gel Loading Dye, Blue (NEB) was added to the reaction. Cleavage was visualized via 1 % agarose gel electrophoresis. The complex is considered active if 40 nM of the complex cleaves 100 % of 2.5 nM DNA within 30 min at 37 °C and if 20 nM of the complex cleaves at least 80 % of 2.5 nM DNA within 30 min at 37 °C.

Purified Cas9 (MacroLab) was complexed with gRNA-CS04 by mixing 50 µl 80 nM Cas9 and 80 nM gRNA in Assembly Buffer (10 mM Tris-HCl, 100 mM NaCl, 1 mM EDTA and 1 mM dithiothreitol (pH 7.5)) at 20 °C for 1 h. Then, 50 µl 10 nM target DNA in 1× CutSmart Buffer (NEB) was also prepared. A 20 µl 1:1 vol/vol mix of preheated target DNA mix and Cas9–gRNA complex was incubated for 30 min at 37 °C. Afterwards, 5.6 µl 6× Gel Loading Dye, Blue (NEB) was added to the reaction. The reaction was then incubated at 85 °C for 10 min. The reaction was run on a 10% polyacrylamide gel (Bio-Rad) for 45 min at 110 V and stained with SYBR Gold. The band intensity was quantified with ImageJ.

3.2.4 Clinical DNA Samples

Human genomic samples were obtained with a certificate of analysis from the Coriell Institute for Medical Research. The HbAA sample (NA03798) was from a 10-year-old healthy Caucasian male. The HbSS sample (NA16265) was from a 19-year-old African American male homozygous for SCD. The HbA/HbS sample (NA20838) was from a 35-year-old African American female heterozygous for the SCD trait. The concentrations were routinely measured before use via Nanodrop One (Thermo Scientific).

3.2.5 Culture of hiPSCs and Mutation Screening

hiPSCs (WTC11) were obtained through the University of California, Berkeley Cell Culture Facility. The *SOD1*-mutated fALS iPSCs (CS04) were obtained from the Cedars-Sinai Medical Center (Los Angeles, California). All hiPSCs were maintained on plates coated with Vitronectin (Life Technologies) and cultured in Essential 8 Medium (Life Technologies) at 37 °C under a 5 % CO2 atmosphere. All hiPSCs were passaged every 7 d by 0.5 mM EDTA (Life Technologies). Genomic DNA was extracted using DNeasy Blood & Tissue kits (Qiagen) according to the manufacturer's instructions. For PCR amplification of the H44R region in *SOD1* (NM_000454.5), the following primers were used: 5′-GGGTGCTTGTGCATTGAGTG-3′ (forward) and 5′-GGGTTTTAACGTTTAGGGGCT-3′ (reverse). The PCR protocol can be found in the 'PCR amplification' section below. The products were directly sequenced using the 3130 Genetic Analyzer (Applied Biosystems).

3.2.6 PCR Amplification

The following PCR protocol was used to amplify a 504-bp region of the *HBB* gene from both HbAA and HbSS gDNA templates: 50 ng genomic DNA (NA03798 or NA16265), 1× Phusion HF Buffer, 200 μM dNTP, 0.5 μM forward primer, 0.5 μM reverse primer and 1 U Phusion DNA polymerase (NEB). The final volume of the PCR reaction was 50 μl. The forward and reverse primer sequences were 5′-TTGAGGTTGTCCAGGTGAGCCA-3′ and 5′-GGCCAATCTACTCCCAGGAGCA-3′, respectively. The following thermal cycler protocol was used: (1) 98 °C for 30 s; (2) 98 °C for 10 s; (3) 63.5 °C for 30 s; (4) 72 °C for 15 s; (5) repeat steps 2–4 29 times; and (6) hold at 72 °C for 5 min before cooling to 4 °C. HbAA and HbSS sequences were validated via Sanger sequencing using the same primers mentioned previously. Sanger sequencing was performed by the University of California, Riverside Gene Core.

A luciferase-transgenic HEK293 cell line (Luc14 HEK293) [119] was used to amplify a 565-bp negative control sequence via a nested PCR protocol. This amplicon did not contain the gRNA-HTYa or the gRNA-SCDa target sequences. The forward and reverse primer sequences for the first PCR were 5′-GCTCACTCATTAGGCACCCC-3′ and 5′-GGCGTTGGTCGCTTCCGGAT-3′, respectively. For the second (nested) PCR, the forward and reverse primer sequences were 5′-CACTTTATGCTTCCGGCTCG-3′ and 5′-CCGCGTACGTGA TGTTCACC-3′, respectively. All amplicons were confirmed on a 1 % agarose gel, stained with 0.5 μg ml^{-1} ethidium bromide for 30 min and imaged using UVP ChemStudio (Analytik Jena). All final PCR-derived amplicons were purified using a PureLink PCR Purification Kit (Invitrogen) before SNP-Chip experiments.

A 2,058-bp DNA fragment for the MgaCas9 cleavage assay was obtained by PCR using as a template HEK293 (ATCC; CRL-1573) genomic DNA and a 5′-TCCTGAGACTTCCACACTGATGC-3′ and 5′-TGCACAGAGCACATT GATTTGT-3′ primer

pair. The PCR product was purified using Monarch DNA Cleanup and Gel Extraction (NEB). The MgaCas9–gRNA complex cleaves a 1,305-bp DNA substrate to generate 736- and 569-bp products.

A 417-bp region of the *SOD1* gene encompassing the H44R SNP locus was amplified from 50 ng template CS04 and WTC11 genomic DNA using the Phusion High-Fidelity PCR Kit (NEB). Reactions were prepared according to the manufacturer's protocol. The forward and reverse primer sequences were 5′-GGGTGCTTGTGCATTGAGTG-3′ and 5′-GGGTTTTAACGTTTAGGGGCT-3′, respectively. The following PCR protocol was used: (1) 98 °C for 3 min; (2) 98 °C for 10 s; (3) 62 °C for 30 s; (4) 72 °C for 15 s; (5) repeat steps 2–4 34 times; (6) 72 °C for 10 min; and (7) hold at 4 °C.

3.2.7 SNP-Chip gFET Functionalization via Molecular Linker Absorption, Activation, Cas Enzyme Coupling, Passivation and Cas–gRNA Complex Formation

For the amplicon studies, gFETs (Cardea) were rinsed with 30 µl acetone twice, followed by two rinses with 30 µl deionized water. The chips were subsequently functionalized with PBA (5 mM; 15 µl; Sigma–Aldrich) in dimethylformamide (DMF) for 2 h at room temperature. Following the incubation, the gFETs were rinsed twice with 30 µl DMF, followed by 30 µl deionized water. The functionalized PBA gFETs were then air dried and used immediately or stored at 4 °C for later use. PBA was activated using a 1:1 vol/vol ratio of *N*-(3-dimethylaminopropyl)-*N*′-ethyl carbodiimide hydrochloride (EDC, 4 mM) and *N*-hydroxysuccinimide (NHS; 11 mM; Sigma–Aldrich) in 50 mM 2-(*N*-morpholino)ethanesulfonic acid (MES; pH 6) for 5 min at room temperature before incubation with Cas enzyme [120,121]. Cas enzymes (900 ng in 30 µl 2 mM $MgCl_2$) were incubated atop the gFET for 15 min, after which

the gFET was rinsed twice with 30 µl MES (pH 6). Any uncoupled PBA molecules on the graphene surface were then blocked using amino-PEG5-alcohol (1 mM; 10 min) and ethanolamine hydrochloride (1 M; 10 min). The surface was then rinsed five times with 2 mM $MgCl_2$ to remove any unbound blocking agent for 1 min. The chips were then calibrated for gRNA using 2 mM $MgCl_2$ for 5 min. gRNA (900 ng in 30 µl 2 mM $MgCl_2$) was then incubated on the gFET for 10 min at 37 °C. The surface was then rinsed with 2 mM $MgCl_2$ to remove any unbound gRNA for 5 min. The distribution of the biofunctionalization signals can be found in **Figure A.1**.

For the genomic studies, gFETs (Cardea) were rinsed with 30 µl acetone followed by 30 µl deionized water twice. The gFETs were subsequently functionalized with PBA (750 mM; 15 µl; Sigma–Aldrich) in DMF for 1 h at room temperature. Following the incubation, the gFET chips were rinsed with 30 µl DMF followed by 30 µl 70 % ethanol twice and 30 µl 100 % isopropyl alcohol. The functionalized PBA chips were then air dried and used immediately or stored at 4 °C for later use. PBA was activated using a 1:1 vol/vol ratio of EDC (200 mM) and NHS (400 mM) (Sigma–Aldrich) in 50 mM MES (pH 6) for 5 min at room temperature before incubation with Cas enzymes. Cas enzymes (900 ng in 2 mM $MgCl_2$) were incubated atop the gFET for 15 min, after which the gFET was rinsed twice with 30 µl MES (pH 6). Any uncoupled PBA molecules on the graphene surface were then blocked using amino-PEG5-alcohol (1 mM; 10 min) and ethanolamine hydrochloride (1 M; 10 min). The surface was then rinsed five times with 2 mM $MgCl_2$ to remove any unbound blocking agent for 1 min. The chips were then calibrated for gRNA using 2 mM $MgCl_2$ for 5 min. gRNA (900 ng in 2 mM $MgCl_2$) was then incubated on the chip for 10 min at 37 °C. The surface was then rinsed with 2 mM $MgCl_2$ to remove any unbound gRNA for 5 min.

3.2.8 SNP-Chip Calibration and DNA Detection on Functionalized gFETs

To compare sensor responses from different devices, each chip was incubated in a solution of 2 mM $MgCl_2$ for 5 min immediately before the introduction of DNA to allow for equilibration of the graphene surface, which we refer to as sensor calibration. All signals following calibration were calculated and expressed as a percentage change from the final signal during calibration. DNA samples were then incubated atop the gFET for 25 min (30 ng μl^{-1} in 2 mM $MgCl_2$ for the amplicon studies and 60 ng per 30 µl in 2 mM $MgCl_2$ for the genomic DNA studies). Any unbound DNA was then rinsed with 2 mM $MgCl_2$ for 15 min. Cas9 and MgaCas9 genomic DNA was rinsed for an additional 5 min. All steps in the assay were performed at 37 °C. The temperature was controlled with a benchtop incubator.

3.2.9 Sensitivity and Specificity Studies

Sensitivity studies were performed by incubating varying concentrations (10–60 ng μl^{-1}) of HbAA genomic DNA (NA03798). These were then tested on the SNP-Chip Cas9-HTYa construct according to the protocol defined in the section ‘SNP-Chip calibration and DNA detection on functionalized gFETs’. Specificity studies were performed by creating non-homogeneous mixtures of HbAA (NA03798) and HbSS (NA16267) genomic DNA, all of which had a final concentration of 60 ng μl^{-1}. These were then tested on SNP-Chip Cas9-HTYa and MgaCas9–22-nucleotude gRNA constructs according to the protocol defined in the section ‘SNP-Chip calibration and DNA detection on functionalized gFETs’.

3.2.10 Blind Studies

SNP-Chip blind studies were performed by first obtaining three genomic DNA samples each from healthy patients (NA03798, NA22807 and NA23904) and patients with SCD (NA16265, NA16266 and NA16267) from the Coriell Institute for Medical Research. Samples were tested and analysed blind. For all other electrical measurements presented in this manuscript, technical replicates were employed. This was due to the nature of this work and the importance of sensor reproducibility. In the blinded studies, we employed biological replicates by assaying samples with either healthy or diseased phenotypes.

3.2.11 SNP-Chip Sensor Response, Measurement and Analysis Methods

The Agile R100 reader system (Cardea) was used for all measurements using the standard electrical setting. Each chip consisted of three transistors (gFETs) using a shared counter and reference electrodes. Each transistor consisted of five graphene channels in parallel. The gate voltage was swept from −100 to +100 mV continuously, at a constant rate, while the source–drain current through each transistor was monitored and recorded in real time. I, C and V response values were calculated for each cycle of a triangular gate loop and were always referenced to a calibration step before the addition of DNA. The I response was calculated by averaging the raw source–drain current data over each period of the liquid gate triangle wave. I response signals are shown here as percentage changes. The C response is the percentage change in the slope of the gFET transfer curve relative to a calibration step. The C response is calculated once per gate loop. The $\frac{dI}{dV_g}$, the derivative of current with respect to gate voltage is evaluated using the forward finite difference approximation to the derivative. For each step in the cycle, the initial current value is subtracted from the ending current value and the result is divided by the change in gate voltage. The average

of all slope values for a cycle is taken to yield the C response value for that cycle. Prior to analysis, the C response is calibrated by dividing by the C response at an initial calibration point, subtracting 1 and multiplying by 100 to convert to percent change. Changes in the C response are probably dominated by changes in the capacitance between the graphene channel and the liquid as material binds to the surface. V response values were calculated by dividing the by dividing the I response by the C response for each gate loop cycle and multiplying by 100 as a unit correction. Prior to analysis, the V response is calibrated by subtracting the value at an initial calibration point. Following our previous work describing the device physics of these sensors [12], this value is presented as the percentage difference relative to the calibration step. This value is like the Dirac voltage shift or, more generally, a transistor threshold voltage shift, but is a calculated value rather than a measured value and should not be taken to imply an actual voltage measurement on the surface.

Agile Plus software (Cardea) was used to run the Agile R100 reader system. Approximately 10 % of transistors failed during measurement due to one or more graphene channels open circuiting. The software detected these failures as instantaneous drops of 15 % or more in the source–drain current. The remaining 90 % of devices measured were analysed using Python scripts and KNIME workflows to calculate capacitance and effective gate potential data. The statistics were calculated using Prism, assuming a normal distribution of the data.

3.2.12 Reproducibility of the SNP-Chip Studies

The SNP-Chip studies were performed by two researchers to ensure the reproducibility of the results. It is clear from all of the sensing data presented in this paper that assuming a normal distribution results in a calculated error that is larger than the true variations in the sensing signals.

Some variations present in the sensing data are recognizable across multiple datasets. One potential source of variation is the biofunctionalization (that is, the immobilization of Cas9 and gRNA on the surface of the gFET). We have provided data (**Figure A.2**) that characterize the variation in immobilization signal of both Cas9 and gRNA. This implies that future research could produce calibration or process techniques that could improve the statistics of the overall measurement system. We show one approach to addressing this here: increasing the specificity of the core biochemical system. This opens promising areas for future studies to enhance sensor sensitivity further.

3.3 Results

SNP-Chip consists of a gFET fabricated using a commercial microelectromechanical system foundry, as previously described [12]. SNP-Chip uses a reader and a cartridge connected to a computer and analysis software [12,14,122,123]. The graphene channel, between the source and drain electrodes, is decorated with Cas enzymes via a chemical linker, 1-pyrenebutanoic acid (PBA). The chemical linker, which π–π stacks with the graphene, is chemically activated via standard carbodiimide chemistry to covalently attach the Cas enzyme to the graphene surface [14,123]. Once the enzyme is immobilized, the graphene surface is passivated with poly(ethylene glycol) (PEG) amine and ethanolamine [14,124]. The Cas enzyme immobilized on the channel forms a complex with a gRNA, which is designed to: (1) bind to the Cas enzymes; and (2) target the DNA locus containing either the SCD-associated SNP or the ALS-associated SNP. The fully functionalized SNP-Chip is calibrated, then unamplified DNA samples are incubated atop the graphene surface during continuous data acquisition. The Cas–gRNA complex interacts with the different PAMs contained within the DNA via three-dimensional diffusion [90,125,126]. In the

presence of the target-adjacent PAM, complete hybridization can occur, leaving the DNA containing the complementary sequence anchored to the surface of the graphene via the Cas–gRNA complex. In the case of DNA targets containing mismatches, the Cas–gRNA complex has less affinity for the DNA and the DNA will dissociate from the surface of the graphene altogether [87,125,127]. After incubating the DNA atop the graphene channel, the gFET is rinsed to remove non-specifically bound DNA from the graphene surface, allowing for the final signal read-out. A schematic demonstrating this workflow is shown in **Figure 3.1**.

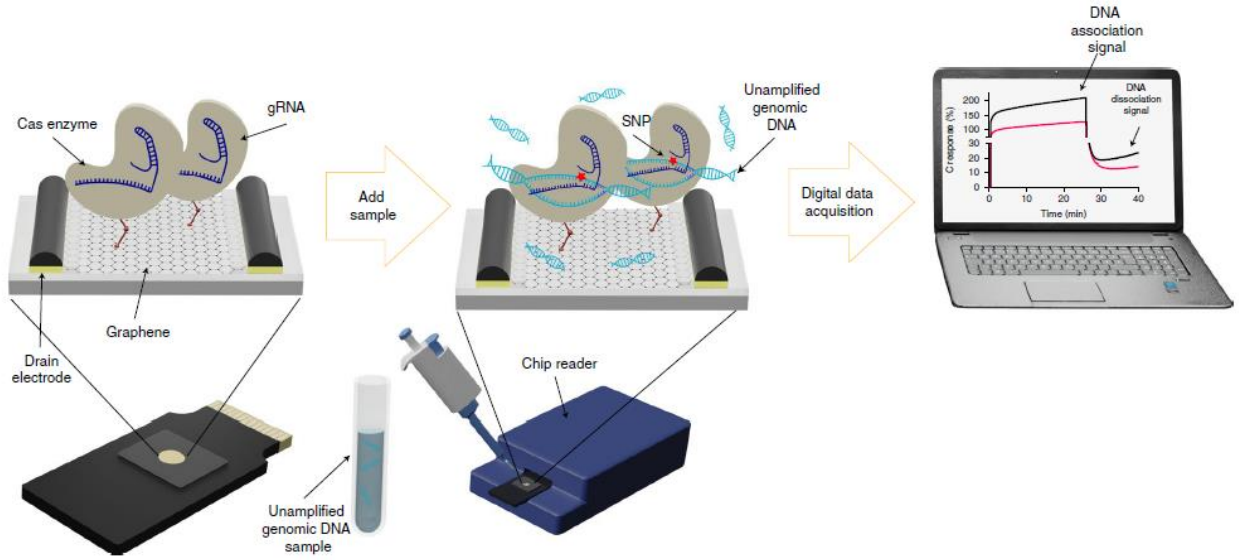

Figure 3.1. CRISPR-powered gFET for amplification-free detection of single-nucleotide mutations. SNP-Chip, the next generation of CRISPR-powered gFET,with expanded monitoring of multiple electronic parameters, can detect single-nucleotide differences within unamplified DNA samples. Through the CRISPR–Cas9 ribonucleic protein complex on its surface, this technology can digitally detect SNPs without labels or amplification. The target specific gRNA is designed to target single-nucleotide mutations relevant to two human disease models: SCD and ALS. Through real-time, multi-parameter and digital data acquisition, SNP-Chip can discriminate between unamplified genomic DNA samples in 40 min.

The SNP specificity of SNP-Chip depends on the highly specific recognition of target sequences by the Cas–gRNA complex, which requires thoughtful gRNA design. The DNA, unwound by the Cas enzyme, is probed by the gRNA spacer sequence upstream of the PAM,

starting at the 3′ end of the spacer [90,128]. It is within the first few nucleotides in the so-called seed sequence where Cas9 and dCas9 are most severely affected by mismatches. It has been observed that incomplete hybridization between Cas9–gRNA complexes and DNA within the spacer seed region often results in the dissociation of Cas9 from DNA altogether [123,125]. In fact, single nucleotides within the seed region of the gRNA, although having little impact on the DNA association, have been shown to increase the rate of DNA dissociation, from $< 0.006\ s^{-1}$ to $> 2\ s^{-1}$ [125]. Therefore, gRNA designs used for SNP-Chip analysis that distinguish between target and non-target DNA within the PAM or the seed sequence exhibit a high degree of specificity [125] because SNP-Chip can measure the DNA dissociation signals in addition to the association signals (**Fig. 3.1**).

To study the single-nucleotide sensitivity of SNP-Chip to detect mutation in the *HBB* gene, we first obtained DNA extracts from a healthy patient (denoted HbAA) who was homozygous for the wild-type HbA *HBB* allele and a patient with SCD (denoted HbSS), who was homozygous for the sickle cell allele (E6V mutation), termed the HbS. All clinical SCD-associated DNA extracts were obtained from commercially available B lymphocyte cells (Coriell Institute). SNP-Chip was functionalized with CRISPR complexes as described above. The primary gRNA design employed in this study has previously been validated for targeting and cleavage of the *HBB* gene using Cas9 [118]. This design was selected to maximize the difference in the affinity of the interactions that occur between the HbA and HbS alleles. This gRNA targets the HbA allele, which is adjacent to a 5′-AGG-3′ PAM. This healthy targeting gRNA, compatible with Cas9 and dCas9, is denoted gRNA-HTYa hereafter. The SCD-associated SNP is the second nucleotide on the PAM-proximal end of the spacer, well within the seed sequence (**Fig. 3.2a**). A second gRNA was designed to target the same protospacer sequence for the HbS allele. This gRNA, compatible with Cas9 and

dCas9, termed gRNA-SCDa, was used as a control for the amplicon SNP-Chip studies to ensure SNP-Chip specificity. Before SNP-Chip analysis, HbAA and HbSS genomic DNA samples were sequenced to: (1) confirm the absence or presence of the SCD-associated SNP in HbAA or HbSS samples; and (2) verify that the two protospacer sequences were present in the clinical DNA samples. To do this, we amplified a 504-base pair (bp) region of the *HBB* gene, encompassing all of exon 1, from both HbAA and HbSS DNA (**Fig. 3.2b**). The sequencing results shown in **Fig. 3.2c** indicate that the gRNA-HTYa and gRNA-SCDa protospacer sequences were found in HbAA and HbSS DNA, respectively, with the SCD-associated SNP present in the HbSS sample. Both sequences were directly adjacent to the Cas9 and dCas9 PAM sequence (5′-AGG-3′) [88,128].

To assess the capacity of SNP-Chip to discriminate between samples that differ by a single nucleotide, we first tested the assay with the HbAA and HbSS amplicons. A 565-bp region of the luciferase transgene from transgenic HEK293 cells was also amplified and used as a negative control [119]. Atomic force microscopy (AFM) analysis of the gFET was performed on dCas9 functionalized chips to ensure immobilization of dCas9 onto the surface of the graphene. **Fig. 3.2d** shows that dCas9 molecules decorate the surface of the graphene channel at a density of 1–2 molecules per μm^2. The immobilized dCas9 was then complexed with either gRNA-HTYa or gRNA-SCDa (**Fig. 3.2e**). Both SNP-Chip constructs, termed dCas9-HTYa and dCas9-SCDa, respectively, were calibrated, then the purified amplicon samples (30 ng μl^{-1}) were introduced to the gFET and incubated on the graphene channel for 25 min at 37 °C. After this incubation period, non-specifically bound DNA was washed away, and the final DNA signal was analysed relative to the calibration point as a percentage change. The SNP discrimination capability of the dCas9–gRNA SNP-Chip construct is reflected in multiple electrical properties of the gFET channel, reported as the I, C and V responses. **Fig. 3.2f** shows the calculated response based on the source–

drain current (I response) for both the dCas9-HTYa and dCas9-SCDa constructs after incubation with HbAA amplicons, HbSS amplicons or negative control amplicons. Each data point here represents a freshly functionalized transistor. In the presence of the HbAA amplicon, the dCas9-HTYa SNP-Chip construct had an average I response value of −9.6 %, representing a 2.5-fold increase compared with the negative control and a 1.4-fold increase compared with the SNP-containing HbSS amplicon. A similar separation was observed for the dCas9-SCDa SNP-Chip construct. In the presence of the HbSS amplicon, we saw an average I response value of −13.3 % (a 4.4-fold increase relative to the negative control and a 2.9-fold increase relative to the HbAA amplicon). The differences between fully complementary DNA targets (HbAA for gRNA-HTYa and HbSS for gRNA-SCDa) and negative control DNA for both constructs were determined to be significant ($P < 0.0001$) [14]. An appreciable difference was observed between DNA samples with and without the SCD-associated SNP. This difference was statistically significant for the dCas9-SCDa SNP-Chip construct ($P < 0.0001$).

Additional discrimination of analytes is possible by evaluating the C and V responses for this dataset. Like the trends observed for the I response, the C response yielded appreciable differences between HbAA and the SNP-containing HbSS amplicons for both SNP-Chip constructs (**Fig. 3.2g)**. When incubated with its target HbAA amplicon, the dCas9-HTYa construct showed an average response of 22.9 % (a 1.9-fold increase in the C response relative to the signal obtained from HbSS amplicons). Similarly, the dCas9-SCDa construct had a C response of 38 % (a 9.2-fold increase when incubated with its target HbSS amplicon compared with the HbAA amplicon). Although the variation observed for the C response was larger for the dCas9-SCDa construct, the difference between HbSS and HbAA DNA can still be considered statistically significant ($P < 0.0001$).

The percentage change in the effective gate potential of the graphene relative to calibration (the V response) is shown in **Fig. 3.2h** for both SNP-Chip constructs in the presence of HbAA, HbSS or negative control amplicons [12]. Overall, fully complementary amplicons for both dCas9 SNP-Chip constructs produced larger-magnitude V response signals compared with amplicons containing the single-nucleotide mismatch. The average complementary response for dCas9-HTYa was −26.2 % and the average complementary response for dCas9-SCDa was −37.0 % The control and mismatched samples showed average responses with magnitudes of 24.9 % or less. These differences (between complementary and control amplicons and between complementary and mismatch-containing amplicons) were statistically significant ($P \leq 0.03$), consistent with the results observed for I and C responses.

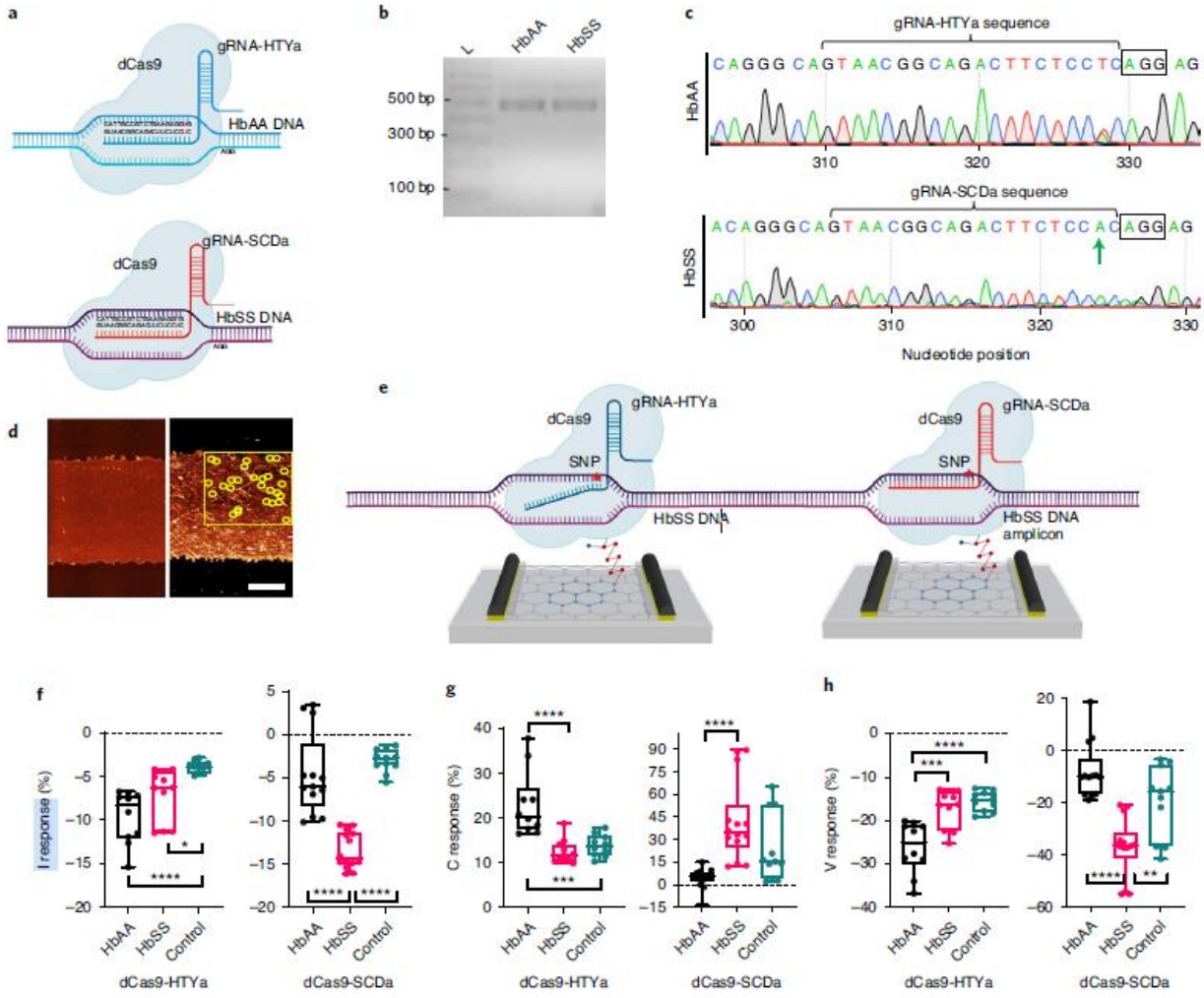

Figure 3.2. (**a**) gRNA-HTYa was selected to target the HbA allele of the *HBB* gene such that the SCD-associated SNP locus was the second nucleotide upstream of the PAM. The SCD-associated SNP locus is highlighted in red. As a control for the amplicon studies, gRNA-SCDa was designed to target the HbS allele of the *HBB* gene at the same locus as gRNA-HTYa. (**b**) 504-bp DNA samples were amplified from HbAA and HbSS genomic DNA templates before CRISPR-based SNP-Chip analysis. L, 100-bp ladder. (**c**) Prior to SNP-Chip analysis, HbAA and HbSS DNA amplicons were sequenced to confirm the presence of the target SNP and the gRNA-HTYa and gRNA-SCDa sequences, respectively. The PAM is noted with a black box, and the SCD-associated SNP is noted with a green arrow. (**d**) AFM image of a bare graphene channel (left) and a channel after dCas9 immobilization (right). The yellow box indicates a 5 μm × 5 μm graphene area; yellow circles each indicate an immobilized dCas9 molecule. Scale bar, 2 μm. (**e**) Schematic of SNP-Chip functionalized with the dCa9–gRNA complex. gRNA-HTYa and gRNA-SCDa were used. In the presence of the SCD-associated SNP, dCas9-HTYa does not hybridize completely with its DNA target, and the DNA dissociates from the dCas9–gRNA complex. For these experiments, all DNA samples were tested at a concentration of 30 ng μl^{-1}. (**f**) I response of the dCas9-HTYa construct (left) (one-way analysis of variance (ANOVA): F = 13.02) and dCas9-SCDa construct (right) (F = 41.61) in the presence of HbAA, HbSS or control amplicons. (**g**) C response of the dCas9-HTYa construct (left) (F = 15.44) and dCas9-SCDa construct (right) (F = 11.28) in the presence of HbAA,

HbSS or control amplicons. (**h**) V response of the dCas9-HTYa construct (left) (F = 16.69) and dCas9-SCDa construct (right) (F = 20.91) in the presence of HbAA, HbSS or control amplicons. All box and whisker plots show the minima, Q2, median, Q3 and maxima ($n \geq 10$ technical replicates). Statistical significance was determined by Tukey's multiple comparisons test after one-way ANOVA (*P < 0.05; **P < 0.01; ***P < 0.001; ***P < 0.0001; two tailed), P < 0.05 considered significant.

We have consistently observed a difference in the interaction between the dCas9 complex on the surface of the gFET and DNA with varying degrees of complementarity (HbAA, HbSS or control) across all electrical parameters analysed. More specifically, the presence of a single-nucleotide mismatch at the seed region of the protospacer notably decreased the SNP-Chip interaction with amplicons introduced to the sensor. Encouraged by the single-nucleotide specificity of the dCas9-based SNP-Chip, we further examined the sensors' sensitivity in the presence of unamplified genomic DNA targets. For these studies, we employed gRNA-HTYa as this gRNA design demonstrated good specificity in all electrical parameters and has been previously reported to efficiently edit the *HBB* gene at the SCD-associated SNP locus with minimal off-target interactions [118]. Like the SNP-Chip construct used to collect the data presented in **Fig. 3.2f-h**, a dCas9-HTYa complex was anchored to the surface of the gFET. This SNP-Chip construct was calibrated and then incubated with unamplified HbAA or HbSS genomic DNA (60 ng μl^{-1}) (**Figure 3.3a**). The I response was measured and the C response was calculated in real time. The C response was selected as the most sensitive measurement parameter in the presence of full genomic DNA. The dCas9-HTYa SNP-Chip construct was able to differentiate between HbAA and HbSS genomic DNA in the C response (P < 0.0001). **Fig. 3.3c** shows representative real-time C response data acquisition for the dCas9-HTYa SNP-Chip in the presence of HbAA and HbSS genomic DNA. This curve shows the change in the C response that occurs with incubation of genomic DNA, followed by the response of the sensor to rinsing off the

DNA sample. As a large, charged molecule, DNA creates a large sensing response during incubation regardless of whether the DNA is bound to the CRISPR complex or simply happens to be adjacent to the graphene channel. The real-time data collected indicate that, before removing unbound genomic DNA, a difference between HbAA and HbSS signals can be seen. For example, **Fig. 3.3c** shows that within the first 5 min of DNA incubation atop the gFET, HbAA genomic DNA gave a C response signal that was ~1.5-fold larger than that of the HbSS gDNA containing the SNP.

However, the critical measurement occurs at the end of the rinse step, when DNA that is not specifically bound to the CRISPR complex is removed from the surface of the chip. **Fig. 3.3d** shows the endpoint DNA signal as the C response obtained with the dCas9-HTYa construct after DNA incubation and the final rinse step. The sensor reached equilibrium within 5 min of incubation, suggesting that the assay time can be further reduced (not tested in these studies). These data again show a complementary DNA response greater than 20 % (that is, 23.7 %), representing a significant 1.6-fold increase in C response ($P < 0.0001$) in the presence of target HbAA genomic DNA compared with the SNP-containing HbSS genomic DNA.

Novel Cas9 variants are continuously being developed for improved specificity [129], thermal stability [130] and size [131]. The growing abundance of Cas9 orthologues has the potential to broaden the applications of SNP-Chip technology. We decided to test this technology with different Cas9 enzymes, including the nuclease-active Cas9 from *Streptococcus pyogenes*, which is the most widely used CRISPR enzyme. Digital analysis of the nuclease-active Cas9 activity can serve as a more direct comparison between SNP-Chip measurements and CRISPR–Cas9 gene therapies targeting pathogenic SNPs, such as those correcting the mutant *HBB* gene via homology-directed repair for SCD gene therapy [109,110]. This was feasible because studies have

shown that Cas9 remains bound to DNA post-cleavage [90]. Taking advantage of these findings, we employed an additional SNP-Chip construct, functionalized with a Cas9 (MacroLab, University of California, Berkley)–gRNA-HTYa complex, which is capable of binding to and cleaving the *HBB* target sequence [118].

To interrogate SNP-Chip's capacity to serve as a SNP detection tool when incorporating Cas9 as the CRISPR element, we tested the Cas9-HTYa SNP-Chip construct with both HbAA and HbSS genomic DNA. **Fig. 3.3b** shows the SNP-Chip construct employed in this study. **Fig. 3.3e** shows the endpoint DNA signal as the C response obtained with the Cas9-HTYa construct after DNA incubation and the final rinse step. These data show a complementary DNA response of 10.8%, representing a significant 2.4-fold increase in C response (P = 0.0118) in the presence of target HbAA genomic DNA compared with the SNP-containing HbSS genomic DNA.

To determine the sensitivity of this platform, we designed the study described in **Fig. 3.3f**. The Cas9-HTYa SNP-Chip construct was incubated with varying concentrations of target HbAA genomic DNA (10–60 ng μl^{-1}). The results of this study are shown in **Fig. 3.3g**. A positive linear correlation between DNA concentration and C response was observed, indicating the quantitative nature of this technology. To further assess the sensitivity and specificity of the platform, the Cas9-HTYa SNP-Chip construct was incubated in the presence of non-homogenous DNA samples, all of which had a concentration of 60 ng μl^{-1}. These samples contained different percentages of target HbAA DNA and non-target HbSS DNA. The results of this study are shown in **Fig. A.2a,b**. A weak positive linear correlation between the percentage of target DNA (HbAA %) and C response was observed, indicating specific discrimination against a concentrated background of DNA with single-nucleotide mismatch specificity. Furthermore, the slope of linear regression deviated significantly from zero (P = 0.0072). The lowest concentration of target HbAA DNA tested in this

study was 12 ng μl^{-1}, which, when considering a molecular weight of 1.9 × 1012 g mol^{-1} of the human genome [132], equals 6.3 fM. To confirm SNP-Chip's ability to discriminate between target and non-target DNA at this concentration, an additional experiment was performed in which the Cas9-HTYa construct was incubated with 6.3 fM HbAA genomic DNA and 6.3 fM HbSS genomic DNA (**Figure A.3**). At a concentration of 6.3 fM, SNP-Chip was still capable of discriminating between HbAA and HbSS DNA (P = 0.03).

We obtained multiple genomic samples isolated from three patients with SCD and three healthy individuals (Coriell Institute). Specifications of these samples are described in **Table 3.1**. In addition to the two SCD samples, which are homozygous for the E6V mutation, we also tested a sample that had the E6V mutation on one allele and the single-nucleotide variant at codon 6 of the *HBB* gene (that is, a glutamic acid to lysine amino acid substitution of the *HBB* gene; E6K) on the other allele. This mutation results in the production of mutant haemoglobin C, as well as mutant haemoglobin S (HbS). This sample has the genotype E6V/E6K. Blind testing of these samples with the Cas9-HTYa SNP-Chip construct was performed. Again, SNP-Chip could discriminate between samples from healthy individuals and patient samples that contained a SNP within the Cas9 target site (P = 0.0077) (**Fig. 3.3h**).

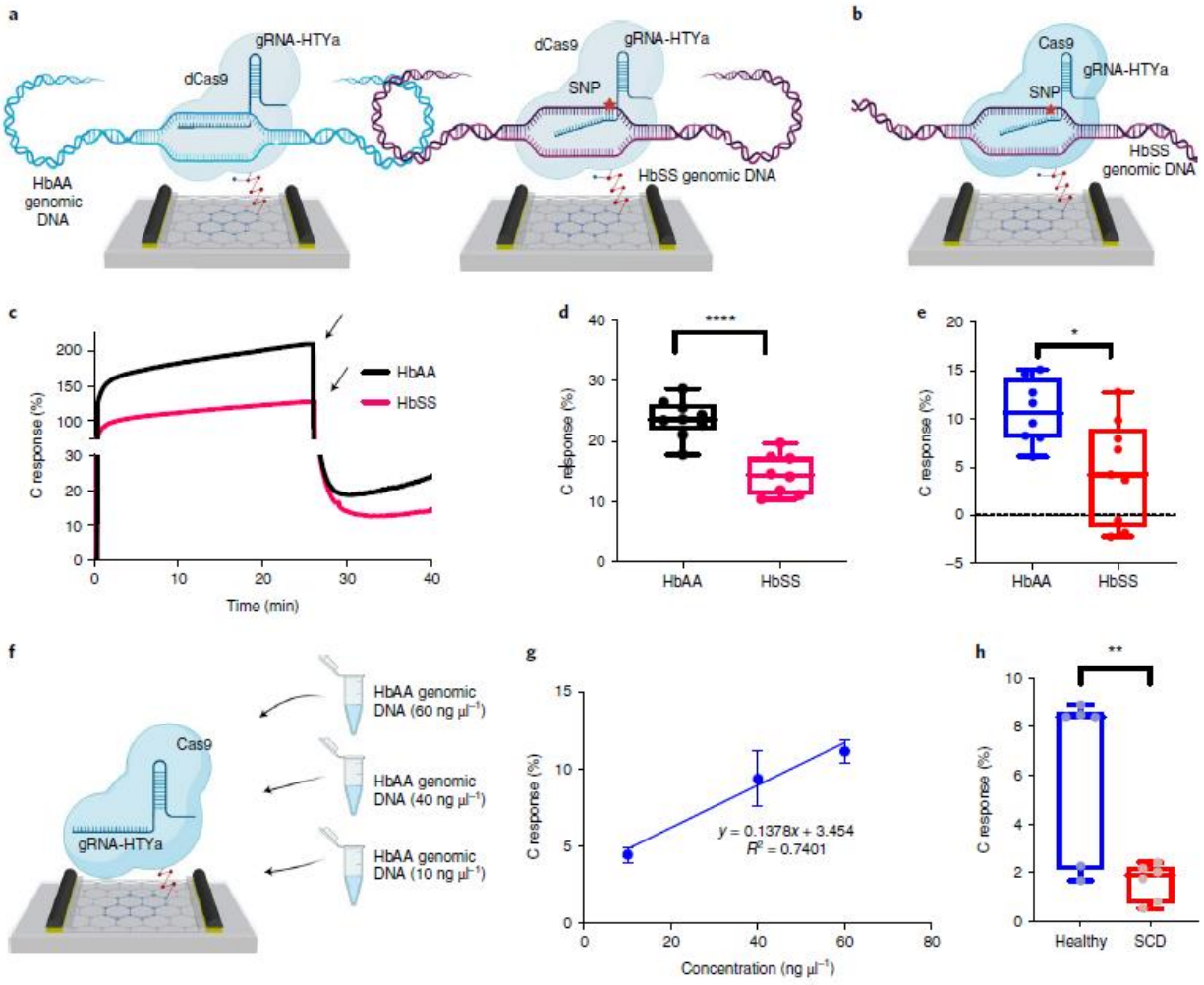

Figure 3.3: (a) Schematic of SNP-Chip functionalized with the dCas9–gRNA complex. gRNA-HTYa was used. In the presence of the SCD-associated SNP, dCas9-HTYa does not hybridize completely with its DNA target, and the DNA dissociates from the dCas9–gRNA complex. (**b**) Schematic of SNP-Chip functionalized with the nuclease-active Cas9–gRNA complex. gRNA-HTYa was used. (**c**) Real-time C response of dCas9-HTYa in the presence of HbAA and HbSS patient genomic samples. The black arrows indicate sensor rinsing. (**d**) Endpoint C response of the dCas9-HTYa construct in the presence of HbAA and HbSS patient genomic DNA samples (60 ng μl^{-1}) (t = 5.849; d.f. = 15; $n \geq 8$ technical replicates). (**e**) Endpoint C response of SNP-Chip with the nuclease-active Cas9-HTYa construct after incubation with homozygous HbAA and HbSS patient genomic DNA samples (60 ng μl^{-1}) (t = 2.867; d.f. = 15; n = 8 technical replicates). (**f**), Schematic of the sensitivity test during which the nuclease-active Cas9-HTYa construct was incubated with varying concentrations of target HbAA DNA samples (10–60 ng μl^{-1}). (**g**) Results of the Cas9-HTYa construct sensitivity test, during which the nuclease-active Cas9-HTYa construct was incubated with varying concentrations of target HbAA DNA samples (10–60 ng μl^{-1}). Each point in the scatter plot shows a mean value ± s.d. ($n \geq 5$ technical replicates). (**h**) Results of blind studies of the C response of SNP-Chip functionalized with nuclease-active Cas9-HTYa in the presence of patient samples with each phenotype (healthy or SCD) (t = 3.325; d.f. = 10; n = 3 biological replicates, with two technical replicates per biological sample). In (**d**), (**e**) and (**h**), significance was determined by unpaired t-test (*P < 0.05; **P < 0.01; ****P < 0.0001; all

two tailed). All box and whisker plots show the minima, Q2, median, Q3 and maxima.

Catalog #	Phenotype	Genotype	Mutation
NA03798	Healthy	HbAA	
NA22807	Healthy	HbAA	
NA23904	Healthy	HbAA	
NA16265	SCD	HbSS	E6V
NA16266	SCD	HbS/HbC	E6V/E6K
NA16267	SCD	HbSS	E6V

Table 3.1: Table summary of clinical samples used in the blind study with the Cas9-HTYa construct. A total of 6 samples (3 from healthy patients and three from patients with SCD) were obtained from Coriell Institute.

To demonstrate the broader usability of SNP-Chip, we employed a second human disease model based on a single-nucleotide mutation in the human *SOD1* gene. This mutation had an A to T substitution resulting in an amino acid substitution of histidine for arginine at codon 44 (H44R) in the SOD1 protein. Specific mutations in the *SOD1* gene, such as H44R, have been linked to the onset of fALS [133]. We designed a gRNA to target the H44R mutation within SOD1. This gRNA, termed gRNA-CS04, was compatible with Cas9 and targeted the H44R SNP at the third nucleotide from the PAM (**Figure 3.4a**) To validate the SNP specificity of gRNA-CS04, we performed an in vitro cleavage assay with target amplicons (CS04 amplicons) originating from hiPSCs, which carried the H44R mutation. As a control, wild-type hiPSCs were also obtained, and the H44R locus was also amplified. These amplicons containing the wild-type sequence are referred to as WTC11.

After 30 min, when complexed with Cas9, gRNA-CS04 showed more efficient cleavage activity with its target amplicon (CS04), as quantified by ImageJ software. Cleavage activity of the target amplicon was 74 %, compared with the activity observed with the wild-type amplicon (WTC11), which was 34 % (**Fig. 3.4b**). We then tested the Cas9-CS04 SNP-Chip construct with CS04, WTC11 and negative control amplicons at a concentration of 30 ng μl^{-1}. In both the I response and the C response, SNP-Chip could discriminate between amplicons, which differed by a single nucleotide ($P \leq 0.0216$) (**Fig. 3.4c,d**).

Finally, to further confirm the ability of SNP-Chip to discriminate between samples that differ by a single nucleotide in the fALS disease model (in addition to the SCD model) without amplification, we extracted genomic DNA from wild-type hiPSCs (termed WTC11) and hiPSCs, which carried the H44R mutation in the *SOD1* gene (termed CS04). Genomic DNA samples (60 ng μl^{-1}) were introduced to the Cas9-CS04 SNP-Chip construct (**Fig. 3.4e**). In the presence of its target DNA, the Cas9-CS04 SNP-Chip construct had an average C response of 23.7 %, which was significantly larger than the C response obtained from the same construct in the presence of the WTC11 genomic DNA sample ($P < 0.0001$). One device was determined to be an outlier by Grubb's outlier test and was removed from further analysis. These results demonstrate that SNP-Chip can be reconfigured to target different SNPs of interest by simply redesigning the gRNA component of the SNP-Chip construct.

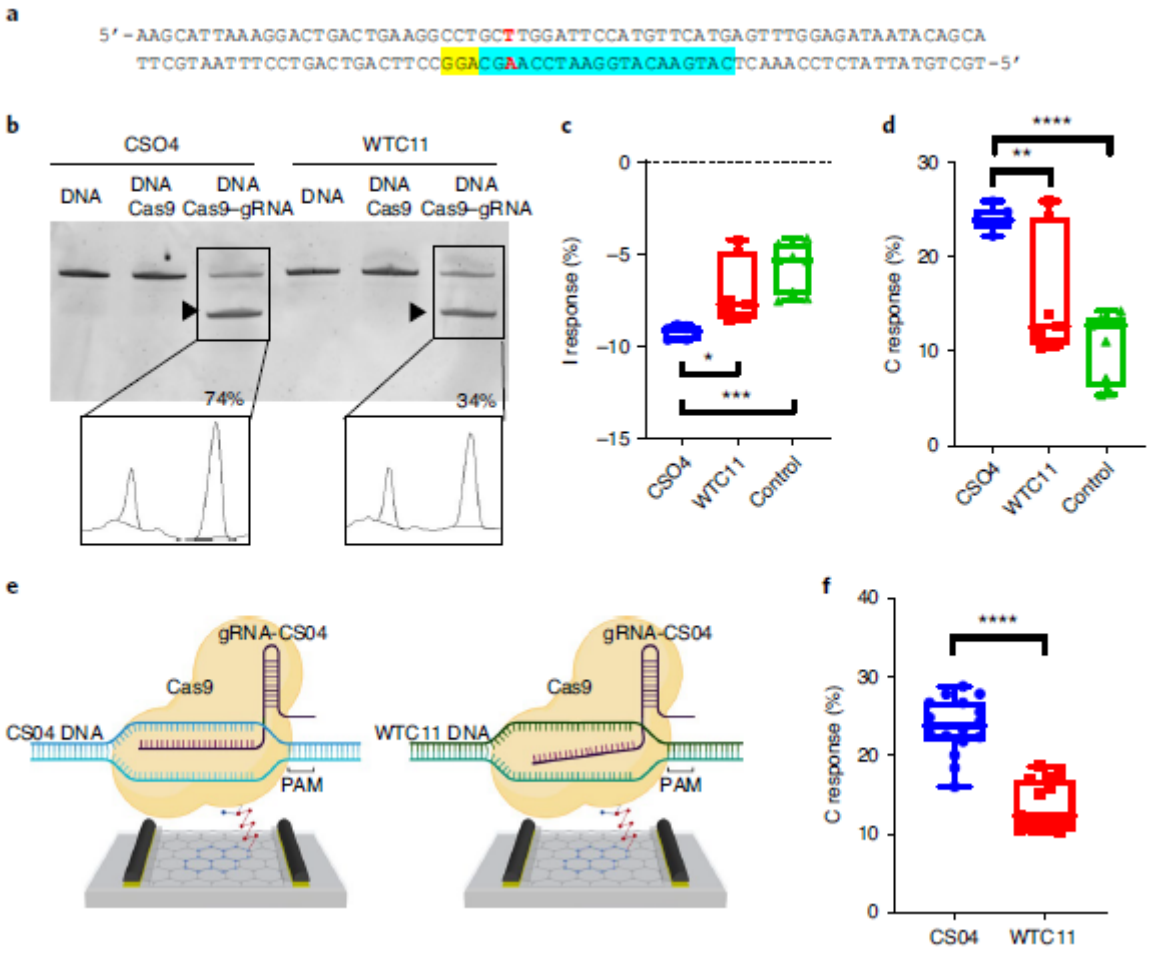

Figure 3.4: (**a**) gRNA-CS04 was designed to target the fALS-associated H44R SNP (red) three nucleotides from the PAM (yellow). The gRNA target is highlighted (blue). (**b**) In vitro cleavage assay with gRNA-CS04 and CS04 and WTC11 amplicons shows more efficient cleavage of CS04 than WTC11. The cleavage products are indicated by black arrowheads. The percentage cleavage was determined with ImageJ. (**c**) I response of the Cas9-CS04 construct in the presence of CS04, WTC11 and negative control amplicons ($n \geq 5$ technical replicates; $F = 13.02$). (**d**) C response of the Cas9-CS04 construct in the presence of CS04, WTC11 and negative control amplicons ($n \geq 5$ technical replicates; $F = 16.7$). Significance in (**c**) and (**d**) was determined by Tukey's multiple comparisons test after one-way ANOVA (*$P < 0.05$; **$P < 0.01$; ***$P < 0.001$; ****$P < 0.0001$), with $P < 0.05$ considered significant. (**e**) Schematic of the Cas9-CS04 construct in the presence of CS04 and WTC11 genomic DNA. (**f**) C response in the presence of CS04 and WTC11 genomic DNA (60 ng μl^{-1}) ($t = 8.131$; d.f. = 29; $n \geq 16$ technical replicates). Significance was determined by two-tailed unpaired t-test (****$P < 0.0001$). All box and whisker plots show the minima, Q2, median, Q3 and maxima.

Although Cas9 is highly programmable [128], single-base-pair sensitivity is limited by the location of that base pair relative to the PAM. The primary PAM for Cas9, 5′-NGG-3′, occurs every 8–12 bp in the human genome on average [134,135]; however, it is possible that for an arbitrary SNP, gRNA designs for Cas9 would not be sufficient for SNP detection. This limitation could be addressed by incorporating CRISPR enzymes that interact with different PAMs [136-138] into the SNP-Chip design or by employing high-fidelity CRISPR enzymes that have enhanced SNP sensitivity [93,94]. We hypothesized that a Cas9 orthologue that targets the SCD-associated SNP within the PAM would further improve SNP-Chip's sensitivity. Namely, since a single-nucleotide mutation in the PAM abolishes binding and cleavage by Cas9 [128,139], SNPs located within the PAM sequence should compromise Cas9 binding and improve SNP-Chip's SNP discrimination capability. We have recently identified a Cas9 orthologue from *Mycoplasma gallisepticum* CA06 strain (MgaCas9; CasZyme) that recognizes 5′-NNGAD-3′ PAM (where D is any nucleotide except C) [140], which overlaps with the SCD-associated SNP (**Figure 3.5a**). This Cas9 orthologue is characterized by a short gRNA, with only two hairpin structures. Also, the analysis of melting temperatures indicated that the thermostability of MgaCas9 is comparable to that of Cas9 [140].

To establish gRNA requirements for MgaCas9, we determined the optimal spacer length with an in vitro DNA cleavage assay. We PCR amplified the *HBB* gene fragment and monitored MgaCas9 cleavage using 21-, 22-, 23- and 24-nucleotide protospacer gRNAs that targeted *HBB* at the same location such that the SCD-associated SNP locus was in the PAM (**Fig. 3.5a,b**). The most efficient cleavage occurred after 30 min with the 22-nucleotide spacer gRNA (**Fig. 3.5c**).

We then tested whether SNP-Chip could serve as a facile amplification-free tool for designing and selecting Cas complexes with higher efficiency, thereby improving on conventional

methods for the selection of different RNA-guided Cas enzymes. To do this, two iterations of SNP-Chip, functionalized with MgaCas9, were employed using two of the validated MgaCas9 gRNA designs. When the two MgaCas9 constructs were incubated with DNA samples, both constructs were able to discriminate between HbAA and HbSS genomic DNA with statistical significance ($P < 0.0001$) (**Fig. 3.5d**). These results obtained from the SNP-Chip MgaCas9 constructs also indicated higher efficiency of the 22-nucleotide gRNA (**Fig. 3.5d,e**), in agreement with the results from the in vitro cleavage assay. This result suggests that this technology can monitor gRNA designs without the need for amplification, which could simplify the gRNA validation process.

In addition, the MgaCas9–22-nucleotide gRNA construct was tested in the presence of non-homogeneous genomic DNA samples that contained different proportions of target (HbAA) and non-target (HbSS) genomic material. Notably, using the MgaCas9–22-nucleotide gRNA compared with the Cas9-HTYa construct improved the linear correlation ($R2$) between HbAA % and the C response (**Fig. A.1c,d**). The slope of this linear regression also deviated significantly from zero ($P < 0.0001$), suggesting that altering the CRISPR component of SNP-Chip can improve its quantitative capabilities.

Finally, we assessed the ability of SNP-Chip to measure the heterozygosity of SNPs without DNA amplification. For this study, we obtained genomic material from a patient heterozygous for HbA and HbS alleles (Coriell Institute). This heterozygous sample (HbA/ HbS) was analysed using both the Cas9-HTYa SNP-Chip construct and the MgaCas9–22-nucleotide gRNA construct. A schematic of the gRNA target sequences and PAM of these two constructs is shown in **Fig. 3.5f**. We have shown that the Cas9-HTYa SNP-Chip construct can discriminate between HbAA and HbSS DNA, but it was unable to discriminate between heterozygous (HbA/HbS) and homozygous (HbSS) samples (**Fig. 3.5g**). However, the MgaCas9–22-nucleotide

gRNA construct, which targeted the SCD-associated SNP within the PAM, discriminated directly (no DNA amplification) between the homozygous (HbSS) and heterozygous (HbA/ HbS) samples with statistical significance (P = 0.000129). This result is important in demonstrating the ability of SNP-Chip to detect heterozygosity, to quantify predisposition to and potential to transmit numerous genetic disorders by taking advantage of the diversity of Cas9 orthologues and the programmability of SNP-Chip.

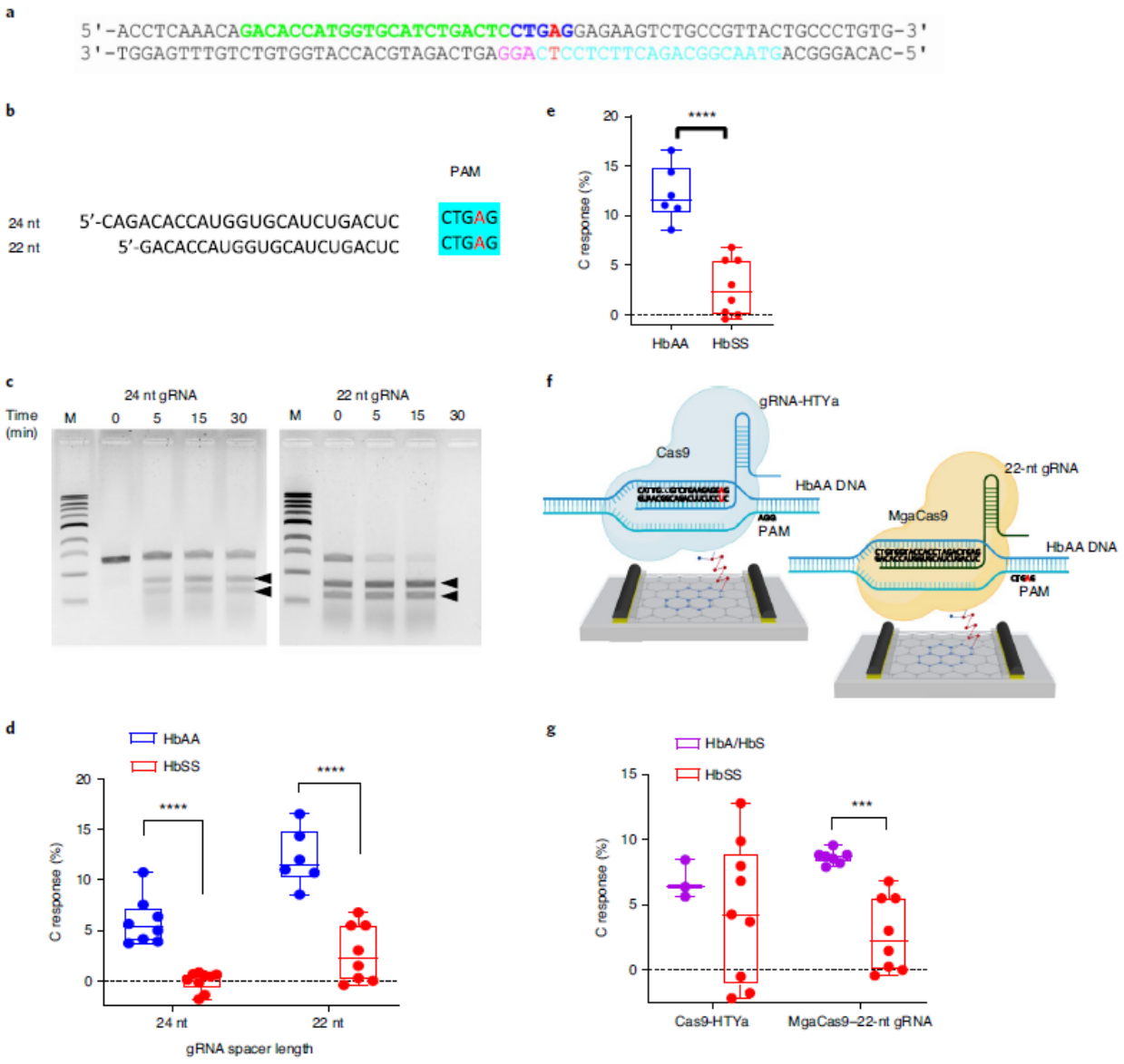

Figure 3.5. (**a**) Schematic of MgaCas9 and Cas9 targets in the *HBB* gene. The SNP is indicated in red, the MgaCas9 target sequence is indicated in green and its PAM is indicated in blue. The Cas9 PAM and protospacer are on the opposite DNA strand and are indicated in pink (PAM) and blue (target sequence). (**b**) Two different MgCas9-compatible gRNAs were designed to target the SCD-associated SNP locus (red) in the PAM (highlighted in blue) with two spacers of different nucleotide (nt) lengths. (**c**) An in vitro cleavage assay was performed on *HBB* amplicons, and successful cleavage was confirmed via gel electrophoresis. The 22-nucleotide gRNA was more efficient than the 24-nucleotide gRNA after a 30-min reaction, as indicated by the double arrowheads. M, 1-kb DNA ladder. (**d**) Two SNP-Chip constructs utilizing MgaCas9 were employed to compare the efficiencies of the 22-nucleotide gRNA and the 24-nucleotide gRNA. The C response of the MgaCas9–22-nucleotide gRNA construct (t = 6.143; d.f. = 12) and the MgaCas9–24-nucleotide gRNA construct (t = 6.897; d.f. = 15) in the presence of homozygous HbAA and HbSS patient genomic DNA samples (60 ng μl^{-1}) was measured ($n \geq 6$ technical replicates). (**e**) C response of the SNP-Chip MgaCas9–22-nucleotide gRNA construct after

incubation with homozygous HbAA and HbSS patient genomic DNA samples (60 ng μl^{-1}) ($n \geq 6$ technical replicates). (**f**) Schematic of the SNP-Chip Cas9-HTYa construct fully complexed with the target HbAA genomic DNA (left) and the SNP-Chip MgaCas9–22-nucleotide gRNA construct fully complexed with the target HbAA genomic DNA (right). (**g**) C response of the SNP-Chip Cas9-HTYa construct ($t = 0.7082$; d.f. = 10) and the MgaCas9–22-nucleotide gRNA construct ($t = 5.362$; d.f. = 13) after incubation with heterozygous HbA/HbS and homozygous HbSS patient genomic DNA samples (60 ng μl^{-1}) ($n \geq 3$ technical replicates). Significance in (**d**), (**e**) and (**g**) was determined by two-tailed unpaired *t*-test (***$P < 0.001$; ****$P < 0.0001$). All box and whisker plots show the minima, Q2, median, Q3 and maxima.

3.4 Discussion

The use of gFET sensors has become a powerful and useful tool for detecting biomolecules in medical, clinical, agricultural and environmental applications as they offer great versatility and high sensitivity [15,141-143]. In our previous study, we combined CRISPR–dCas9 with our graphene transistors to harness the power of CRISPR as a nucleic acid search and targeting engine [14]. In this study, we have further expanded the uses of this technology by incorporating different CRISPR–Cas9 variants and expanding the types of electrical measurements taken to yield a rapid and direct electronic CRISPR-based biosensor for SNP detection (SNP-Chip) without the need for DNA amplification.

Although other SNP detection technologies have been reported [116,145-147], these technologies primarily interact with small DNA fragments [117,146] or the less complex bacterial genome [145]. SNP detection in the more complex human genome requires enrichment [148] or amplification [116]. More detailed comparisons between our technology and other DNA detection technologies are available in **Table A.1** and **Table A.2**.

To evaluate the technology, we first tested SNP-Chip using SCD as a SNP disease model. By using a gRNA to target the healthy *HBB* allele, such that the SNP locus was within the seed region of the gRNA spacer sequence, SNP-Chip constructs with both dCas9 and Cas9 could

discriminate between genomic DNA samples from healthy patients and those with SCD. We have also tested this technology in the presence of non-homogenous DNA samples containing different percentages of target versus non-target DNA, demonstrating the quantitative nature of this technology. One key advantage of using CRISPR–Cas9 and SNP-Chip label-free technology is the ease of re-programmability to detect other target genes. To target a different mutation, one can reconfigure the CRISPR element employed within SNP-Chip by simply designing a new gRNA. We have demonstrated this by utilizing SNP-Chip to detect a different single-nucleotide mutation implicated in human disease (ALS). These findings suggest that facile SNP-sensitive genotyping of multiple genes is possible with CRISPR-powered gFETs.

One key limitation of this technology is the PAM-dependent nature of CRISPR–Cas9 to interact and bind to its DNA target [85], as this interaction is reliably disrupted when mismatches lie in the PAM-proximal region of the gRNA spacer sequence [125]. Therefore, certain single-nucleotide mutations, which are not proximal to a PAM sequence, may be difficult to detect. Although this presents a challenge for broad applications of this technology, the diversity of newly discovered Cas9 orthologues or engineered Cas9 variants, including those that are PAM independent [149], will enable further expansion of our technology's capability to detect a wide variety of gene sequences with SNP-level sensitivity. For example, in this work, we have used a recently reported Cas9 orthologue [140] with different PAM requirements to improve the discriminative capability of our platform. The use of this Cas9 orthologue enabled us to discriminate between genomic DNA from patients homozygous for the sickle cell trait and patients who were heterozygous carriers of the trait. The CRISPR field is constantly expanding, and as new CRISPR–Cas enzymes are discovered or engineered, the potential applications of this technology will broaden, allowing us to develop new tools for rapid and facile nucleic acid detection.

SNP-Chip may contribute to medical diagnostics and basic research, as it can meaningfully reduce the time and cost of SNP genotyping, monitor the efficiency of gRNA designs and facilitate the quality control processes involved in CRISPR-based gene editing.

Chapter 4

Single-Molecule Measurements Using SWCNT-FETs

Ensemble techniques provide limited biosensing information as they fail to observe subtle biomolecular characteristics due to ensemble averaging. Single-molecule techniques allow probing of biomolecules with greater depth than their ensemble counterparts to fill this informational gap. The prevalent techniques in single-molecule science include: optical tweezers, magnetic tweezers, FRET, probe microscopy, molecular dynamics (MD) simulations, nuclear magnetic resonance spectroscopy (NMR), nanopore-based sensing, and transistor-based sensing [4,5,18,19,23]. These techniques have contributed a wealth of information to our current understanding of biomolecules such as molecular structure, conformational dynamics, and reaction pathways.

This chapter details the single-molecule sensing mechanism of SWCNT-FETs (Section 3.1), device fabrication and preparation (Section 3.2), experimental procedure (Section 3.3), sample signals generated by Taq polymerase (Section 3.4), and signal analysis and event characterization (Section 3.5).

4.1 SWCNT-FETs and Signal Transduction

SWCNT-FETs have been actively used as chemical and biological sensors over the past 20 years [20-23,150-152]. Due to their quasi-one-dimensional structure, SWCNTs boast inherently high sensitivity to local environments. For measurements of enzyme kinetics, an individual molecule is immobilized to the SWCNT sidewall and the device is submerged in a liquid containing substrates for catalysis. During catalysis, the motions of charged residues alter

local potentials surrounding the SWCNT channel and electrostatically gate the channel and/or modulate the Schottky barrier at the SWCNT-metal contact [22,153,154]. These motions are transduced as changes in source-drain current, given by the Debye-Hückel expression

$$|\Delta I(t)| = \frac{A}{x_0}\exp\left(-\frac{x_0}{\lambda_D}\right) \tag{4.1}$$

where λ_D is the Debye length, determined by the ionic strength of the liquid, and x_0 is the relevant screening distance for gating [155-158].

4.2 Device Fabrication and Preparation

The methodology for SWCNT synthesis and device fabrication is well established and only briefly summarized here. SWCNTs were grown via chemical vapor deposition (CVD) from $Fe_{30}Mo_{84}$ catalyst seeds on 4-inch doped (p++) silicon wafers with a 250 nm thermally formed insulating oxide layer [159,160]. A fast-heating CVD recipe permitted growth of straight CNTs upwards of 100 μm in length. Immediately following growth, each wafer was baked at 315 °C for 30 minutes to remove excess amorphous carbon. Next, the entire wafer was passivated by atomic layer deposition (ALD) with 10 nm Al_2O_3. Bilayer nickel (40 nm) and platinum (10 nm) electrodes were then lithographically defined using photolithography and deposited using electron-beam evaporation. Lastly, an additional layer of Al_2O_3 was deposited to passivate SWCNT-electrode contacts until the device is ready for measurements.

Following device fabrication, each SWCNT-FET device required characterization and further preparation prior to biochemical measurement. Images of individual devices were acquired using scanning electron microscopy (SEM) (JEOL 6060) to verify single SWCNT connections. Following SEM imaging, the Al_2O_3 passivation layers were removed with a proprietary phosphoric

acid (Transene Transetch-N). To prepare SWCNT-FET devices for measurements in liquid, electrodes were re-passivated with a layer of polymethyl methacrylate (PMMA). Devices were first spincoated with a layer of PMMA photoresist, then 1 μm windows were drawn between source and drain electrodes using electron beam lithography to expose the middle of the SWCNT channel. The windows were developed in 3 to 1 solution of methyl isobutyl ketone (MIBK) to IPA. The undeveloped PMMA was partially cured in air at 194°C for 30 minutes. After window development and partial curing, devices were imaged with AFM to confirm successful SWCNT exposure and minimal residual photoresist in the exposed window.

4.3 Experimental Procedure

4.3.1 Experimental Setup and Initial Characterization

Figure 4.1 is a cartoon of the experimental setup. For temperature control, the chip was kept in physical contact with a thermoelectric Peltier plate, which was controlled with an external DC power supply. Source and drain electrodes were contacted with micromanipulated needles and recorded with a current preamplifier (Keithley 428) and computer-controlled data acquisition board (NI PCIe-6361). Liquid potential control was achieved by contacting the on-chip liquid with two Pt wires (0.2mm diameter, Alfa #00263) to serve as counter and pseudo-reference electrodes. The two Pt wires were connected to a Keithley 2400 SourceMeter in 4-wire mode, which provided continuous monitoring and control of liquid potential, V_{lg}, and counter electrode current, I_{lg}. The stability and calibration of the Pt pseudoreference was checked against a standard Ag/AgCl reference electrode each day before measurements.

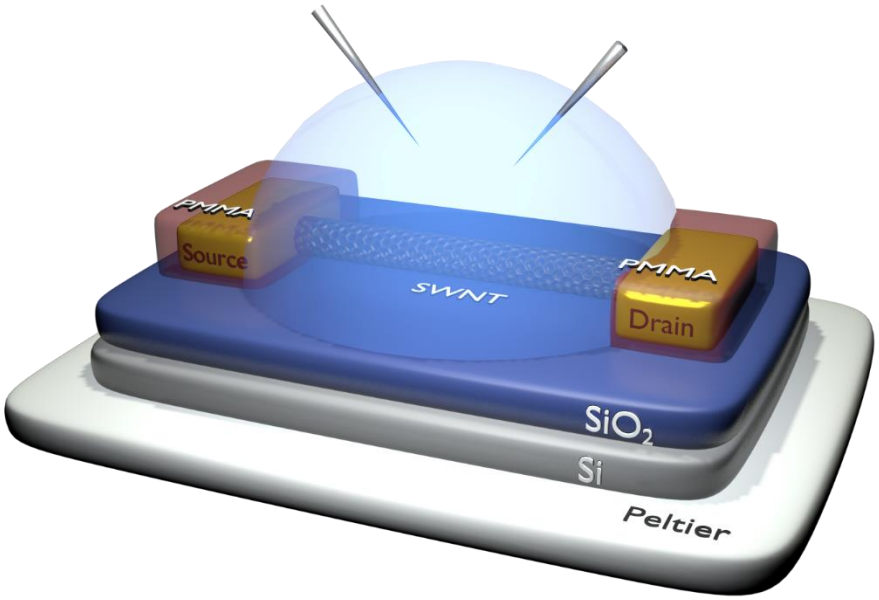

Figure 4.1: Schematic of the SWCNT-FET submerged in liquid, with the source and drain electrodes (gold) passivated by PMMA (burgundy) as the device sits atop a thermoelectric Peltier plate (white).

Before biofunctionalization, each SWCNT-FET device was measured in Taq activity buffer solution (40 mM HEPES + 50 mM KCl + 5 mM $MgCl_2$) to verify its experimental suitability. Measurements of source-drain current, $I_{sd}(t)$, were performed at various V_{lg} spanning from the threshold voltage, V_{th}, to the saturation region of the device to verify changing conductance over the range. Devices with peak-to-peak noise exceeding 20% of the baseline I_{sd} or with visible deviations from 1/f noise characteristics were excluded from further measurement. Additionally, devices with electrochemical leakage current exceeding 3 nA indicated improper electrode passivation and were also excluded from further measurement.

4.3.2 Taq Polymerase Mutagenesis

Our collaborators in the Weiss lab at University of California, Irvine successfully mutated native Taq polymerase molecules with individual cysteine surface residues to make them biocompatible with the SWCNT-FET platform. The single-cysteine mutation served as an anchor site on the enzyme for immobilization, detailed in the following section. The Weiss lab mutated four variants of Taq polymerase, each with the cysteine located in a specific sub domain to possibly probe various conformational motions of the enzyme during catalysis. These four variants are: (i) R411C, with the cysteine located in the palm subdomain, (ii) R695C, with the cysteine located in the finger domain, (iii) A814C, with the cysteine located in the intervening domain, and (iv) E524C, with the cysteine located in the thumb domain. **Figure 4.2** shows the ribbon structure of Taq polymerase with the subdomains labeled and the cysteine mutation sites highlighted in red. The single point-mutated cysteine ensured site-specific biofunctionalization. Each variant also included a G46D point mutation to deactivate exonuclease activity. Following expression and purification of the Taq polymerase variants, solutions were dialyzed to remove reducing agents that interfere with thiol-maleimide chemistry from the storage buffer.

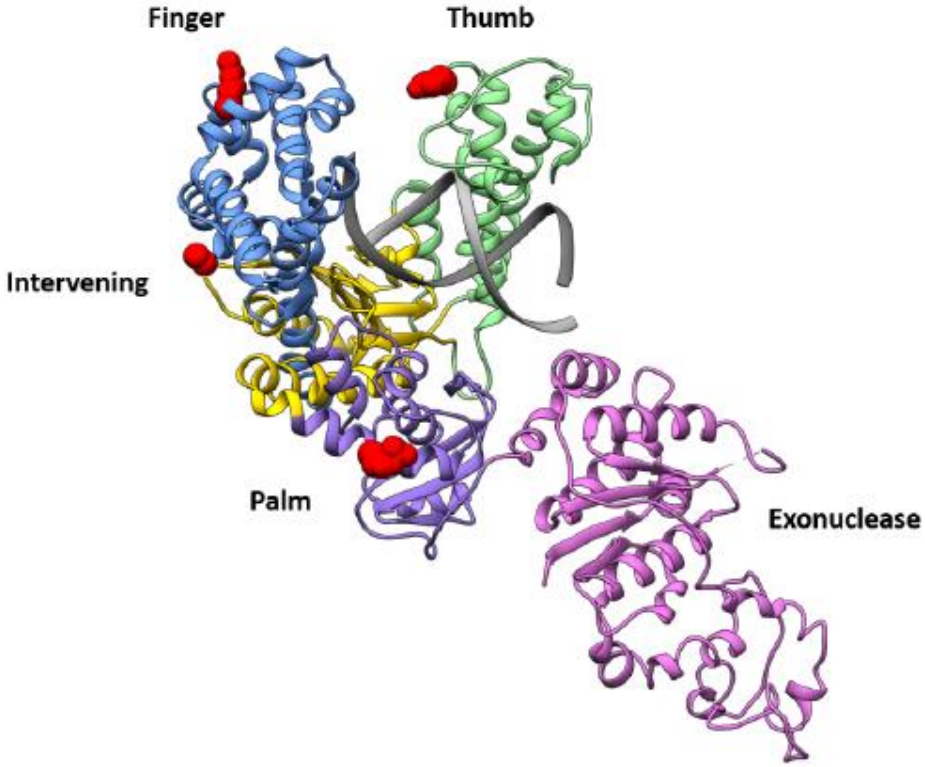

Figure 4.2: Ribbon structure of Taq polymerase in the open conformation as determined by x-ray crystallography. dsDNA is shown in grey, bound at the active site. The five subdomains are annotated, differentiable by color, with the cysteine mutation sites denoted in red.

4.3.3 Biofunctionalization

Biofunctionalization of SWCNT-FET devices occurred in two steps: (i) linker functionalization and (ii) protein immobilization. For linker functionalization, devices were soaked in a solution of 100 pM N-(1-pyrenyl)maleimide (Sigma-Aldrich), hereafter referred to as pyrene-maleimide, and 1 µM pyrene in EtOH, a 1 to 10,000 ratio of pyrene-maleimide to pyrene, for 2 minutes without agitation. While in solution, pyrene and pyrene-maleimide molecules competed to adhere to the exposed SWCNT sidewall via π-π stacking [161]. A 1 to 10,000 ratio of pyrene-

maleimide to pyrene ensured that the majority of the exposed SWCNT surface was passivated with non-reactive pyrene molecules, resulting in only a few chemically available maleimide sites along the ~1 μm length of exposed SWCNT. The 1 to 10,000 ratio in combination with a soak time of 2 minutes reproducibly yielded devices with one to two Taq molecules per μm after immobilization, confirmed by AFM imaging. Soak times longer than 10 minutes resulted in SWCNTs with multiple layers of π-π stacked pyrene molecules, while soak times shorter than 1 minute resulted in devices without any immobilized Taq molecules, presumably due to the lack of maleimide anchor sites. After linker functionalization, devices were rinsed with > 5 mL of EtOH, > 5 mL of IPA, > 5 mL of DI water, then > 5 mL of Taq activity buffer to desorb weakly bound pyrene molecules. Each device was soaked in Taq activity buffer for 10 minutes following the final rinse to allow for equilibriation of the SWCNT and SiO_2 surfaces.

Immediately following the soak in Taq activity buffer, each device was submerged in a solution containing 4 nM Taq polymerase for 5 minutes without agitation to immobilize protein molecules. Free thiol groups of point-mutated cysteine residues on the surface of Taq polymerase molecules reacted with available maleimide groups to form stable thiol-ether bonds [162-164]. The 5-minute soak time was found to be sufficient for Taq polymerase molecules in solution to satisfy all available maleimide anchor sites. Similar to linker functionalization, soak times longer than 10 minutes resulted in excess nonspecifically bound protein while soak times shorter than 2 minutes were insufficient for Taq polymerase molecules to satisfy the linker sites. After protein immobilization, each device was rinsed with at least 10 mL of Taq activity buffer to desorb all non-specifically bound molecules and soaked in Taq activity buffer to allow for surface equilibriation.

4.3.4 Electrical Measurement

After protein conjugation, Taq-biofunctionalized devices were first measured in buffer at various V_{lg}, with data acquired in 100 mV steps, spanning the entire linear region of the device from V_{th} to V_{sat}. During data acquisition, the chip sat atop the Peltier thermoelectric plate for temperature control. All of the data in this chapter was acquired with a constant voltage of 0.2 V or 0.3 V applied to the Peltier device, corresponding to a surface temperature of ~27 °C or ~40 °C, respectively. At least two minutes of $I_{sd}(t)$ were acquired at each V_{lg} to provide sufficient data to gauge background activity for comparison against signals in the presence of substrates.

Following control measurements in buffer, solutions containing single-stranded DNA (ssDNA) and complementary nucleotides (dNTPs) were introduced for Taq to catalyze. For the data shown throughout this chapter, the ssDNA used was a 42-base long strand of thymines ($polyT_{42}$) while complementary nucleotides were adenines (dATP). In the presence of substrates, data was acquired at various V_{lg}, in 50 or 100 mV steps, once again spanning the linear region of the device until catalytic signals were observed, samples of which are provided in the following section.

Following measurements in substrates, the device was removed from atop the Peltier plate and rinsed with >5 mL of buffer + 0.1 % Tween-20 to desorb nonspecifically bound substrates. The device was then measured in buffer again to confirm the absence of catalytic signals. If the catalytic signals observed in the presence of substrates did not subside in the subsequent buffer measurement, then the device was once again rinsed with >5 mL of buffer + 0.1 % Tween-20 then submerged in a well of buffer for at least 30 minutes to allow for slow desorption of nonspecifically bound substrates. This process of rinsing followed by a long bath in buffer was repeated until catalytic signals were no longer observed in measurements using buffer alone.

4.4 Sample Signals

Examples of $I_{sd}(t)$ data from free-running Taq polymerase are shown in **Figure 4.3**. **Fig. 4.3a** shows an example of $I_{sd}(t)$ in buffer, where the noise profile follows 1/f characteristics [165]. **Fig. 4.3b** shows an example of $I_{sd}(t)$ in the presence of substrates. Upon the introduction of $polyT_{42}$ and dATPs, transient excursions began to appear in $I_{sd}(t)$. These excursions, hereafter referred to as events, resulted from conformational changes of Taq polymerase as it polymerizes DNA and are therefore catalytic signals [166].

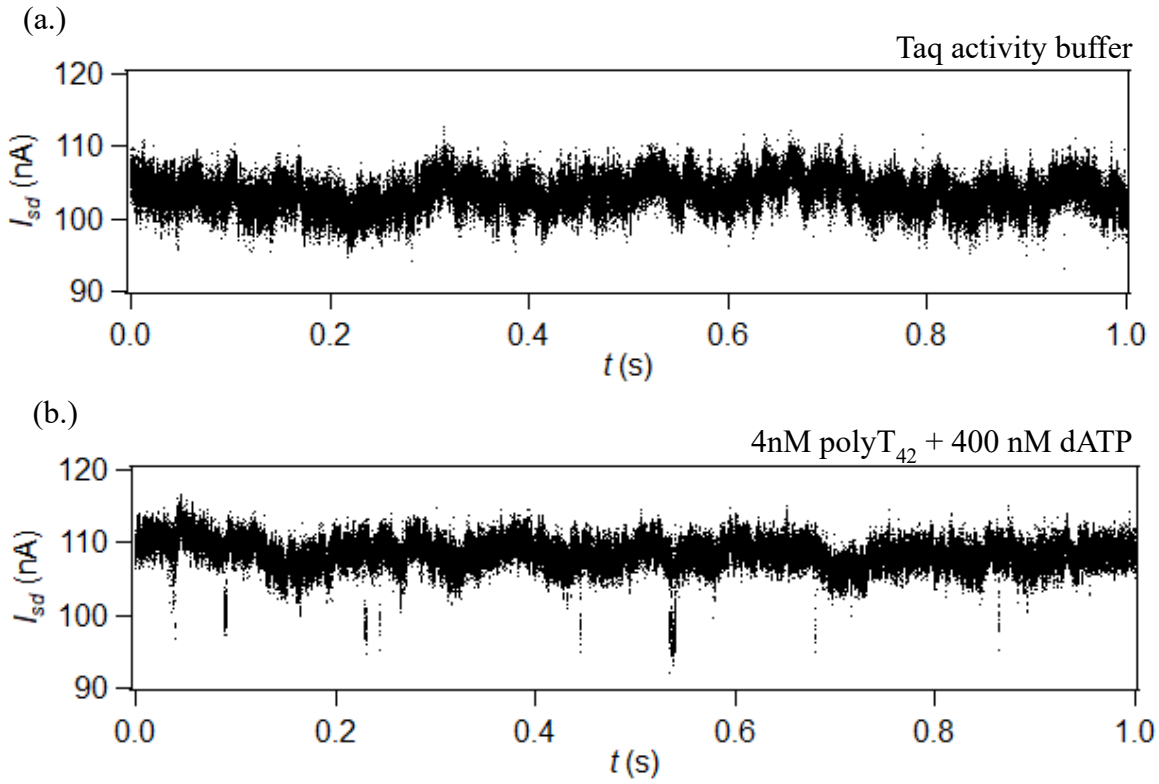

Figure 4.3: Example $I_{sd}(t)$ data of a Taq-functionalized device in (a.) Taq activity buffer and (b.) 4 nM $polyT_{42}$ + 400 nM dATP in Taq activity buffer.

Raw $I_{sd}(t)$ data was denoised and flattened to better characterize events in the analyses described in §4.5 Signal Analysis and Event Characterization. First, $I_{sd}(t)$ data was passed through a NoRSE filter [167]. Next, the data was decimated by a factor of 1000 to 1 with averaging and fit with a third order polynomial. The resulting fit traced low-frequency baseline fluctuations and was subsequently subtracted from the NoRSE-filtered $I_{sd}(t)$ data. The resulting data after fit subtraction, hereafter referred to as denoised I_{sd}, led to more accurate identification and characterization of events. Traces of raw, NoRSE-filtered and denoised I_{sd} data are shown in **Figure 4.4**.

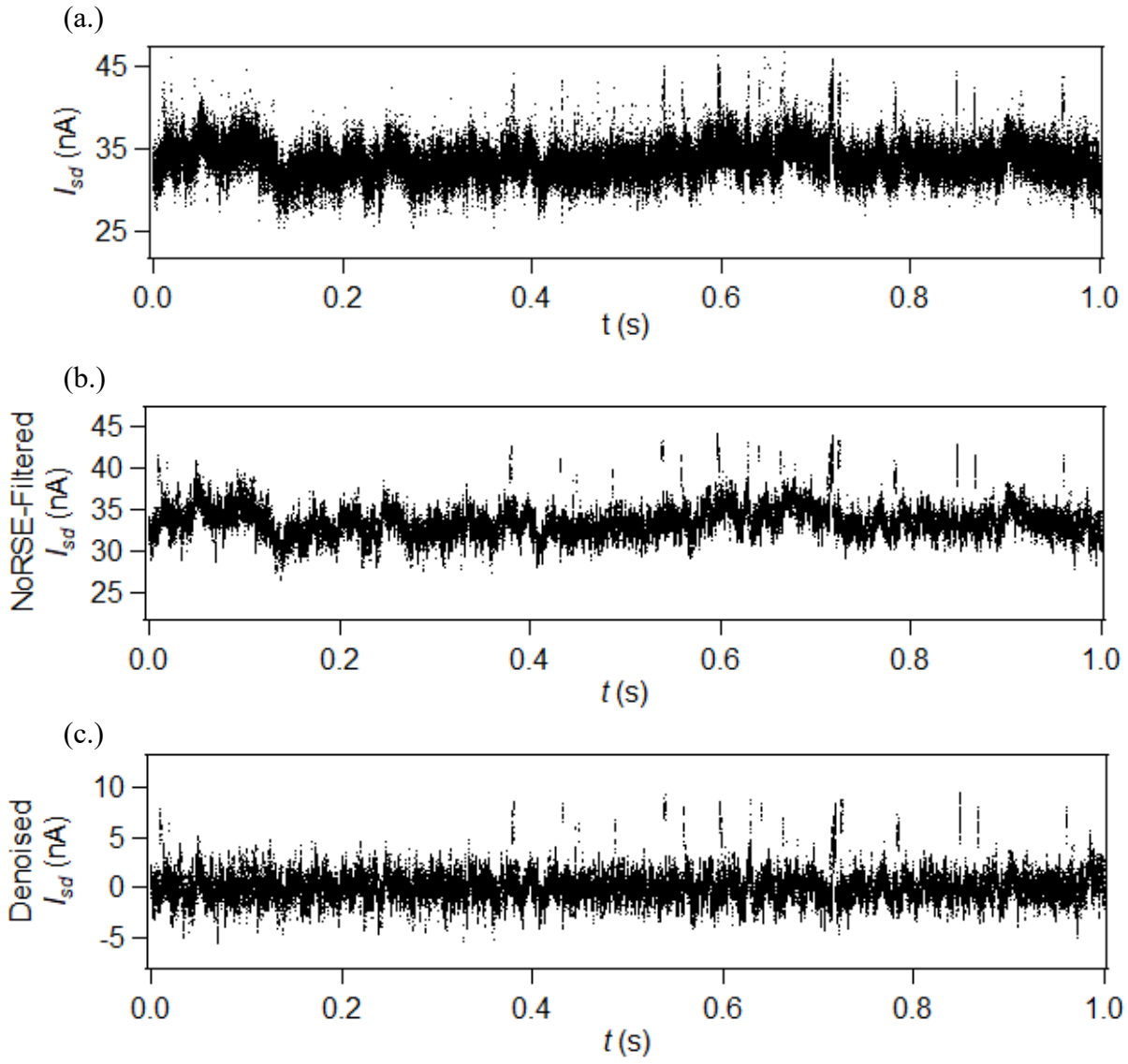

Figure 4.4: (a.) Raw, (b.) NoRSE-filtered, and (c.) denoised $I_{sd}(t)$ data. Events appear most clearly in denoised $I_{sd}(t)$ data due to reduced background noise via signal processing.

4.5 Signal Analysis and Event Characterization

In each data set which they were present, events were characterized by one or more of the following: (i) average event amplitude, (ii) event dwell times, (iii) event waiting times, (iv) event rate, (v) event occurrence probability, and (vi) distribution of events in time. Average event

amplitude was expressed both as change in current, ΔI_{sd}, as well as effective gating, ΔV_{lg}. **Figure 4.5** exemplifies how average event amplitude was measured. A histogram of the denoised I_{sd} data was compiled for 10 s of data for each data set, shown in **Fig. 4.5a**. Each histogram was fit with a double Gaussian function, where the primary peak corresponded to the state of dominant occupation, the open conformation of Taq, and the secondary peak, if any, resulted from the transient excursions from the baseline state, which corresponded to the closed conformation [168,169]. ΔI_{sd} was measured as the difference between peak positions of the double Gaussian fit. If $I_{sd}(t)$ did not contain events, then the corresponding histogram was accurately fit by a single Gaussian function and ΔI_{sd} was assigned a value of zero, indicating the absence of events. A ΔI_{sd} value of 5 nA ± 3 nA was extracted from the example data presented below. To express average event amplitude as effective gating, denoised I_{sd} values were divided by the local transconductance, dI_{sd}/dV_{lg}, of the device under investigation to yield effective liquid gate voltage. The same histogram and double Gaussian fitting procedure was performed for effective liquid gate voltage to determine ΔV_{lg}, as shown in **Fig. 4.5b**. A ΔV_{lg} value of -16 mV ± 8 mV was extracted from the example data presented below. When catalytic signals were observed in multiple datasets acquired at different V_{lg}, the corresponding effective V_{lg} histograms were normalized by FWHM of the primary Gaussian peak before fitting the secondary peak to better compare average event amplitudes at different V_{lg}. This normalization routine and its implementation are explained in more detail in §5.2.1 Event Analysis and Defining a Range of Active V_{lg}.

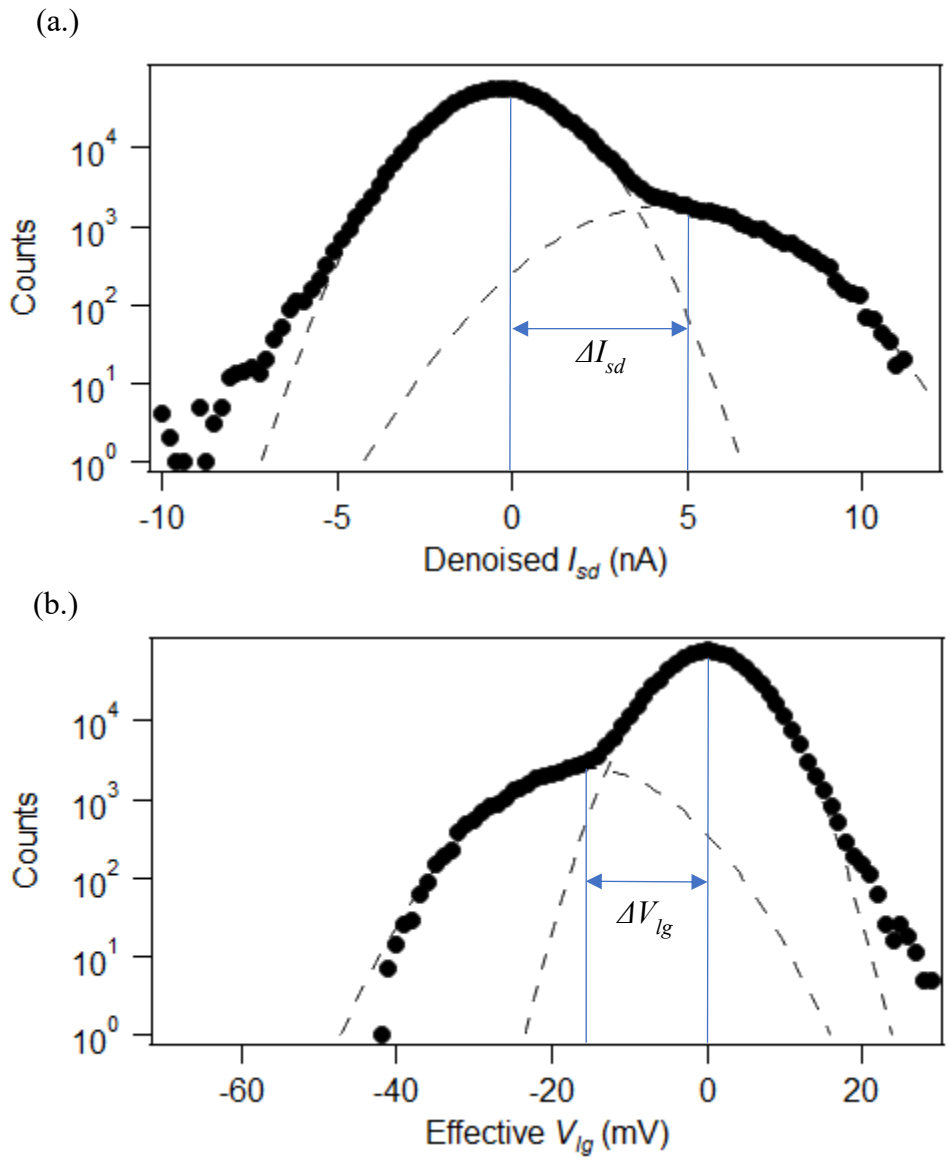

Figure 4.5: (a.) Example histogram of denoised I_{sd} data with the double Gaussian fit overlaid and average event amplitude shown as change in current, ΔI_{sd}, shown. (b.) Example histogram of effective V_{lg} data with double Gaussian fit overlaid and average event amplitude as effective gating, ΔV_{lg}, shown.

To examine event dwell and waiting times, events first needed to be individually characterized. Event recognition was automated using a two-level analysis with user-defined amplitude and event length thresholds. The amplitude threshold was chosen to be the denoised I_{sd} value at the intersection of the two Gaussian peaks from the average event amplitude analysis described above. However, data belonging to the primary peak still satisfied the amplitude threshold when defined this way. To avoid falsely identifying the data corresponding to the primary peak as events, the amplitude threshold was used in conjunction with an event length threshold, where the denoised $I_{sd}(t)$ data was required to continuously satisfy the amplitude threshold for the duration of the event length threshold to be considered an event. The event length threshold was chosen to be 10 data points, corresponding to 100 μs, because anomalous excursions lasting less than 100 μs due to extraneous noise were often observed in the presence of buffer alone and could not be reliably attributed to catalytic motions. The two-level analysis created a binary output wave, synchronized with the input denoised $I_{sd}(t)$ data, assigning each data point to one of the two states depending on whether it satisfied the amplitude threshold. If a sequence of data points failed to continuously satisfy the amplitude threshold for the event length threshold, then the entire sequence of data points was reassigned to the baseline state. Examples of denoised $I_{sd}(t)$ data and the binary output wave are shown in **Figure 4.6**.

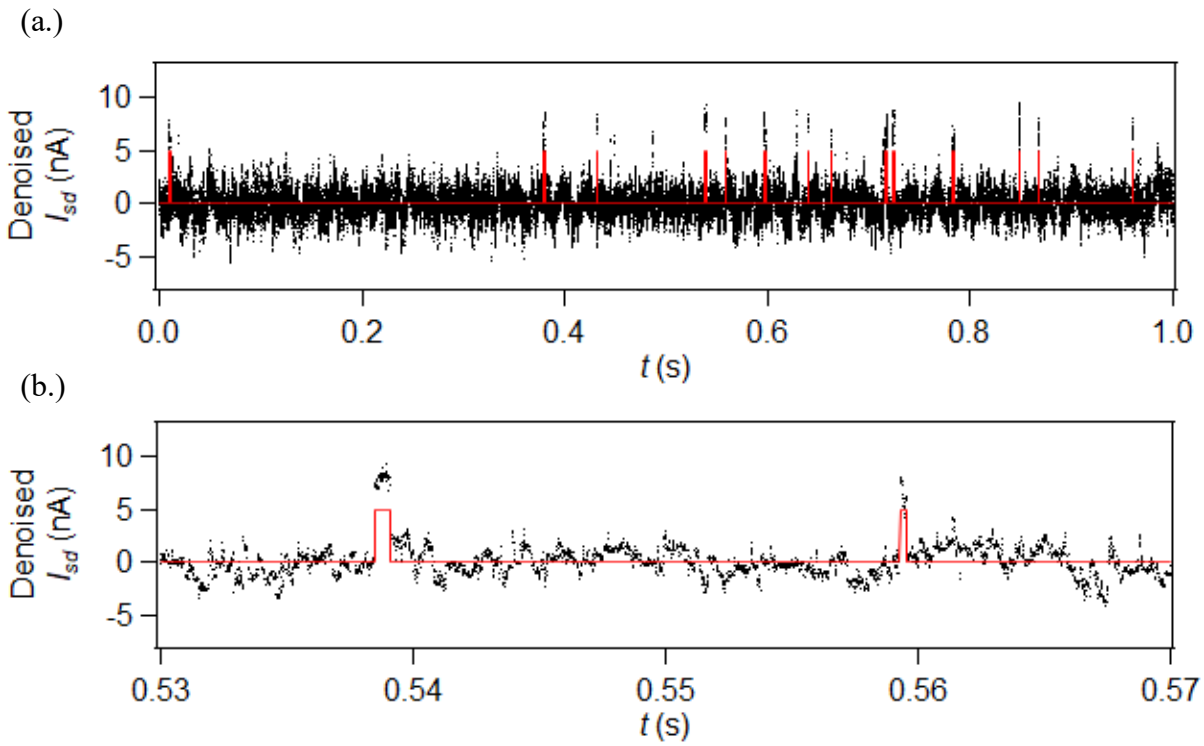

Figure 4.6: Samples of denoised $I_{sd}(t)$ data (black) with the binary output wave (red) of the two-level analysis overlaid.

Both event dwell and waiting times were easily evaluated from the two-level analysis. Event dwell times were calculated as the amount of time an event continuously satisfied the amplitude threshold. Event waiting times were calculated as the time between the end of an event and the beginning of the following event. Histograms of event dwell and waiting times were compiled for entire datasets, with examples shown in **Figure 4.7**. Distributions of event dwell and waiting times were described accurately by either stretched single or double exponential fits, indicating that they followed Poisson statistics, which in turn indicated that Taq's catalysis was a Poisson process. A Poisson process with average time τ has an exponential probability distribution described by

$$P(t) = \frac{1}{\tau} e^{-\frac{t}{\tau}}. \quad (4.2)$$

Stretched exponential distributions resulted from dynamic disorder over multiple minutes of measurement. Average waiting ($\tau_{waiting}$) and dwell (τ_{dwell}) times were extracted from exponential fits of their respective histograms. For the example data presented in **Fig. 4.7**, τ_{dwell} and $\tau_{waiting}$ were found to be 240 µs ± 10 µs and 97 ms ± 5 ms, respectively. The value for $\tau_{waiting,1}$ shown in **Fig. 4.7b** resulted from fitting of the first data point, which contained an anomalously large number of counts and was an artifact of the automated event recognition. More specifically, the automated event recognition mischaracterized individual events as multiple events if the event intermittently failed to satisfy the amplitude threshold, which led to artifactual waiting times. The inverse of $\tau_{waiting}$ gave an average event rate, approximately 10 s^{-1} in this case, which was later compared with average event rates calculated by enumerating the number of events in each second of data.

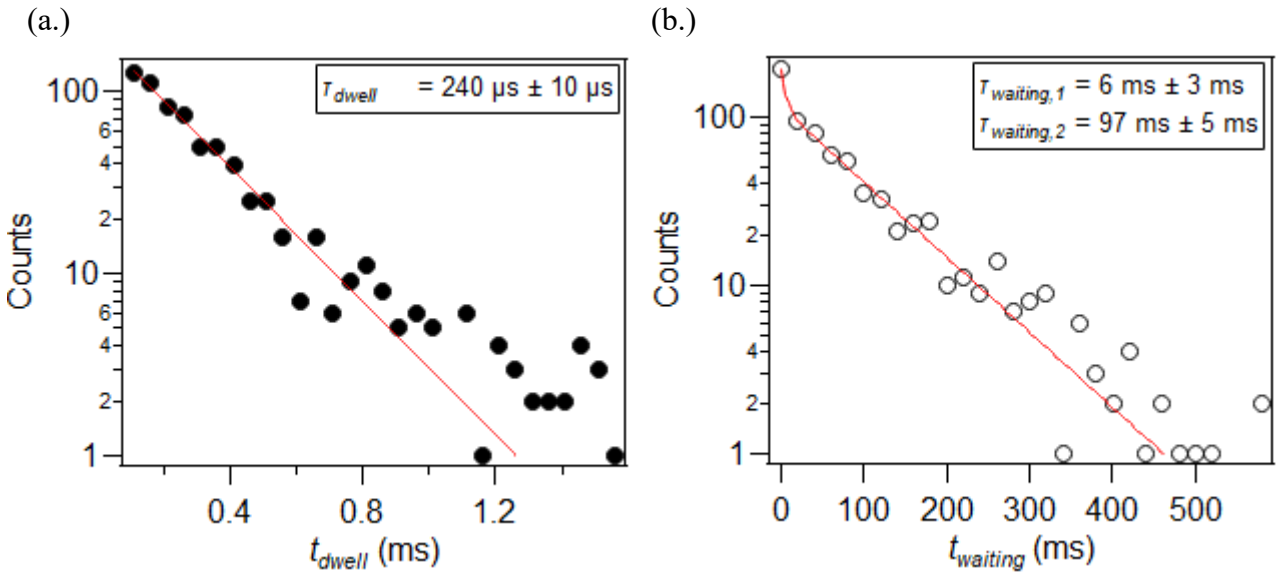

Figure 4.7: (a.) Histogram of event dwell times on a semilog plot with a single exponential fit overlaid and fit parameters shown in the inset. (b.) Histogram of event waiting times on a semilog plot with a double exponential fit overlaid and fit parameters shown in the inset.

To examine the event rate over time, events were enumerated in each second of data by counting the number of leading edges (transitions from the baseline state to the non-baseline state) in the binary wave output of the two-level analysis. Average event rate was calculated by averaging the number of events per second over the entire dataset. An example plot of event rate over time is shown in **Figure 4.8**, with an average event rate per second of 10 s^{-1}. While the average event rate from this analysis was in agreement with the average event rate from the inverse of $\tau_{waiting}$ shown in **Fig. 4.7b**, it is not uncommon for the number of events per second to vary by an order of magnitude from one second to the next [170].

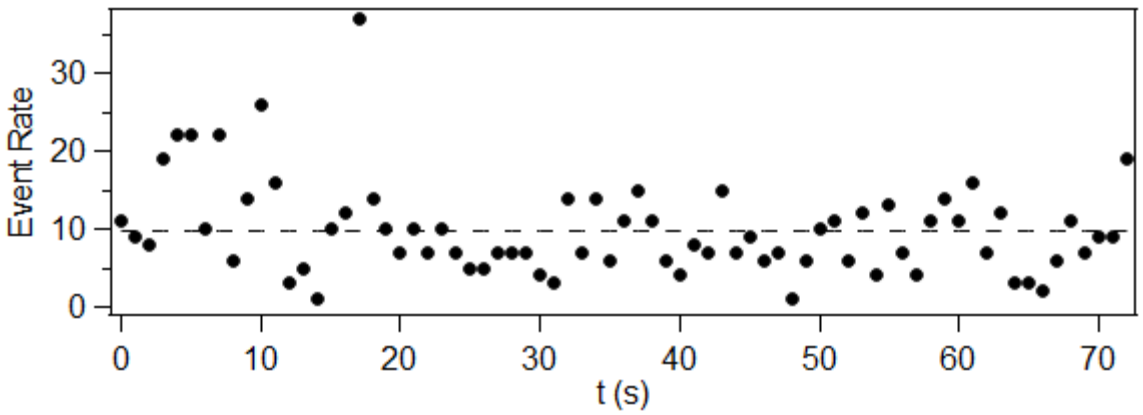

Figure 4.8: Event rate over 73 seconds of data, measured as the number of events detected via the two-level analysis in each second of data. The average event rate of 10 s^{-1}, shown as the dashed line, is calculated by averaging the number of events per second over the entire dataset.

To evaluate the event occurrence probability, the data was examined in sequential 50 ms segments and the number of events occurring in each time frame was recorded. Similar to the event enumeration to examine event rate over time, each 50 ms segment of data was assigned a value equal to the number of events it contained. The probabilities for 0, 1, or 2 events to occur within a

50 ms segment were calculated for entire datasets. **Figure 4.9** shows examples of 50 ms segments containing 0, 1, and 2 events, respectively. An example histogram of event occurrence probability per 50 ms time frame is shown in **Figure 4.10**. The data points represent the values from experimental data while the dashed line is the theoretical prediction for a Poisson process with an average rate of 4 s^{-1}, which was determined to be the corresponding average event rate of the sample data set. The theoretical prediction agreed with the experimental data, providing further evidence that the observed catalytic signal represented a Poisson process.

(a.)

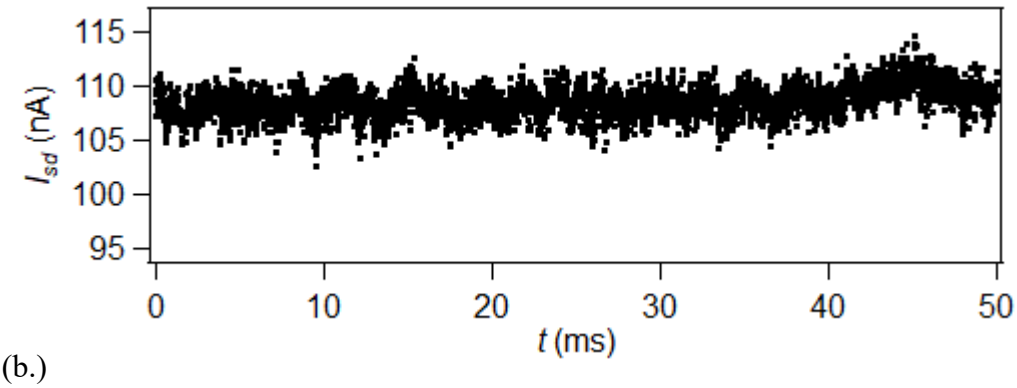

(b.)

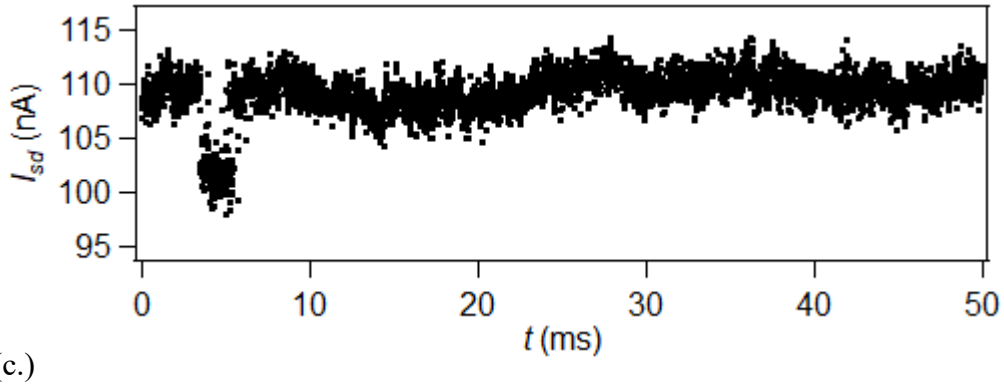

(c.)

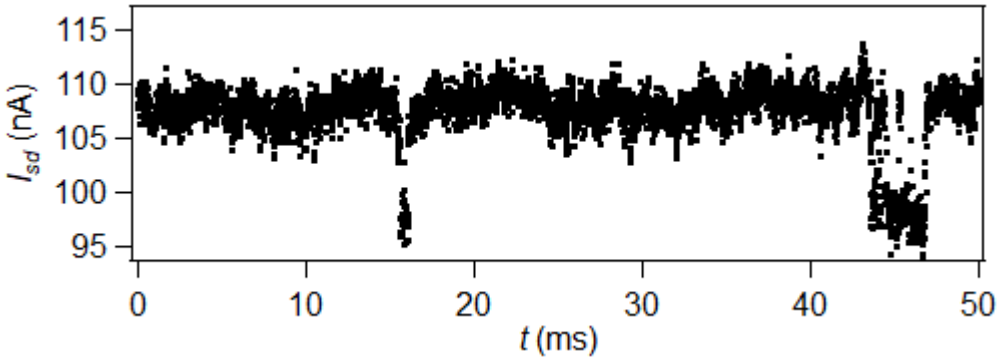

Figure 4.9: 50 ms segments of $I_{sd}(t)$ data containing (a.) 0, (b.) 1, and (c.) 2 events.

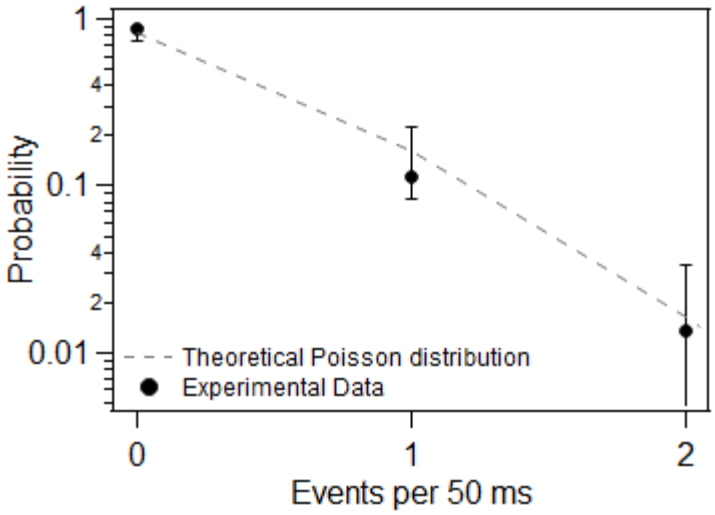

Figure 4.10: Probability to find 0, 1, or 2 events within a random 50 ms time frame.

Lastly, $I_{sd}(t)$ data was examined in 100 ms segments to explore the distribution of events in time. This analysis was performed as an additional method to verify that Taq's catalysis was a Poisson process. To begin, entire datasets were divided up into sequential 100 ms segments of data. Next, the delay time, t_{delay}, was evaluated for each event to be the amount of time between the center of the 100 ms segment of data and the leading edge of the event, as depicted in **Figure 4.11**. If an event did not occur within a 100 ms time frame, no data point was generated. By definition, a Poisson process has an even distribution of events in time when the timing of those events is evaluated with respect to an arbitrary reference point, as is done here.

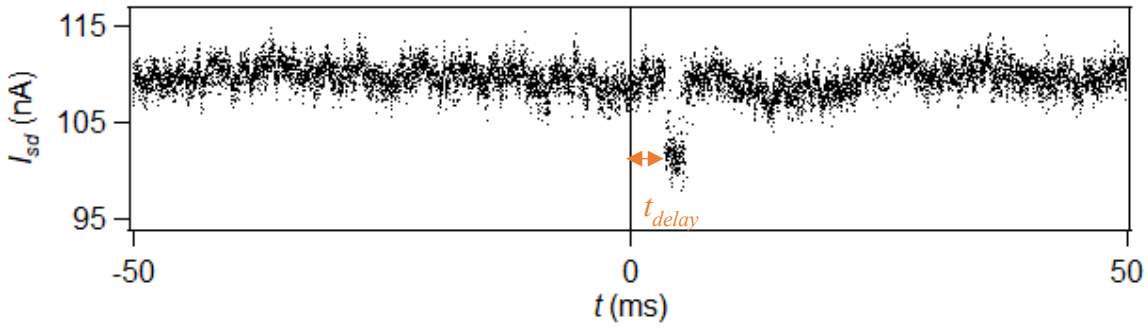

Figure 4.11: 100 ms snippet of $I_{sd}(t)$ data with an event and t_{delay} depicted, defined as the time between the center of the time frame and the time at the leading edge of an event.

The analysis methods presented in this chapter provide various information about the signals observed and therefore the catalytic activity of Taq polymerase. Average event amplitude is related to the charges of nearby residues and their displacements during catalytic conformational changes. On the other hand, analysis of event dwell and waiting times as well as event rates per second provided information regarding Taq's kinetics. Furthermore, the analyses regarding event occurrence probabilities and distributions of events in time provided even more detailed information of Taq's kinetics, confirming that its catalysis is a Poisson process. Each of these analyses were implemented in the work of Chapter 5 to characterize the effects of various applied potentials on individual Taq polymerase molecules.

Chapter 5

Perturbing Taq's Catalytic Timing with Applied Potentials

The work presented in Chapter 2 provided evidence that measurements using solid-state transistor biosensors require careful consideration of applied potentials (see **Fig. 2.8** and **Fig. 2.10**). Beyond simple ligand-receptor binding, there is evidence that electrostatics play an influential role in enzyme catalysis as well [28,29,169,172-174]. Enzyme catalysis has two largely debated theories – dynamical and electrostatic. The dynamical theory of enzyme catalysis proposes that an enzyme samples an ensemble of substates with a preference for conformations along the reaction trajectory [172-174]. Alternatively, the electrostatic theory of enzyme catalysis suggests that preorganized active sites of enzymes promote reactions by reducing barriers via electrostatics such as protein charges, permanent dipoles, induced dipoles and solvation by bound water molecules [27-35]. In either case, external electric fields have been shown to enhance catalytic rates, most often by field-induced stabilization of transition states [34,36-39]. Therefore, the effects of applied potentials in single-molecule measurements of Taq polymerase need proper characterization.

The SWCNT-FET platform also allows measurements using alternating liquid potentials, where enzyme catalysis may be otherwise influenced, via stochastic resonance for example. Stochastic resonance is the phenomenon in which a signal or process of a nonlinear system is enhanced by the presence of an oscillating input signal and stochastic influence, such as thermal fluctuations. The degree to which the nonlinear system is altered depends on both the magnitude of the stochastic influence as well as the magnitude and frequency of the oscillating input signal [175-178]. Stochastic resonance has been observed in biomolecular systems such as DNA hybridization using optical tweezers [179-181]. Regarding the dynamical theory of enzymes, the

sampling of conformational states may be assisted by the presence of a time-varying electric field, influencing conformational change along the reaction trajectory. Stochastic resonance has been observed to affect magnitude of output signals as well as the timing of barrier crossings, both of which may serve as factors for base-pair discrimination in DNA polymerase measurements [175-177]. Aside from stochastic resonance, there has also been work otherwise proposing effects of time-varying electric fields in biomolecular interactions [30,182]. Realization of electrostatic enzymatic control, especially over a DNA polymerase as important as Taq polymerase, could open the door to countless powerful applications.

In this chapter, to explore and understand the effects of applied potentials on individual Taq polymerase molecules, measurements were performed using various time-independent potentials (TIPs) and time-varying potentials (TVPs). Detailed analysis of measurements with TIPs revealed the dependence of Taq's catalytic activity on constant applied potentials. Furthermore, measurements using TVPs explored whether oscillating applied potentials induced corresponding oscillatory behavior of the Taq polymerase molecule.

5.1 Experimental Procedure

Following control measurements in buffer, as detailed in Chapter 4, solutions containing $polyT_{42}$ and dATPs were introduced for Taq to catalyze. In the presence of substrates, measurements were performed with TIPs spanning the linear region of the device. Two or more minutes of $I_{sd}(t)$ were acquired at each V_{lg}, taken in 30 mV steps, to precisely examine whether catalytic signals differed between TIPs. The signals at each V_{lg} were characterized by average event amplitude, average event rate per second, event occurrence probability, and distribution of events in time.

Once signals using TIPs were sufficiently characterized, TVPs were implemented to control V_{lg}. 10 Hz square waves were applied to the counter electrode with amplitudes chosen based on the results of measurements with TIP, explained in more detail in §5.3 Taq Polymerase Activity Under Time-Varying Potentials. Comparisons of event occurrence probability and distributions of events in time were made between TIP and TVP data sets to characterize the effects of time-varying electric fields on the catalytic activity of Taq polymerase. Initial measurements performed on device PCB17-CK00de used only TIPs, while follow-up measurements performed on device PCB45-IG11de used both TIPs and TVPs.

5.2 Taq Polymerase Activity Under a Range of Time-Independent Potentials

The first TIP measurements were performed on device PCB17-CK00de biofunctionalized with R411C Taq polymerase with V_{lg} ranging from -0.35 V to +0.2 V, acquired in 30 mV steps to precisely observe the effects of TIPs. All measurements were performed at T ≈ 27 ºC ($V_{peltier}$ = 0.2 V). $I_{sd}(t)$ for various measurements are shown in **Figure 5.1**. **Fig. 5.1a** shows a characteristic trace of $I_{sd}(t)$ in buffer with V_{lg} held constant at 0.1 V. In buffer, $I_{sd}(t)$ was dominated by 1/f noise. This noise behavior was consistent at all V_{lg} while the device was submerged in buffer alone. **Fig. 5.1b** shows a characteristic trace of $I_{sd}(t)$ in the presence of 4 nM $polyT_{42}$ and 400 nM dATP with V_{lg} held constant at 0.05 V, where positive events began to appear. Events were only apparent in the range of V_{lg} from -0.1 V to 0.14 V, existing throughout the entire measurements performed at each V_{lg}. All V_{lg} with observed events in $I_{sd}(t)$ are hereafter referred to as active $V_{lg.}$ Outside of the range of active V_{lg}, $I_{sd}(t)$ in the presence of substrates was similar to $I_{sd}(t)$ in buffer – dominated by 1/f noise with no events. **Fig. 5.1c** is a characteristic trace of $I_{sd}(t)$ in the presence of substrates with

V_{lg} held constant at -0.16 V, showing the absence of events. This result confirmed that Taq polymerase activity depended on applied potentials.

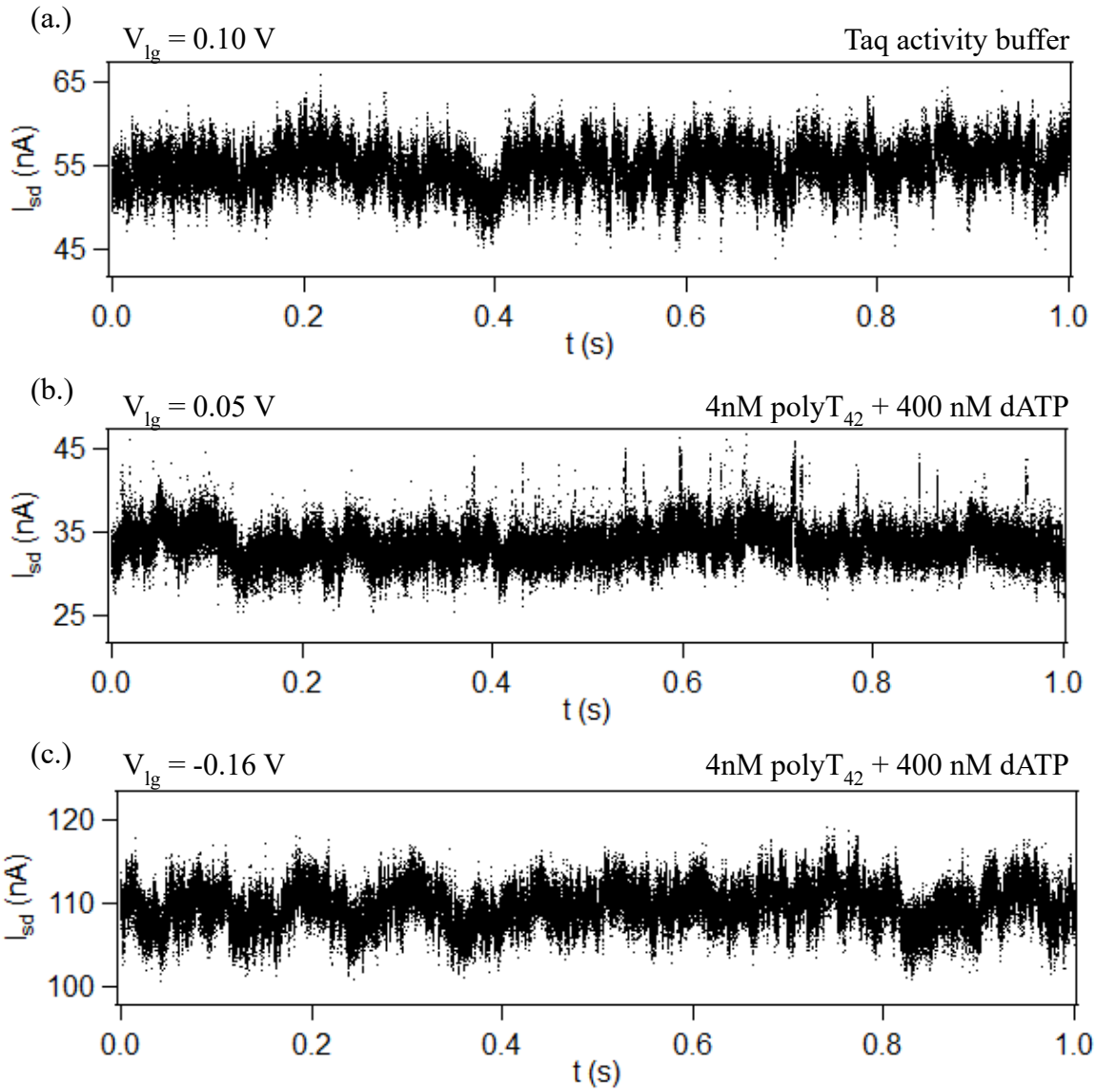

Figure 5.1: One-second snippets of $I_{sd}(t)$ in (a.) Taq activity buffer at V_{lg} = 0.10 V, (b.) 4 nM polyT$_{42}$ + 400 nM dATP in Taq activity buffer at V_{lg} = 0.05 V, and (c.) 4 nM polyT$_{42}$ + 400 nM dATP in Taq activity buffer at V_{lg} = -0.16 V.

Although events were observed in $I_{sd}(t)$ at V_{lg} ranging from -0.1 V to +0.14 V, the event characteristics were not necessarily the same at all active V_{lg}. Therefore, further analysis was required for each measurement to compare events occurring at different V_{lg} and more precisely describe the effects of constant applied potentials.

5.2.1 Event Analysis and Defining a Range of Active V_{lg}

The first metric of comparison between events at different V_{lg} was average event amplitude in effective gating, ΔV_{lg}. **Figure 5.2a** shows histograms of denoised I_{sd} for 10 seconds of data acquired at V_{lg} = -0.22 V, 0.02 V, and 0.11 V. Unfortunately, the magnitude of 1/f noise fluctuations correlate directly with device conductance, which depends on V_{lg}. Therefore, the noise profile of denoised I_{sd} data was different at each V_{lg}, indicated by the varying primary peak width of the denoised I_{sd} histogram. Additionally, the local transconductance dI_{sd}/dV_{lg} was not consistent between V_{lg}, which inherently led to different ΔI_{sd} at different V_{lg}. In other words, if the Taq molecule was locally gating the SWCNT-FET equally, independent of V_{lg}, then variations in local transconductance led to varying ΔI_{sd} across V_{lg}.

To better compare data acquired at different V_{lg}, two signal processing steps were performed on the data before event amplitude analysis. First, the denoised I_{sd} data was converted to effective V_{lg}, as detailed in §4.5 Signal Analysis and Event Characterization, to account for differences in local transconductance between V_{lg}. Resulting histograms of effective V_{lg} are shown in **Fig. 5.2b** for the same datasets as **Fig. 5.2a**. Second, the histograms of data at each V_{lg} were artificially scaled such that the primary Gaussian peak FWHM for all datasets is normalized to a single value to account for differences in 1/f noise and extraneous noise between V_{lg}. For all measurements performed on PCB17-CK00de, the primary peak FWHM at each V_{lg} was

normalized to be 7 mV ± 1 mV, which was the primary peak FWHM at V_{lg} = 0.08 V–the median value between all datasets. The normalized histograms of effective V_{lg} are shown in **Fig. 5.2c** for the datasets shown previously in the same figure. These normalized histograms allowed for more accurate comparisons of ΔV_{lg} at different V_{lg}.

Histograms of only 10 seconds of data at each V_{lg} were analyzed rather than histograms of entire data sets to eliminate the effects of shifts in V_{lg} over time, due to electrode contamination for example. At V_{lg} from -0.35 V to -0.13 V, there were no events in $I_{sd}(t)$ and the corresponding histograms were accurately fit with a single Gaussian. At V_{lg} from -0.1 V to 0.11 V, histograms of effective liquid gate voltage were properly fit by a double Gaussian function. The average event amplitude expressed as effective gating, measured as the difference of Gaussian peak positions, described in §4.5 Signal Analysis and Event Characterization, was ΔV_{lg} = -16 mV ± 8 mV for V_{lg} = 0.02 V for example. For V_{lg} from 0.14 V to 0.2 V, the histograms of effective liquid gate voltage were not accurately fit with single nor double Gaussian functions. As such, an accurate value of average event amplitude could not be generated for measurements at V_{lg} = 0.14 V and greater.

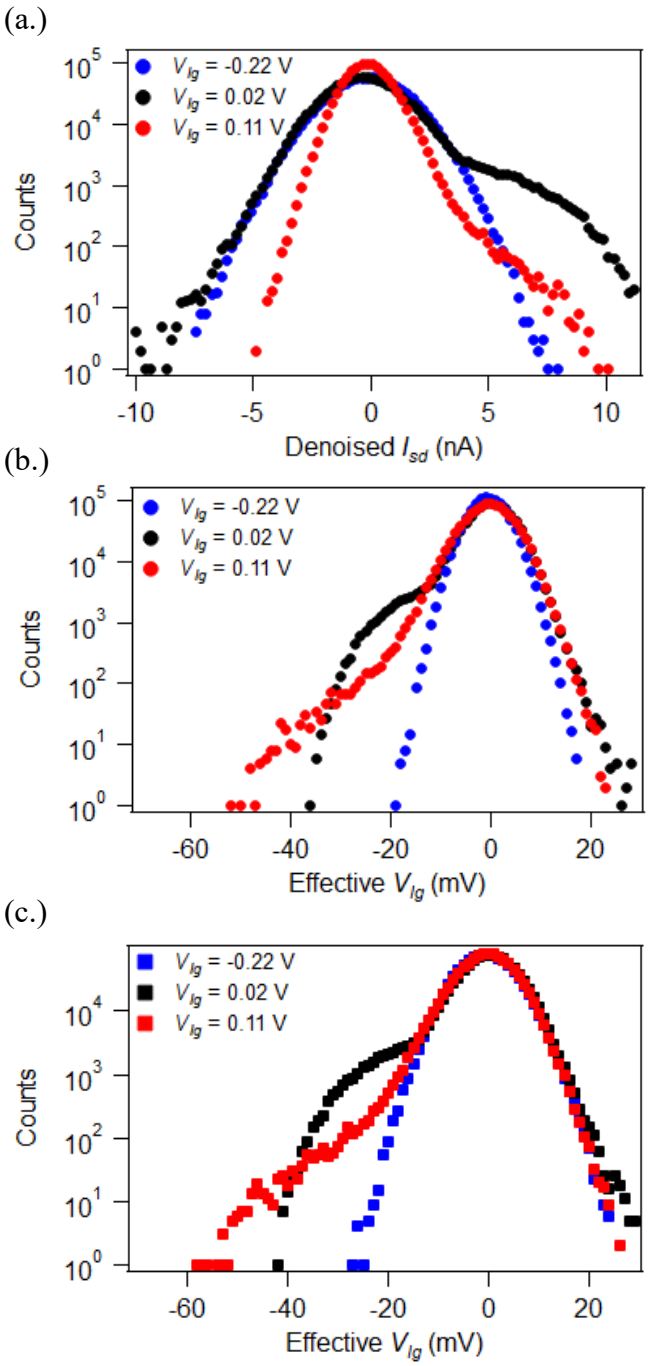

Figure 5.2: Histograms of (a.) denoised I_{sd} and effective V_{lg} (b.) before and (c.) after FWHM normalization for data acquired at V_{lg} = -0.22 V, 0.02 V and 0.11 V.

For histograms that could be properly fit with a single or double Gaussian, average event amplitudes expressed as effective gating for each V_{lg} are given in **Table 5.1**. Uncertainty in average

event amplitude was calculated as the sum of standard deviations of Gaussian peaks. For distributions described by a single Gaussian function, the lack of a second peak indicated no detectable events by amplitude, resulting in $\Delta V_{lg} = 0$. At liquid potentials from -0.1 V to 0.11 V, double Gaussian fits produced consistent average event amplitudes of ΔV_{lg} = -13 mV ± 9 mV; these liquid potentials defined the range of active V_{lg} where $|\Delta V_{lg}| > 0$ V. Additionally, the single polarity of the signal across changing liquid potentials was evidence that the events do not follow the behavior of a thermally activated fluctuator. An average event amplitude was not generated for liquid potentials from 0.14 V to 0.2 V due to the lack of proper Gaussian fitting.

Liquid Gate Voltage, V_{lg}	Average Event Amplitude, ΔV_{lg}	Liquid Gate Voltage, V_{lg}	Average Event Amplitude, ΔV_{lg}
-0.35 V	0 mV ± 3 mV	-0.01 V	-13 mV ± 6 mV
-0.25 V	0 mV ± 3 mV	0.02 V	-16 mV ± 8 mV
-0.22 V	0 mV ± 3 mV	0.05 V	-13 mV ± 9 mV
-0.19 V	0 mV ± 3 mV	0.08 V	-14 mV ± 9 mV
-0.16 V	0 mV ± 3 mV	0.11 V	-12 mV ± 5 mV
-0.13 V	0 mV ± 3 mV	0.14 V	N/A
-0.10 V	-10 mV ± 5 mV	0.17 V	N/A
-0.07 V	-12 mV ± 5 mV	0.20 V	N/A
-0.04 V	-12 mV ± 5 mV		

Table 5.1: Average event amplitude, ΔV_{lg}, at each TIP measured. The double Gaussian fit failed for liquid potentials from 0.14 V to 0.2 V and therefore was unable to produce a value for ΔV_{lg}. The uncertainty is expressed as the sum of standard deviations of the two Gaussian peaks.

Another metric of activity used for comparison was event rate over time and average event rate. At each V_{lg}, events were enumerated in each second for 10 seconds of data then averaged. **Figure 5.3** shows the average event rate in events per second in the presence of polyT_{42} and dATPs plotted against V_{lg}. The dotted line is the maximum event rate extracted from $I_{sd}(t)$ in buffer alone, 5 events per second, where a low number of events were still detected because of either anomalous excursions or artifacts of denoising and/or event recognition. Events occurring at a rate below this threshold were therefore not significant and not indicative of catalytic activity for this device. From this analysis, events occurred at an average rate greater than the threshold only in the range of V_{lg}

from -0.04 V to 0.14 V, which defined a slightly different range of active V_{lg} than the analysis of average event amplitudes. Within this active V_{lg} range, there was large variation in event rates, ranging from 5 to 50 events per second. Outside of the range of active V_{lg}, the average event rate, or rather the lack thereof, indicated no catalytic activity. This suggested that applied potentials outside of the range of active V_{lg} inhibited the Taq polymerase molecule from performing proper catalysis.

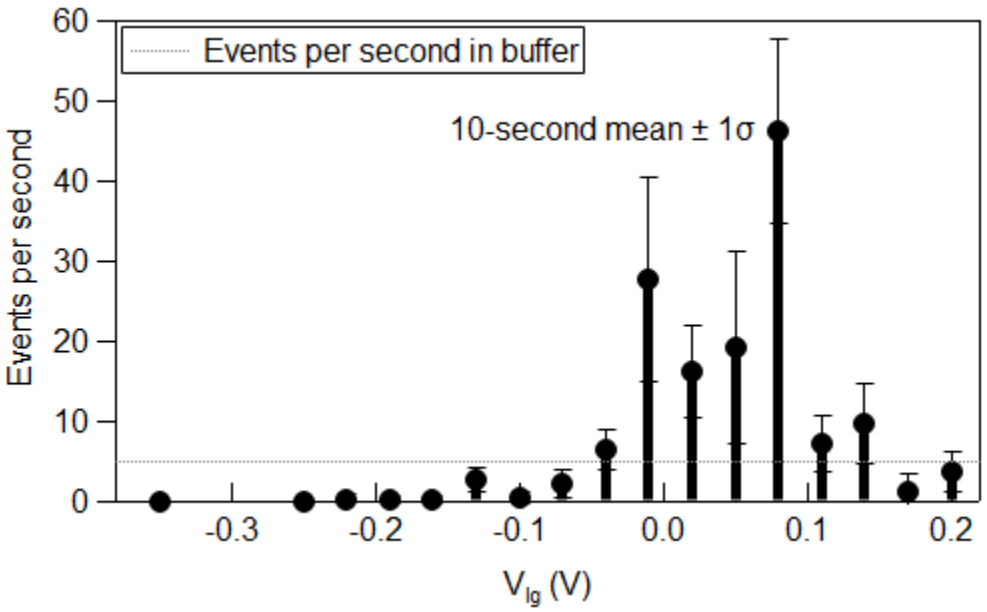

Figure 5.3: Average event rate versus liquid potential in the presence of 4nM polyT_{42} and 400nM dATP in Taq activity buffer. The number of events within each second of data is averaged over 10 seconds of data with error bars representing one standard deviation. The dotted line represents the maximum number of events detected with the same event detection algorithm in the absence of substrates.

The results of these two analyses provided sufficient evidence that the catalytic activity of Taq depended on applied potentials. The two analyses were independently able to define a range of active V_{lg}. Analysis of average event amplitudes defined a range of active V_{lg} from -0.1 V to

+0.11 V while analysis of event rates defined a range of active V_{lg} from -0.04 V to +0.14 V. While there was some disagreement between the analyses over the center of the range of active V_{lg}, they defined similar widths of 200 mV ± 30 mV. Average event amplitudes appeared to be consistent within the range of active V_{lg}. Because the amplitude of an event corresponds to the physical distance that nearby charged residues move during a conformational change, this result suggested that the detectable conformational change of the Taq molecule was consistent within the range of active V_{lg}. In other words, the applied potentials did not cause the Taq molecule to close tighter during its catalytic cycle. On the other hand, average event rates varied by an order of magnitude within the range of active V_{lg}. Past measurements in the Collins lab have shown that event rates vary by two orders of magnitude for a single polymerase molecule from second to second [170], so this variation is not surprising. However, it is currently unclear if this large variation was inherent to the protein or if it resulted from the applied potentials influencing catalytic activity.

5.2.2 Analyzing Signals with TIPs for Comparison to Signals with TVPs

Before applying TVPs, device PCB45-IG11de was biofunctionalized with A814C Taq polymerase and measured at TIPs ranging from -0.20 V to 0.20 V in buffer alone, then in the presence of 4 nM polyT$_{42}$ and 400 nM dATP. All measurements using PCB45-IG11de were performed at T = 27 °C. Characteristic traces of $I_{sd}(t)$ are shown in **Figure 5.4**. Once again, in the absence of substrates, $I_{sd}(t)$ was dominated by 1/f noise, as shown in **Fig. 5.4a**. Samples of $I_{sd}(t)$ in the presence of substrates are shown in **Fig. 5.4b** and **Fig. 5.4c**. Events again existed only in the presence of substrates, indicating catalytic motions of the protein, present only at V_{lg} from -0.11 V to 0.07 V.

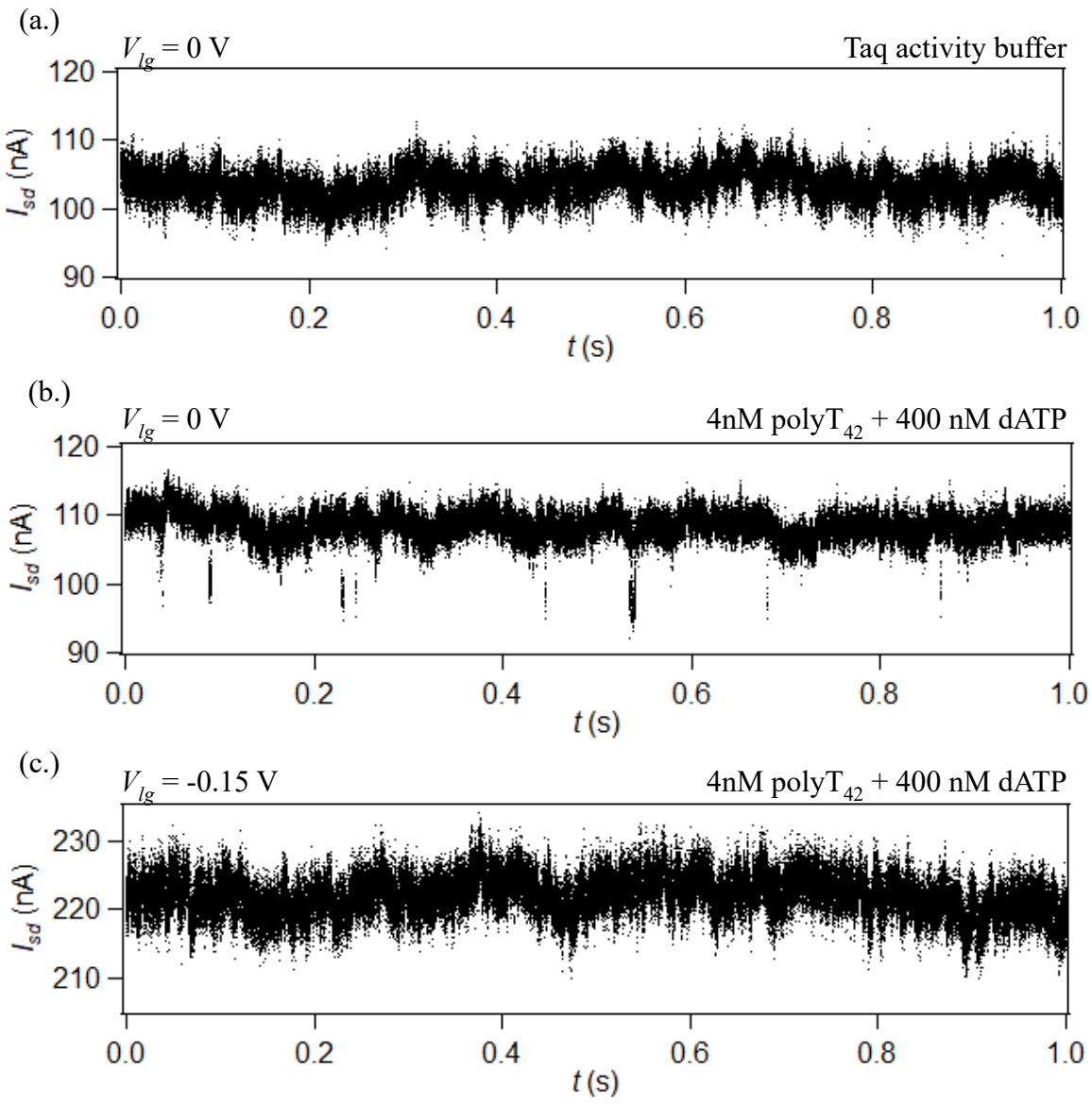

Figure 5.4: Sample $I_{sd}(t)$ data for measurements in (a.) Taq activity buffer at V_{lg} = 0 V, (b.) 4 nM polyT$_{42}$ + 400 nM dATP in Taq activity buffer at V_{lg} = 0 V, and (c.) 4 nM polyT$_{42}$ + 400 nM dATP in Taq activity buffer at V_{lg} = -0.15 V.

First, to establish a baseline for comparison of signals under TVPs, events observed under TIPs were analyzed further. Distributions of event dwell and waiting times were generated from $I_{sd}(t)$ data at V_{lg} = 0 V and are shown in **Figure 5.5**. The distribution of event dwell times was well

fit by a single exponential function except at longer time scales, which only accounted for a small fraction of all events. The single exponential fit of dwell times gave an average dwell time, τ_{dwell}, of 530 µs ± 30 µs. The distribution of event waiting times was fit primarily by a single exponential function, except for the first data point, which represented waiting times less than 20 ms. However, the first data point was anomalous as it resulted from artifacts of event recognition, where a single event was falsely recognized as two events resulting in a waiting time less than 20 ms, or an event that had intermediate returns to the baseline and was instead identified as multiple events with abnormally short waiting times. The single exponential fit of waiting times gave an average waiting time, $\tau_{waiting}$, of 260 ms ± 25 ms. The reciprocal of $\tau_{waiting}$ gave an average event rate of approximately 4 s^{-1}.

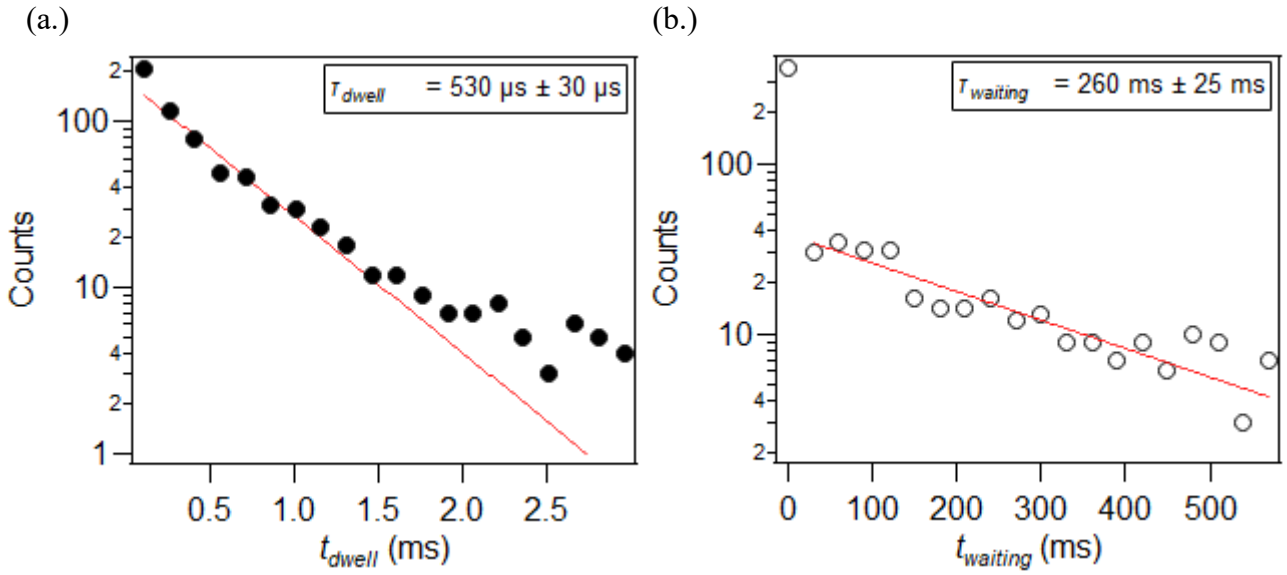

Figure 5.5: Distributions of (a.) t_{dwell} and (b.) $t_{waiting}$ with single exponential fits of the data overlaid and average times in the insets.

Next, events were enumerated in 50 ms segments of $I_{sd}(t)$ data at V_{lg} = 0 V, then compiled to determine probabilities of event occurrence. A histogram of events per 50 ms segment of data is shown in **Figure 5.6** and was also used as an example histogram in **Fig. 4.10**. The data points represent the probabilities determined from experimental data while the dashed line is the theoretical prediction for a Poisson process with an average rate of 4 s^{-1}—the average event rate determined from $\tau_{waiting}$. The error bars on the experimental data represent the variance of a Poisson-distributed variable. The majority of 50 ms frames had 0 events (87%), while a frame with 2 events was rare (<2%). However, the probability for a 50 ms frame to have a single event was approximately 11%, which was within uncertainty of a Poisson process with an average rate of 4 s^{-1} (16 % chance for one event to occur). Analysis of event occurrence probabilities further confirmed that the protein activity under TIPs observed was a Poisson process.

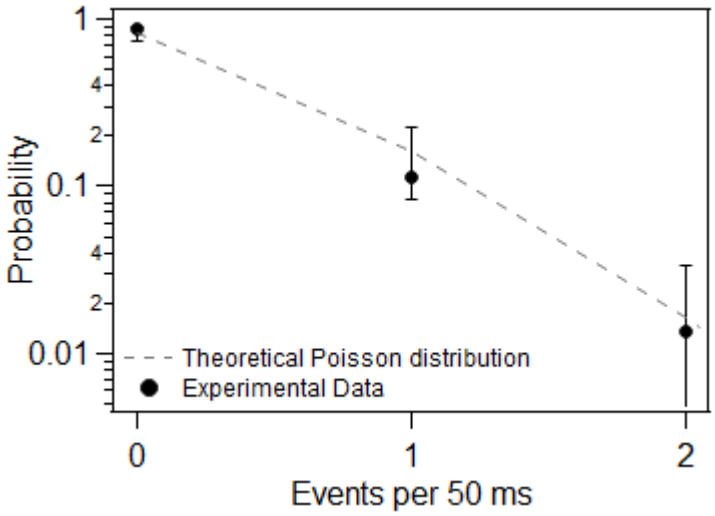

Figure 5.6: Probability for 0, 1 or 2 events to occur in a random 50 ms time frame.

To characterize the distribution of events in time more precisely, the distribution of event delay times, t_{delay}, for measurements at V_{lg} = 0 V are shown in **Figure 5.7**. Event delay times were measured as described in §4.5 Signal Analysis and Event Characterization. If there was a lack of

an event within the 100 ms time frame, no data point was generated. Error bars once again represent the variance of a Poisson-distributed variable. There was a total of 134 events in the data set analyzed. The delay times were evenly distributed, with events occurring randomly in 100 ms segments of data throughout the data set. In other words, when an event was present in a 100 ms segment of data, there was approximately a 10 % chance for the event to occur in any 10 ms subsegment of the 100 ms segment of data, once again indicating that the signal observed with TIPs is that of a Poisson process.

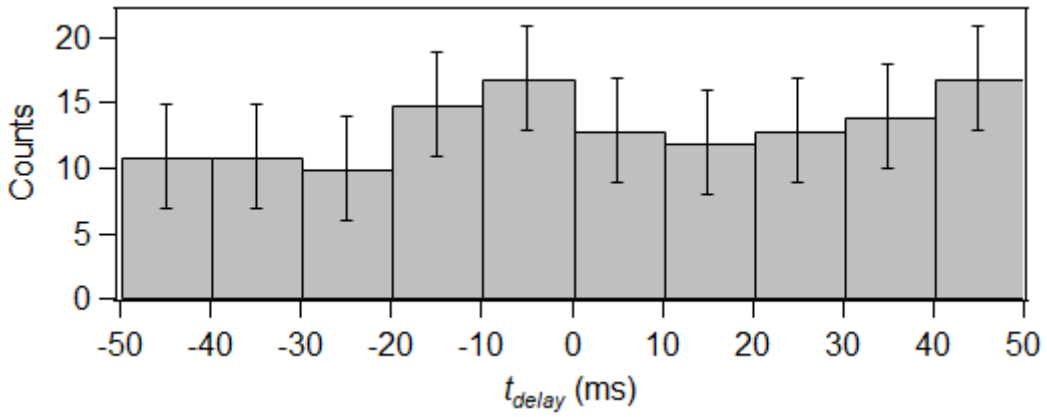

Figure 5.7: Distribution of t_{delay} for measurements at TIP V_{lg} = 0 V.

5.3 Taq Polymerase Activity Under Time-Varying Potentials

After measurements with TIPs revealed the range of active V_{lg}, TVPs were applied to device PCB45-IG11de. The TVPs that were applied to the counter electrode were 10 Hz square waves with boundaries: (i) [-0.2 V, 0 V], (ii) [-0.1 V, 0 V], (iii) [0 V, 0.1 V], and (iv) [0 V, 0.2 V]. **Figure 5.8** shows examples of $I_{sd}(t)$ with TVPs. In measurements with TVPs, nearly all events occurred while V_{lg} was within the active V_{lg} range (i.e. V_{lg} = -0.1 V or 0 V), showing that the catalytic activity of Taq polymerase could be toggled on and off by oscillating applied potentials

between active and inactive V_{lg}. There appeared to be three visually distinct types of events, hereafter referred to as Type 1, 2, and 3 events. A Type 1 event is shown in **Fig. 5.8a**, which had an event dwell time that follows the same Poisson statistics as events observed with TIPs. A Type 2 event, shown in **Fig. 5.8b**, also had an event dwell time in agreement with events observed with TIPs but coincided with the leading edge of a square wave half-cycle. Lastly, a Type 3 event began in one state of the square wave and ended in the other with an abnormally long dwell time, as shown in **Fig. 5.8c**. This is the only situation where an event occurred at an 'inactive' V_{lg}.

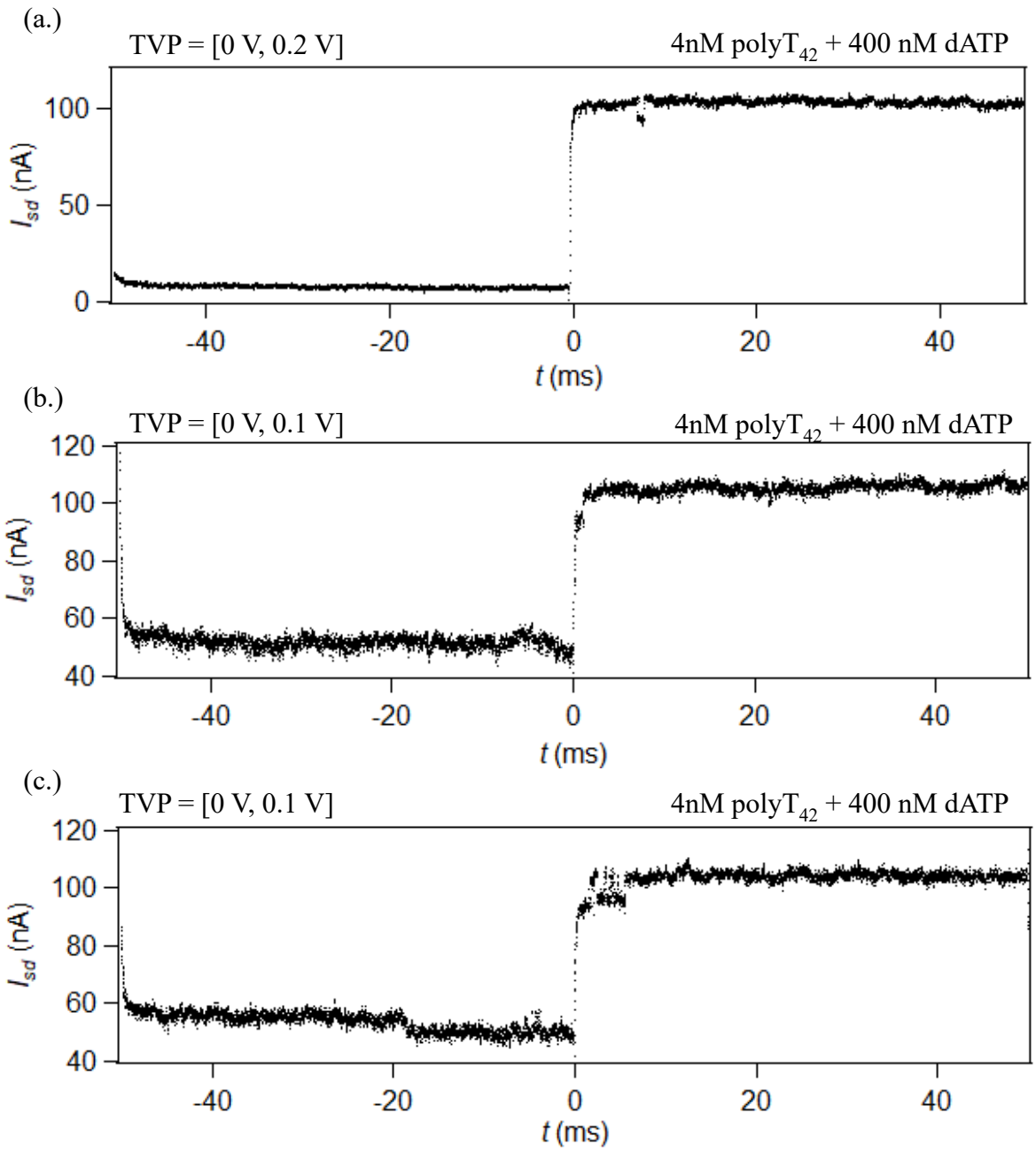

Figure 5.8: Samples of $I_{sd}(t)$ data in 4 nM polyT$_{42}$ + 400 nM dATP in Taq activity buffer under TVPs as annotated, exemplifying (a.) Type 1, (b.) Type 2, and (c.) Type 3 events.

Table 5.2 shows the number of occurrences in 38 seconds of data of each event type for all four TVP data sets as well as the earlier measurement with V_{lg} held constant at 0 V. When V_{lg} was held constant at 0 V, all events were Type 1. TVP = [-0.2 V, 0 V] and TVP = [-0.1 V, 0 V]

data both contained exclusively Type 1 events. Both Type 1 and Type 2 events were present in TVP = [0 V, 0.2 V] data, accounting for 56 % and 44 % of all events, respectively. All three event types were present in TVP = [0 V, 0.1 V] data, though the majority of events, 65%, were Type 1 events.

	Type 1 Events	Type 2 Events	Type 3 Events	Total Number of Events
0 V	134	0	0	**134**
[-0.2 V, 0 V]	51	0	0	**51**
[-0.1 V, 0 V]	56	0	0	**56**
[0 V, 0.1 V]	42	9	13	**64**
[0 V, 0.2 V]	59	46	0	**105**

Table 5.2: Total number of events and enumeration of each event type under different applied potentials.

The existence and abnormally long dwell times of Type 3 events in the TVP = [0 V, 0.1 V] dataset suggested that the TVP affected the energy landscape of the Taq polymerase molecule in a more complex way than simply enabling and disabling catalytic activity. The long dwell time of Type 3 events may have resulted from an increase in the energy barrier between conformational states and/or a deepening of the local energy minima corresponding to the closed state, effectively requiring the Taq molecule to overcome a greater energy barrier to return to its open conformation. Because Type 3 events always began in the V_{lg} = 0.1 V state of the TVP, the shift in energy landscape likely occurred in this state of the TVP, but reverted upon the return to V_{lg} = 0 V.

The existence of Type 2 events also indicated a more complex effect of TVPs, particularly in the case of TVP = [0 V, 0.2 V]. While it is possible that an event may have naturally coincided with the edge of a square wave, the high rate of synchronization, 44 %, was likely indicative of a reproducible mechanism rather than random coincidence. For example, it is possible that the large and abrupt change in V_{lg} from 0.2 V to 0 V momentarily reduced or eliminated the energy barrier for conformational change, effectively increasing the likelihood for an event to occur at that specific moment in time. Additionally, the prevalence of Type 2 events was greatest for TVP = [0 V, 0.2 V], indicating that this effect was dependent on the amplitude and polarity of TVP.

5.3.1 Event Characterization of Signals with Time-Varying Potentials

Event occurrence probabilities were extracted from $I_{sd}(t)$ data with applied TVPs. Because the TVPs were all applied at 10 Hz, enumerating events in 50 ms segments of data was equivalent to enumerating events in half-cycles of the TVP. In general, there were no events when the square wave was at the 'inactive' V_{lg} of its cycle ($V_{lg} \neq 0$ V or -0.1 V), so the probabilities for 1 or 2 events to occur were zero during those times. However, when the square wave was at the active V_{lg} (V_{lg} = 0 V or -0.1 V), there was a nonzero probability for 1 or 2 events to occur within each half-cycle. The probabilities for 0, 1 or 2 events to occur per 50 ms half-cycle when V_{lg} = 0 V were calculated from experimental data for each TVP and are shown in **Figure 5.9**. For three of the four TVPs, experimental probabilities for all numbers of occurrences were within one σ of the respective theoretical values as well as experimental values for the TIP. Only measurements using TVP = [0 V, 0.2 V] had probabilities that deviated significantly from Poisson statistics. The probability for one event to occur in the V_{lg} = 0 V half-cycle, 24 %, was greater than one standard deviation above the theoretical value for a Poisson process, 16 %. This suggests that the applied TVP = [0 V, 0.2

V] altered the energy landscape of the Taq molecule in a way that the catalytic conformational change was more energetically favorable than under TIPs. Interestingly, the large total number of events using TVP = [0 V, 0.2 V], relative to the other TVPs, was not also reflected in the probability for two events to occur, indicating that Type 1 and Type 2 events generally did not *both* occur in a single half-cycle.

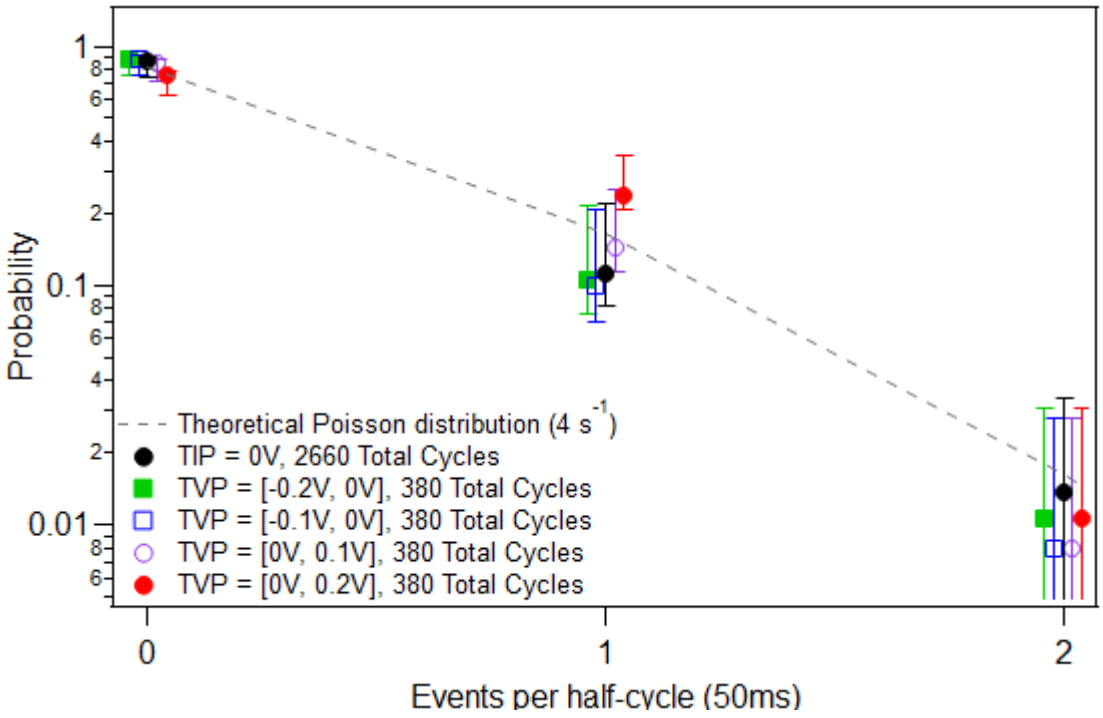

Figure 5.9: Probability for 0, 1, or 2 events to occur in a 50 ms segment of data with V_{lg} = 0 V. Experimental data is shown as black circles (TIP = 0 V), green squares (TVP = [-0.2 V, 0 V]), blue squares (TVP = [-0.1 V, 0 V]), purple circles (TVP = [0 V, 0.1 V]), and red circles (TVP = [0 V, 0.2 V]) while the theoretical Poisson distribution is shown as a dashed line.

To further describe the effect of TVPs, distributions of events in time were also evaluated in each data set for Type 1 events only. **Figure 5.10** depicts the distributions of t_{delay} throughout each of the four TVP measurements. Because the TVPs were applied at 10 Hz, t_{delay} was measured

from the leading edge of the V_{lg} = 0 V half-cycle of the square wave for all applied signals, which conveniently corresponded to the center of the 100 ms segment of data as indicated in **Fig. 5.10a**. The distributions of delay times are shown in **Fig. 5.10b, c, d,** and **e**. The distribution of events in time for TVP = [-0.2 V, 0 V], TVP = [-0.1 V, 0 V], and TVP = [0 V, 0.1 V] were consistent with a Poisson process within uncertainty, and therefore consistent with data using TIPs. Alternatively, for TVP = [0 V, 0.2 V], Type 1 events did not occur randomly in time and instead were more likely to occur within 20 ms of the square wave transition. The effect of this applied TVP was further evidenced by the prevalence of Type 2 events (see **Table 5.2**), accounting for approximately 40% of all events.

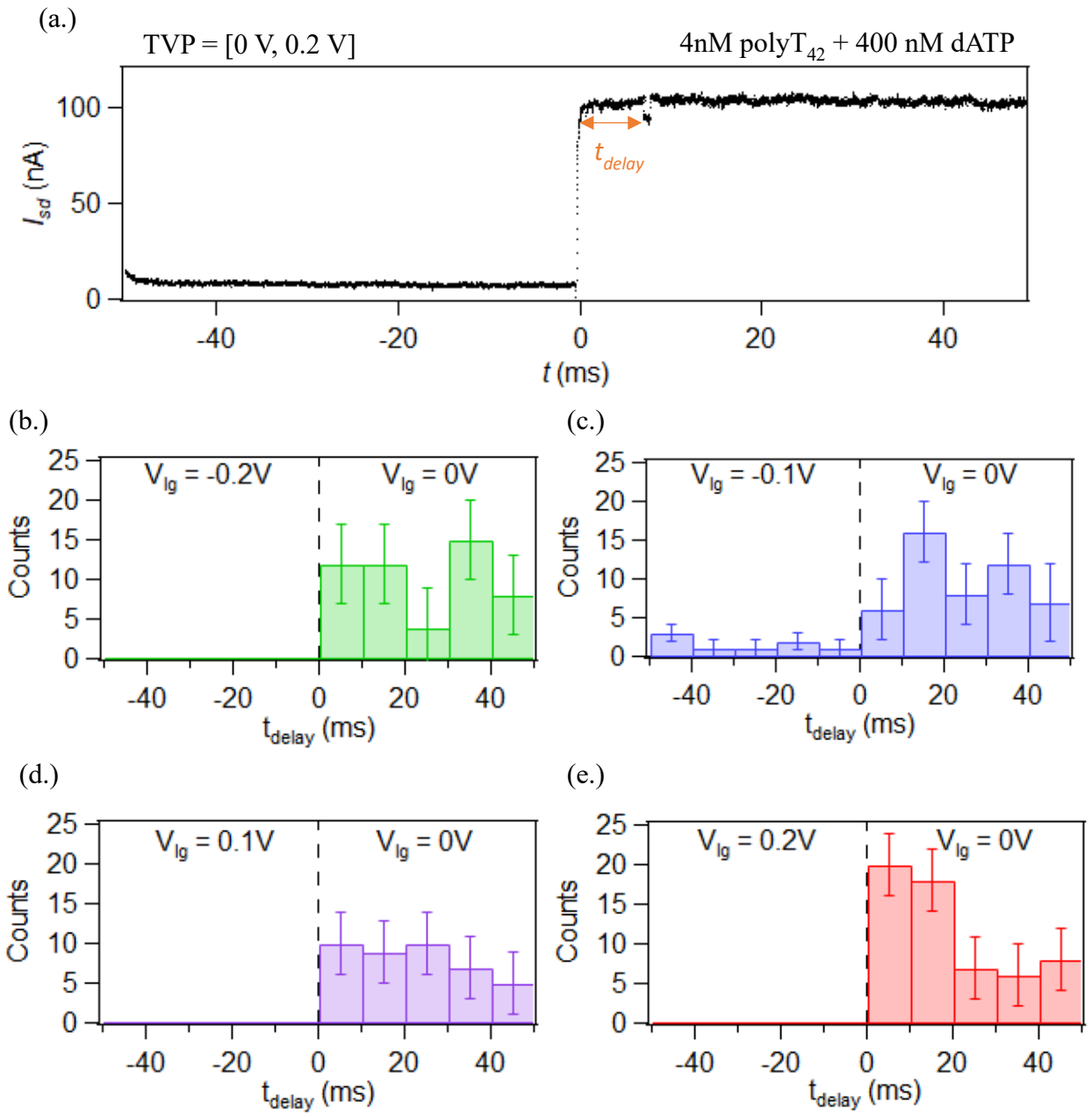

Figure 5.10: (a.) Example of t_{delay}. Distribution of t_{delay} for (b.) TVP = [-0.2 V, 0 V], (c.) TVP = [-0.1 V, 0 V], (d.) TVP = [0 V, 0.1 V] and (e.) TVP = [0 V, 0.2 V].

From the results of the different analyses, TVP = [-0.2 V, 0 V] and TVP = [-0.1 V, 0 V] did not perturb the Taq molecule in a way that significantly differed from TIPs, as evidenced by all of the above analyses. Events were all Type 1 events occurring in 50 ms time frames with

probabilities well described by a theoretical Poisson process, as well as occurring randomly in time, which is also expected for a Poisson process.

On the other hand, TVP = [0 V, 0.1 V] and TVP = [0 V, 0.2 V] both appeared to perturb the timing of Taq's catalytic closures. TVP = [0 V, 0.1 V] affected the event dwell time most clearly, as evidenced by the existence of Type 3 events. However, TVP = [0 V, 0.2 V] influenced all metrics that were examined. Approximately 44 % of all events with applied TVP = [0 V, 0.2 V] were Type 2 events and the existence of these events did not appear to come at the expense of Type 1 events. The probability for one event of either type to occur in a single V_{lg} = 0 V half-cycle with TVP = [0 V, 0.2 V] was 50 % greater than with TIP = 0 V or the theoretical prediction for a Poisson process. Additionally, Type 1 events were more than twice as likely to occur within the first 20 ms of the V_{lg} = 0 V half-cycle than in the final 30 ms, indicating that the square wave transition edge was a significant choice of reference point for evaluating t_{delay}. One possible explanation for the TVP = [0 V, 0.2 V] is that the enzyme may be electrostatically forced closed at V_{lg} = 0.2 V, effectively resetting Taq's catalytic 'clock' at the transition to V_{lg} = 0 V. This would explain the biased distribution of delay times with respect to the square wave transition edge, as t_{delay} would effectively represent $t_{waiting}$ in this case. Additionally, Type 2 events may simply result from the enzyme waiting to reopen upon the liquid potential transition, which would explain why they have dwell times consistent with Type 1 events.

5.4 Conclusions and Future Work

Measurements of Taq polymerase with applied TIPs confirmed past observations of the Collins lab – that individual molecules are sensitive to applied potentials. More precisely, applied potentials enabled and disabled Taq's catalysis and a range of active V_{lg} was defined as a result.

Within the range of active V_{lg}, the average event amplitude remained constant (see **Table 5.1**), indicating that the applied potentials did not affect the detectable physical movement resulting from conformational changes. On the other hand, the average event rate varied from 5 s^{-1} to 50 s^{-1} within the range of active V_{lg} (See **Fig. 5.3**), though this large variance is not necessarily due to the applied potentials as rates associated with individual molecules have been observed to vary by two orders of magnitude from second-to-second.

Measurements using TVPs revealed even more complex effects of applied potentials. First, Taq activity was successfully toggled on and off by oscillating applied potentials in and out of the range of active V_{lg}. The existence of Type 2 and Type 3 events (see **Fig. 5.8** and **Table 5.2**) indicated that the applied TVPs affected the energy landscape of the Taq molecules in ways that are more complex than simply enabling and disabling catalysis. Further analysis of event occurrence probabilities and distribution of events in time revealed that TVP = [0 V, 0.2 V] also disturbed the natural Poisson-like behavior of Taq's catalysis (see **Fig. 5.9** and **Fig. 5.10**), increasing the likelihood of events to occur in general, and more specifically within 20 ms of the square wave transition. Results with multiple applied TVPs showed that the polarity and amplitude of TVPs are critical parameters in influencing the Taq molecule.

This work was able to explore the effects of applied potentials, both constant and time-varying, with the greatest detail thus far but also revealed effects that warrant further experimentation. This work gave early evidence of possible synchronization (Type 2 events) and dwell time disturbance (Type 3 events) with applied potentials, so future work and applications of these results would benefit by optimizing frequency, amplitude, and polarity of TVPs for better control of the molecules' activity.

REFERENCES

[1] Schultz, J. S., Taylor, R. F. Handbook of Chemical and Biological Sensors. (1996).

[2] Mehrotra, P. Biosensors and their applications - A review. *J. Oral Biol. Craniofacial Res.* **6**, 153–159 (2016).

[3] Vigneshvar, S., Sudhakumari, C. C., Senthilkumaran, B. & Prakash, H. Recent advances in biosensor technology for potential applications - an overview. *Front. Bioeng. Biotechnol.* **4**, 1–9 (2016).

[4] Wang, J., Chen, G., Jiang, H., Li, Z. & Wang, X. Advances in nano-scaled biosensors for biomedical applications. *Analyst* **138**, 4427–4435 (2013).

[5] Shi, W., Friedman, A. K. & Baker, L. A. Nanopore Sensing. *Anal. Chem.* **89**, 157–188 (2017).

[6] Dias, A. D., Kingsley, D. M. & Corr, D. T. Recent advances in bioprinting and applications for biosensing. *Biosensors* **4**, 111–136 (2014).

[7] Miyazaki, C. M., Shimizu, F. M. & Ferreira, M. *Surface Plasmon Resonance (SPR) for Sensors and Biosensors*. *Nanocharacterization Techniques* (Elsevier Inc., 2017).

[8] Liao, C., Li, Y. & Tjong, S. C. Graphene nanomaterials: Synthesis, biocompatibility, and cytotoxicity. *Int. J. Mol. Sci.* **19**, (2018).

[9] Lerner, M. B. *et al.* Large scale commercial fabrication of high quality graphene-based assays for biomolecule detection. *Sensors Actuators, B Chem.* **239**, 1261–1267 (2017).

[10] Fang, Y. & Wang, E. Electrochemical biosensors on platforms of graphene. *Chem. Commun.* **49**, 9526–9539 (2013).

[11] Zhang, M. *et al.* Highly sensitive glucose sensors based on enzyme-modified whole-graphene solution-gated transistors. *Sci. Rep.* **5**, 1–6 (2015).

[12] Goldsmith, B. R. *et al.* Digital Biosensing by Foundry-Fabricated Graphene Sensors. *Sci. Rep.* **9**, 1–10 (2019).

[13] Janegitz, B. C. *et al.* The application of graphene for in vitro and in vivo electrochemical biosensing. *Biosens. Bioelectron.* **89**, 224–233 (2017).

[14] Hajian, R. *et al.* Detection of unamplified target genes via CRISPR–Cas9 immobilized on a graphene field-effect transistor. *Nat. Biomed. Eng.* **3**, 427–437 (2019).

[15] Afsahi, S. *et al.* Novel graphene-based biosensor for early detection of Zika virus infection. *Biosens. Bioelectron.* **100**, 85–88 (2018).

[16] Peña-Bahamonde, J., Nguyen, H. N., Fanourakis, S. K. & Rodrigues, D. F. Recent advances in graphene-based biosensor technology with applications in life sciences. *J. Nanobiotechnology* **16**, 1–17 (2018).

[17] Chen, D., Tang, L. & Li, J. Graphene-based materials in electrochemistry. *Chem. Soc. Rev.* **39**, 3157–3180 (2010).

[18] Joo, C., Balci, H., Ishitsuka, Y., Buranachai, C. & Ha, T. Advances in single-molecule fluorescence methods for molecular biology. *Annu. Rev. Biochem.* **77**, 51–76 (2008).

[19] Neuman, K. C. & Nagy, A. Single-molecule force spectroscopy: Optical tweezers, magnetic tweezers and atomic force microscopy. *Nat. Methods* **5**, 491–505 (2008).

[20] Collins, P. G., Bradley, K., Ishigami, M. & Zettl, A. Extreme oxygen sensitivity of electronic properties of carbon nanotubes. *Science (80-.).* **287**, 1801–1804 (2000).

[21] Goldsmith, B. R., Coroneus, J. G., Kane, A. A., Weiss, G. A. & Collins, P. G. Monitoring single-molecule reactivity on a carbon nanotube. *Nano Lett.* **8**, 189–194 (2008).

[22] Sorgenfrei, S. & Shepard, K. L. Label-free field-effect-based single-molecule detection of DNA hybridization kinetics. *Nat. Nanotechnol.* **6**, 126–132 (2011).

[23] Besteman, K., Lee, J., Wiertz, F. G. M., Heering, H. A. & Dekker, C. Enzyme-Coated Carbon Nanotubes as Single-Molecule Biosensors. *Nano Lett.* **3**, 727–730 (2003).

[24] Olsen, T. J. *et al.* Electronic measurements of single-molecule processing by DNA polymerase I (Klenow fragment). *J. Am. Chem. Soc.* **135**, 7855–7860 (2013).

[25] Sims, P. C. *et al.* Electronic measurements of single-molecule catalysis by cAMP-dependent protein kinase A. *J. Am. Chem. Soc.* **135**, 7861–7868 (2013).

[26] Choi, Y. *et al.* Single-Molecule Lysozyme Dynamics. *Science* **335**, 319–325 (2012).

[27] Warshel, A. & Levitt, M. Theoretical studies of enzymic reactions: Dielectric, electrostatic and steric stabilization of the carbonium ion in the reaction of lysozyme. *J. Mol. Biol.* **103**, 227–249 (1976).

[28] Warshel, A. Energetics of enzyme catalysis. *Proc. Natl. Acad. Sci. U. S. A.* **75**, 5250–5254 (1978).

[29] Warshel, A. *et al.* Electrostatic basis for enzyme catalysis. *Chem. Rev.* **106**, 3210–3235 (2006).

[30] Tsong, T. Y., Liu, D. S., Chauvin, F., Gaigalas, A. & Dean Astumian, R. Electroconformational coupling (ECC): an electric field induced enzyme oscillation for cellular energy and signal transductions. *J. Electroanal. Chem.* **275**, 319–331 (1989).

[31] Matthew, J. B. Electrostatic Effects In Proteins. *J. Chromatogr. Libr.* **40**, 55–75 (1988).

[32] Mehler, E. L. & Solmajer, T. Electrostatic effects in proteins: Comparison of dielectric and charge models. *Protein Eng. Des. Sel.* **4**, 903–910 (1991).

[33] Feierberg, I. & Åqvist, J. The catalytic power of ketosteroid isomerase investigated by computer simulation. *Biochemistry* **41**, 15728–15735 (2002).

[34] Fried, S. D. & Boxer, S. G. Electric fields and enzyme catalysis. *Annu. Rev. Biochem.* **86**, 387–415 (2017).

[35] Prah, A., Frančišković, E., Mavri, J. & Stare, J. Electrostatics as the Driving Force behind the Catalytic Function of the Monoamine Oxidase A Enzyme Confirmed by Quantum Computations. *ACS Catal.* **9**, 1231–1240 (2019).

[36] Lai, W., Chen, H., Cho, K. Bin & Shaik, S. External electric field can control the catalytic cycle of cytochrome P450cam: A QM/MM study. *J. Phys. Chem. Lett.* **1**, 2082–2087 (2010).

[37] Ciampi, S., Darwish, N., Aitken, H. M., Díez-Perez, I. & Coote, M. L. Harnessing electrostatic catalysis in single molecule, electrochemical and chemical systems: a rapidly growing experimental tool box. *Chem. Soc. Rev.* **47**, 5146–5164 (2018).

[38] Shaik, S., Ramanan, R., Danovich, D. & Mandal, D. Structure and reactivity/selectivity control by oriented-external electric fields. *Chem. Soc. Rev.* **47**, 5125–5145 (2018).

[39] Vaissier, V., Sharma, S. C., Schaettle, K., Zhang, T. & Head-Gordon, T. Computational Optimization of Electric Fields for Improving Catalysis of a Designed Kemp Eliminase. *ACS Catal.* **8**, 219–227 (2018).

[40] Fu, W. *et al.* Graphene transistors are insensitive to pH changes in solution. *Nano Lett.* **11**, 3597–3600 (2011).

[41] Radić, Z., Kirchhoff, P. D., Quinn, D. M., McCammon, J. A. & Taylor, P. Electrostatic influence on the kinetics of ligand binding to acetylcholinesterase: Distinctions between active center ligands and fasciculin. *J. Biol. Chem.* **272**, 23265–23277 (1997).

[42] Dell'Orco, D., Xue, W. F., Thulin, E. & Linse, S. Electrostatic contributions to the kinetics and thermodynamics of protein assembly. *Biophys. J.* **88**, 1991–2002 (2005).

[43] Vainrub, A. & Pettitt, B. M. Surface electrostatic effects in oligonucleotide microarrays: Control and optimization of binding thermodynamics. *Biopolymers* **68**, 265–270 (2003).

[44] Erbaş, A., De La Cruz, M. O. & Marko, J. F. Effects of electrostatic interactions on ligand dissociation kinetics. *Phys. Rev. E* **97**, 1–12 (2018).

[45] Bergveld, P. Thirty years of ISFETOLOGY: What happened in the past 30 years and what may happen in the next 30 years. *Sensors Actuators, B Chem.* **88**, 1–20 (2003).

[46] Pachauri, V. & Ingebrandt, S. Biologically sensitive field-effect transistors: From ISFETs to NanoFETs. *Essays Biochem.* **60**, 81–90 (2016).

[47] Xia, J., Chen, F., Li, J. & Tao, N. Measurement of the quantum capacitance of graphene. *Nat. Nanotechnol.* **4**, 505–509 (2009).

[48] Uesugi, E., Goto, H., Eguchi, R., Fujiwara, A. & Kubozono, Y. Electric double-layer capacitance between an ionic liquid and few-layer graphene. *Sci. Rep.* **3**, 1–5 (2013).

[49] Mailly-Giacchetti, B. *et al.* PH sensing properties of graphene solution-gated field-effect transistors. *J. Appl. Phys.* **114**, (2013).

[50] Akhterov, M. V. Microsecond Dynamics of Enzymes: A Single-Molecule Study Using Carbon Nanotube Transistors. (2015). University of California, Irvine, Ph.D. dissertation.

[51] Jakobson, C. G., Feinsod, M. & Nemirovsky, Y. Low frequency noise and drift in Ion Sensitive Field Effect Transistors. *Sensors Actuators, B Chem.* **68**, 134–139 (2000).

[52] Chou, J. C. & Wang, Y. F. Preparation and study on the drift and hysteresis properties of the tin oxide gate ISFET by the sol-gel method. *Sensors Actuators, B Chem.* **86**, 58–62 (2002).

[53] Rispens, T. *et al.* Label-free assessment of high-affinity antibody-antigen binding constants. Comparison of bioassay, SPR, and PEIA-ellipsometry. *J. Immunol. Methods* **365**, 50–57 (2011).

[54] Rees, H. A. & Liu, D. R. Base editing: precision chemistry on the genome and transcriptome of living cells. *Nat. Rev. Genet.* **19**, 770–788 (2018).

[55] Landrum, M. J. et al. ClinVar: public archive of relationships among sequence variation and human phenotype. *Nucleic Acids Res.* **42**, D980–D985 (2013).

[56] Landrum, M. J. et al. ClinVar: public archive of interpretations of clinically relevant variants. *Nucleic Acids Res.* **44**, D862–D868 (2015).

[57] Hawn, T. R. et al. Toll-like receptor polymorphisms and susceptibility to urinary tract infections in adult women. *PLoS ONE* **4**, e5990 (2009).

[58] Johnson, C. M. et al. Cutting edge: a common polymorphism impairs cell surface trafficking and functional responses of TLR1 but protects against leprosy. *J. Immunol.* **178**, 7520–7524 (2007).

[59] Sironi, M. et al. A common polymorphism in *TLR3* confers natural resistance to HIV-1 infection. *J. Immunol.* **188**, 818–823 (2012).

[60] Pagliai, G. et al. *CLOCK* gene polymorphisms and quality of aging in a cohort of nonagenarians—The MUGELLO Study. *Sci. Rep.* **9**, 1472 (2019).

[61] Yang, C.-H., Cheng, Y.-H., Chuang, L.-Y. & Chang, H.-W. Drug-SNPing: an integrated drug-based, protein interaction-based tagSNP-based pharmacogenomics platform for SNP genotyping. *Bioinformatics* **29**, 758–764 (2013).

[62] Alwi, Z. B. The use of SNPs in pharmacogenomics studies. *Malays. J. Med. Sci.* **12**, 4–12 (2005).

[63] McCarthy, J. J. & Hilfiker, R. The use of single-nucleotide polymorphism maps in pharmacogenomics. *Nat. Biotechnol.* **18**, 505–508 (2000).

[64] Chagné, D. et al. Validation of SNP markers for fruit quality and disease resistance loci in apple (*Malus* × *domestica* Borkh.) using the OpenArray® platform. *Horticulture Res.* **6**, 30 (2019).

[65] Kennedy, R. B. et al. Genetic polymorphisms associated with rubella virus-specific cellular immunity following MMR vaccination. *Hum. Genet.* **133**, 1407–1417 (2014).

[66] Dhiman, N. et al. SNP/haplotype associations in cytokine and cytokine receptor genes and immunity to rubella vaccine. *Immunogenetics* **62**, 197–210 (2010).

[67] He, J. et al. Association of SARS susceptibility with single nucleic acid polymorphisms of *OAS1* and *MxA* genes: a case-control study. *BMC Infect. Dis.* **6**, 106 (2006).

[68] Gralinski, L. E. et al. Genome wide identification of SARS-CoV susceptibility loci using the collaborative cross. *PLoS Genet.* **11**, e1005504 (2015).

[69] Itoyama, S. et al. ACE1 polymorphism and progression of SARS. *Biochem. Biophys. Res. Commun.* **323**, 1124–1129 (2004).

[70] Guan, Y. et al. Isolation and characterization of viruses related to the SARS coronavirus from animals in Southern China. *Science* **302**, 276–278 (2003).

[71] Kan, B. et al. Molecular evolution analysis and geographic investigation of severe acute respiratory syndrome coronavirus-like virus in palm civets at an animal market and on farms. *J. Virol.* **79**, 11892–11900 (2005).

[72] Gisler, F. M., von Kanel, T., Kraemer, R., Schaller, A. & Gallati, S. Identification of SNPs in the cystic fibrosis interactome influencing pulmonary progression in cystic fibrosis. *Eur. J. Hum. Genet.* **21**, 397–403 (2013).

[73] Williams, L. M. & Oleksiak, M. F. Ecologically and evolutionarily important SNPs identified in natural populations. *Mol. Biol. Evol.* **28**, 1817–1826 (2011).

[74] López-García, M. A. et al. Influence of genetic variants of CYP2D6, CYP2C9, CYP2C19 and CYP3A4 on antiepileptic drug metabolism in pediatric patients with refractory epilepsy. *Pharmacol. Rep.* **69**, 504–511 (2017).

[75] Barilli, E. et al. A high-density integrated DArTseq SNP-based genetic map of *Pisum fulvum* and identification of QTLs controlling rust resistance. *Front. Plant Sci.* **9**, 167 (2018).

[76] Zhang, T. et al. Identification of molecular markers associated with verticillium wilt resistance in alfalfa (*Medicago Sativa* L.) using high-resolution melting. *PLoS ONE* **9**, e115953 (2014).

[77] Rey, T. et al. The Medicago truncatula GRAS protein RAD1 supports arbuscular mycorrhiza symbiosis and *Phytophthora palmivora* susceptibility. *J. Exp. Bot.* **68**, 5871–5881 (2017).

[78] Ben Ali, S.-E. et al. Mutation scanning in a single and a stacked genetically modified (GM) 0event by real-time PCR and high resolution melting (HRM) analysis. *Int. J. Mol. Sci.* **15**, 19898–19923 (2014).

[79] Gunderson, K. L., Steemers, F. J., Lee, G., Mendoza, L. G. & Chee, M. S. A genome-wide scalable SNP genotyping assay using microarray technology. *Nat. Genet.* **37**, 549–554 (2005).

[80] Yamamoto, G. et al. Highly sensitive method for genomewide detection of allelic composition in nonpaired, primary tumor specimens by use of affymetrix single-nucleotide-polymorphism genotyping microarrays. *Am. J. Hum. Genet.* **81**, 114–126 (2007).

[81] Gaedigk, A. et al. SNP genotyping using TaqMan® technology: the *CYP2D6*17* assay conundrum. *Sci. Rep.* **5**, 9257 (2015).

[82] Borodina, T. A., Lehrach, H. & Soldatov, A. V. Ligation detection reaction-TaqMan procedure for single nucleotide polymorphism detection on genomic DNA. *Anal. Biochem.* **333**, 309–319 (2004).

[83] Ramos, A. M. et al. Design of a high density SNP genotyping assay in the pig using SNPs identified and characterized by next generation sequencing technology. *PLoS ONE* **4**, e6524 (2009).

[84] Boyle, E. A. et al. High-throughput biochemical profiling reveals sequence determinants of dCas9 off-target binding and unbinding. *Proc. Natl Acad. Sci. USA* **114**, 5461–5466 (2017).

[85] Anders, C., Niewoehner, O., Duerst, A. & Jinek, M. Structural basis of PAM-dependent target DNA recognition by the Cas9 endonuclease. *Nature* **513**, 569–573 (2014).

[86] Josephs, E. A. et al. Structure and specificity of the RNA-guided endonuclease Cas9 during DNA interrogation, target binding and cleavage. *Nucleic Acids Res.* **43**, 8924–8941 (2015).

[87] Pattanayak, V. et al. High-throughput profiling of off-target DNA cleavage reveals RNA-programmed Cas9 nuclease specificity. *Nat. Biotechnol.* **31**, 839–843 (2013).

[88] Qi, L. S. et al. Repurposing CRISPR as an RNA-guided platform for sequence-specific control of gene expression. *Cell* **152**, 1173–1183 (2013).

[89] Zhao, C., Shu, X. & Sun, B. Construction of a gene knockdown system based on catalytically inactive ("dead") Cas9 (dCas9) in *Staphylococcus aureus*. *Appl. Environ. Microbiol.* **83**, e00291-17 (2017).

[90] Sternberg, S. H., Redding, S., Jinek, M., Greene, E. C. & Doudna, J. A. DNA interrogation by the CRISPR RNA-guided endonuclease Cas9. *Nature* **507**, 62–67 (2014).

[91] Chatterjee, P., Jakimo, N. & Jacobson, J. M.Minimal PAM specificity of a highly similar SpCas9 ortholog. *Sci. Adv.* **4**, eaau0766 (2018).

[92] Chen, J. S. et al. Enhanced proofreading governs CRISPR–Cas9 targeting accuracy. *Nature* **550**, 407–410 (2017).

[93] Kleinstiver, B. P. et al. High-fidelity CRISPR–Cas9 variants with undetectable genome-wide off-targets. *Nature* **529**, 490–495 (2016).

[94] Slaymaker, I. M. et al. Rationally engineered Cas9 nucleases with improved specificity. *Science* **351**, 84–88 (2016).

[95] Zhang, D. et al. Perfectly matched 20-nucleotide guide RNA sequences enable robust genome editing using high-fidelity SpCas9 nucleases. *Genome Biol.* **18**, 191 (2017).

[96] Vakulskas, C. A. et al. A high-fidelity Cas9 mutant delivered as a ribonucleoprotein complex enables efficient gene editing in human hematopoietic stem and progenitor cells. *Nat. Med.* **24**, 1216–1224 (2018).

[97] Cai, L. et al. A universal approach to correct various *HBB* gene mutations in human stem cells for gene therapy of beta-thalassemia and sickle cell disease. *Stem Cells Transl. Med.* **7**, 87–97 (2017).

[98] Eaton, W. A. Hemoglobin S polymerization and sickle cell disease: a retrospective on the occasion of the 70th anniversary of Pauling's *Science* paper. *Am. J. Hematol.* **95**, 205–211 (2020).

[99] Papageorgiou, D. P. et al. Simultaneous polymerization and adhesion under hypoxia in sickle cell disease. *Proc. Natl Acad. Sci. USA* **115**, 9473–9478 (2018).

[100] Sachdev, V., Rosing, D. R. & Thein, S. L. Cardiovascular complications of sickle cell disease. *Trends Cardiovasc. Med.* (2020).

[101] Piel, F. B., Steinberg, M. H. & Rees, D. C. Sickle cell disease. *N. Engl. J. Med.* **376**, 1561–1573 (2017).

[102] Quinn, C. T., Rogers, Z. R., McCavit, T. L. & Buchanan, G. R.Improved survival of children and adolescents with sickle cell disease. *Blood* **115**, 3447–3452 (2010).

[103] Gong, L., Parikh, S., Rosenthal, P. J. & Greenhouse, B. Biochemical and immunological mechanisms by which sickle cell trait protects against malaria. *Malar. J.* **12**, 317 (2013).

[104] Robberecht, W. & Philips, T. The changing scene of amyotrophic lateral sclerosis. *Nat. Rev. Neurosci.* **14**, 248–264 (2013).

[105] Al-Chalabi, A. et al. The genetics and neuropathology of amyotrophic lateral sclerosis. *Acta Neuropathol.* **124**, 339–352 (2012).

[106] Borchelt, D. R. et al. Superoxide dismutase 1 with mutations linked to familial amyotrophic lateral sclerosis possesses significant activity. *Proc. Natl Acad. Sci. USA* **91**, 8292–8296 (1994).

[107] Nordlund, A. et al. Functional features cause misfolding of the ALS-provoking enzyme SOD1. *Proc. Natl Acad. Sci. USA* **106**, 9667–9672 (2009).

[108] Pattabhi, S. et al. In vivo outcome of homology-directed repair at the *HBB* gene in HSC using alternative donor template delivery methods. *Mol. Ther. Nucleic Acids* **17**, 277–288 (2019).

[109] Dever, D. P. et al. CRISPR/Cas9 β-globin gene targeting in human hematopoietic stem cells. *Nature* **539**, 384–389 (2016).

[110] Park, S. H. et al. Highly efficient editing of the β-globin gene in patient-derived hematopoietic stem and progenitor cells to treat sickle cell disease. *Nucleic Acids Res.* **47**, 7955–7972 (2019).

[111] Duan, W. et al. The deletion of mutant SOD1 via CRISPR/Cas9/sgRNA prolongs survival in an amyotrophic lateral sclerosis mouse model. *Gene Ther.* **27**, 157–169 (2020).

[112] Gaj, T. et al. In vivo genome editing improves motor function and extends survival in a mouse model of ALS. *Sci. Adv.* **3**, eaar3952 (2017).

[113] Aryal, N. K., Wasylishen, A. R. & Lozano, G. CRISPR/Cas9 can mediate high-efficiency off-target mutations in mice in vivo. *Cell Death Dis.* **9**, 1099 (2018).

[114] Cho, S. W. et al. Analysis of off-target effects of CRISPR/Cas-derived RNA-guided endonucleases and nickases. *Genome Res.* **24**, 132–141 (2014).

[115] DeWitt, M. A. et al. Selection-free genome editing of the sickle mutation in human adult hematopoietic stem/progenitor cells. *Sci. Transl. Med.* **8**, 360ra134 (2016).

[116] Bowden, R. et al. Sequencing of human genomes with nanopore technology. *Nat. Commun.* **10**, 1869 (2019).

[117] Hwang, M. T. et al. Highly specific SNP detection using 2D graphene electronics and DNA strand displacement. *Proc. Natl Acad. Sci. USA* **113**, 7088–7093 (2016).

[118] Bialk, P. et al. Analyses of point mutation repair and allelic heterogeneity generated by CRISPR/Cas9 and single-stranded DNA oligonucleotides. *Sci. Rep.* **6**, 32681 (2016).

[119] Daer, R. M., Cutts, J. P., Brafman, D. A. & Haynes, K. A. The impact of chromatin dynamics on Cas9-mediated genome editing in human cells. *ACS Synth. Biol.* **6**, 428–438 (2017).

[120] Everaerts, F., Torrianni, M., Hendriks, M. & Feijen, J. Biomechanical properties of carbodiimidecrosslinked collagen: influence of the formation of ester crosslinks. *J Biomed Mater Res A* **85**, 547–555 (2008).

[121] Wang, C., Yan, Q., Liu, H.-B., Zhou, X.-H. & Xiao, S.-J. Different EDC/NHS Activation Mechanismsbetween PAA and PMAA Brushes and the Following Amidation Reactions. *Langmuir* **27**, 12058–12068 (2011).

[122] Sadlowski, C. et al. Graphene-based biosensor for on-chip detection of bio-orthogonally labeled proteins to identify the circulating biomarkers of aging during heterochronic parabiosis. *Lab Chip* **18**, 3230–3238 (2018).

[123] Wickramathilaka, M. P. & Tao, B. Y. Characterization of covalent crosslinking strategies for synthesizing DNA-based bioconjugates. *J. Biol. Eng.* **13**, 63 (2019).

[124] Riquelme, M. V. et al. Optimizing blocking of nonspecific bacterial attachment to impedimetric biosensors. *Sens. Biosensing Res.* **8**, 47–54 (2016).

[125] Singh, D., Sternberg, S. H., Fei, J., Doudna, J. A. & Ha, T. Real-time observation of DNA recognition and rejection by the RNA-guided endonuclease Cas9. *Nat. Commun.* **7**, 12778 (2016).

[126] Knight, S. C. et al. Dynamics of CRISPR–Cas9 genome interrogation in living cells. *Science* **350**, 823–826 (2015).

[127] Yang, M. et al. The conformational dynamics of Cas9 governing DNA cleavage are revealed by single-molecule FRET. *Cell Rep.* **22**, 372–382 (2018).

[128] Jinek, M. et al. A programmable dual RNA-guided DNA endonuclease in adaptive bacterial immunity. *Science* **337**, 816–821 (2012).

[129] Amrani, N. et al. NmeCas9 is an intrinsically high-fidelity genome-editing platform. *Genome Biol.* **19**, 214 (2018).

[130] Harrington, L. B. et al. A thermostable Cas9 with increased lifetime in human plasma. *Nat. Commun.* **8**, 1424 (2017).

[131] Hu, Z. et al. A compact Cas9 ortholog from *Staphylococcus auricularis* (SauriCas9) expands the DNA targeting scope. *PLoS Biol.* **18**, e3000686 (2020).

[132] D'Agata, R. et al. Direct detection of point mutations in nonamplified human genomic DNA. *Anal. Chem.* **83**, 8711–8717 (2011).

[133] Rosen, D. R. et al. Mutations in Cu/Zn superoxide dismutase gene are associated with familial amyotrophic lateral sclerosis. *Nature* **362**, 59–62 (1993).

[134] Cong, L. et al. Multiplex genome engineering using CRISPR/Cas systems. *Science* **339**, 819–823 (2013).

[135] Ran, F. A. et al. Genome engineering using the CRISPR–Cas9 system. *Nat. Protoc.* **8**, 2281–2308 (2013).

[136] Yang, Z., Edwards, H. & Xu, P. CRISPR–Cas12a/Cpf1-assisted precise, efficient and multiplexed genome-editing in *Yarrowia lipolytica*. *Metab. Eng. Commun.* **10**, e00112 (2020).

[137] Abudayyeh, O. O. et al. C2c2 is a single-component programmable RNA-guided RNA-targeting CRISPR effector. *Science* **353**, aaf5573 (2016).

[138] Gootenberg, J. S. et al. Nucleic acid detection with CRISPR–Cas13a/C2c2. *Science* **356**, 438–442 (2017).

[139] Gasiunas, G., Barrangou, R., Horvath, P. & Siksnys, V. Cas9–crRNA ribonucleoprotein complex mediates specific DNA cleavage for adaptive immunity in bacteria. *Proc. Natl Acad. Sci. USA* **109**, E2579 (2012).

[140] Gasiunas, G. et al. A catalogue of biochemically diverse CRISPR–Cas9 orthologs. *Nat. Commun.* **11**, 5512 (2020).

[141] Povedano, E. et al. Electrochemical affinity biosensors for fast detection of gene-specific methylations with no need for bisulfite and amplification treatments. *Sci. Rep.* **8**, 6418 (2018).

[142] Rauf, S. et al. Carboxylic group riched graphene oxide based disposable electrochemical immunosensor for cancer biomarker detection. *Anal. Biochem.* **545**, 13–19 (2018).

[143] Guo, L. et al. Colorimetric biosensor for the assay of paraoxon in environmental water samples based on the iodine-starch color reaction. *Anal. Chim. Acta* **967**, 59–63 (2017).

[144] Lang, Q., Han, L., Hou, C., Wang, F. & Liu, A. A sensitive acetylcholinesterase biosensor based on gold nanorods modified electrode for detection of organophosphate pesticide. *Talanta* **156–157**, 34–41 (2016).

[145] Greig, D. R., Jenkins, C., Gharbia, S. & Dallman, T. J.Comparison of single-nucleotide variants identified by Illumina and Oxford Nanopore technologies in the context of a potential outbreak of Shiga toxin-producing *Escherichia coli*. *GigaScience* **8**, giz104 (2019).

[146] Caputo, T. M., Battista, E., Netti, P. A. & Causa, F. Supramolecular microgels with molecular beacons at the interface for ultrasensitive, amplification-free, and SNP-selective miRNA fluorescence detection. *ACS Appl. Mater. Interfaces* **11**, 17147–17156 (2019).

[147] Yang, Z. et al. An amplification-free detection method of nucleic acids by a molecular beacon probe based on endonuclease activity. *Sens. Actuators B* **298**, 126901 (2019).

[148] Gilpatrick, T. et al. Targeted nanopore sequencing with Cas9-guided adapter ligation. *Nat. Biotechnol.* **38**, 433–438 (2020).

[149] Walton, R. T., Christie, K. A., Whittaker, M. N. & Kleinstiver, B. P. Unconstrained genome targeting with near-PAMless engineered CRISPR– Cas9 variants. *Science* **368**, 290–296 (2020).

[150] Martel, R., Schmidt, T., Shea, H. R., Hertel, T. & Avouris, P. Single- and multi-wall carbon nanotube field- effect transistors. *Appl. Phys. Lett.* **73**, 2447–2449 (1998).

[151] Tans, S. J., Verschueren, A. R. M. & Dekker, C. Room-temperature transistor based on a single carbon nanotube. *Nature* **393**, 49–52 (1998).

[152] Kong, J. *et al.* Nanotube molecular wires as chemical sensors. *Science* **287**, 622–625 (2000).

[153] Heller, I. *et al.* Identifying the mechanism of biosensing with carbon nanotube transistors. *Nano Lett.* **8**, 591–595 (2008).

[154] Goldsmith, B. R. *et al.* Conductance-Controlled Point Functionalization of Single-Walled Carbon Nanotubes. *Science* **315**, 77–81 (2007).

[155] Debye, P. & Hückel E. Zur Theorie der Elektrolyte. *Physikalische Zeitschrift* **9**, 185-206 (1923).

[156] Sorgenfrei, S., Chiu, C. Y., Johnston, M., Nuckolls, C. & Shepard, K. L. Debye screening in single-molecule carbon nanotube field-effect sensors. *Nano Lett.* **11**, 3739–3743 (2011).

[157] Stern, E. *et al.* Importance of the debye screening length on nanowire field effect transistor sensors. *Nano Lett.* **7**, 3405–3409 (2007).

[158] Heller, I. *et al.* Influence of electrolyte composition on liquid-gated carbon nanotube and graphene transistors. *J. Am. Chem. Soc.* **132**, 17149–17156 (2010).

[159] Müller, A. *et al.* Generation of cluster capsules (I_h) from decomposition products of a smaller cluster (Keggin-T_d) while surviving ones get encapsulated: Species with core-shell topology formed by a fundamental symmetry-driven reaction. *Chem. Commun.* 657–658 (2001).

[160] An, L., Owens, J. M., McNeil, L. E. & Liu, J. Synthesis of nearly uniform single-walled carbon nanotubes using identical metal-containing molecular nanoclusters as catalysts. *J. Am. Chem. Soc.* **124**, 13688–13689 (2002).

[161] Hunter, C. A. & Sanders, J. K. M. The Nature of π-π Interactions. *J. Am. Chem. Soc.* **112**, 5525–5534 (1990).

[162] Hermanson, G. *Bioconjugate Techniques*, Academic Press, 1195 p. (2008).

[163] Kim, Y. *et al.* Efficient site-specific labeling of proteins via cysteines. *Bioconjug. Chem.* **19**, 786–791 (2008).

[164] Koniev, O. & Wagner, A. Developments and recent advancements in the field of endogenous amino acid selective bond forming reactions for bioconjugation. *Chem. Soc. Rev.* **44**, 5495–5551 (2015).

[165] Collins, P. G., Fuhrer, M. S. & Zettl, A. 1/f noise in carbon nanotubes. *Appl. Phys. Lett.* **76**, 894–896 (2000).

[166] Johnson, K. The kinetic and chemical mechanism of high-fidelity DNA polymerases. *Biochim Biophys Acta* **1804**, 1041–1048 (2010).

[167] Reuel, N. F. *et al.* NoRSE: Noise reduction and state evaluator for high-frequency single event traces. *Bioinformatics* **28**, 296–297 (2012).

[168] Tobias, D. *et al.* Origins of 1/*f* noise in individual semiconducting carbon nanotube field-effect transistors. *Phys. Rev. B - Condens. Matter Mater. Phys.* **77**, 1–4 (2008).

[169] Männik, J., Heller, I., Janssens, A. M., Lemay, S. G. & Dekker, C. Charge noise in liquid-gated single-wall carbon nanotube transistors. *Nano Lett.* **8**, 685–688 (2008).

[170] Lau, C. Single-Molecule Studies of Biomolecules as Molecular Machines. (2020). University of California, Irvine, Ph.D. dissertation.

[171] Turvey, M. W. Single-Molecule, Variable-Temperature Electronic Measurements of Taq DNA Polymerase Using Carbon Nanotube Transistors. (2020). University of California, Irvine, Ph.D. dissertation.

[172] Eisenmesser, E. Z., Bosco, D. A., Akke, M. & Kern, D. Enzyme Dynamics During Catalysis. *Science (80-.).* **295**, 1520–1524 (2002).

[173] Blomberg, C. Fluctuations for good and bad: The role of noise in living systems. *Phys. Life Rev.* **3**, 133–161 (2006).

[174] Henzler-Wildman, K. A. *et al.* Intrinsic motions along an enzymatic reaction trajectory. *Nature* **450**, 838–844 (2007).

[175] McNamara, B. & Wiesenfeld, K. Theory of stochastic resonance. *Phys. Rev. A* **39**, 4854–4869 (1989).

[176] Gammaitoni, L., Hanggi, P., Jung, P. & Marchesoni, F. Stochastic resonance with a mixture of sub-and supra-threshold stimuli in a population of neuron models. *Proc. Annu. Int. Conf. IEEE Eng. Med. Biol. Soc. EMBS* **70**, 7328–7331 (2011).

[177] Schmitt, C., Dybiec, B., Hänggi, P. & Bechinger, C. Stochastic resonance vs. resonant activation. *Europhys. Lett.* **74**, 937–943 (2006).

[178] Grifoni, M. & Hänggi, P. Coherent and incoherent quantum stochastic resonance. *Phys. Rev. Lett.* **76**, 1611–1614 (1996).

[179] McDonnell, M. D. & Abbott, D. What is stochastic resonance? Definitions, misconceptions, debates, and its relevance to biology. *PLoS Comput. Biol.* **5**, (2009).

[180] Hayashi, K., de Lorenzo, S., Manosas, M., Huguet, J. M. & Ritort, F. Single-molecule stochastic resonance. *Phys. Rev. X* **2**, 1–11 (2012).

[181] Franco, E. *et al.* Timing molecular motion and production with a synthetic transcriptional clock. *Proc. Natl. Acad. Sci. U. S. A.* **108**, (2011).

[182] Robertson, B. & Astumian, R. D. Michaelis-Menten equation for an enzyme in an oscillating electric field. *Biophys. J.* **58**, 969–974 (1990).

[183] Magdy, T., Kuo, H. & Burridge, P. W. Precise and Cost-Effective Nanopore Sequencing for Post-GWAS Fine-Mapping and Causal Variant Identification. *iScience* **23**, 100971 (2020).

[184] Wu, L. *et al.* Amplification-free SERS analysis of DNA mutation in cancer cells with single-base sensitivity. *Nanoscale* **11**, 7781–7789 (2019).

APPENDIX A

Supplemental SNP-Chip Data[2]

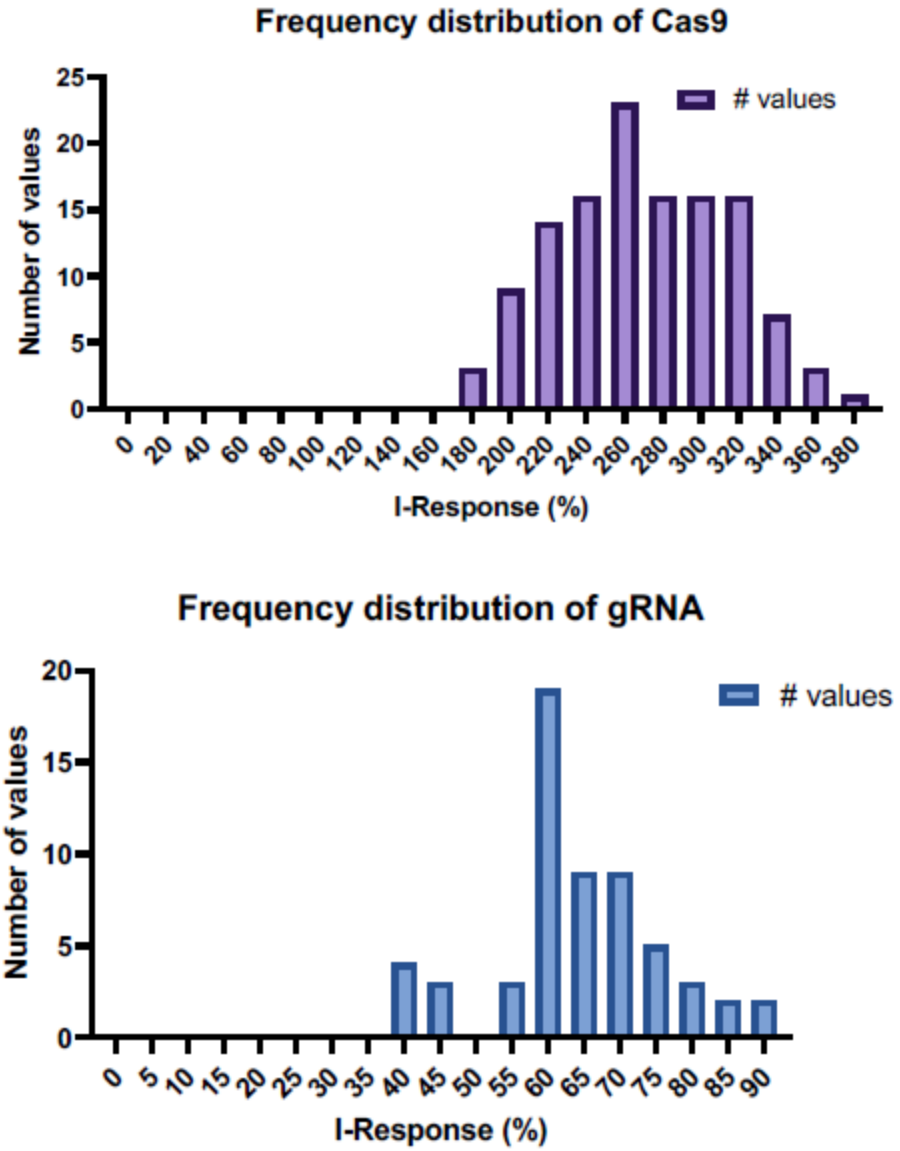

Figure A.1: Frequency distribution of signal obtained from Cas9 and gRNA association on gFET. The distribution of signal of Cas9 binding (top) and the gRNA-HTYa binding (bottom).

[2] Reprinted with permission from "Discrimination of Single-Point Mutations in Unamplified Genomic DNA via Cas9 Immobilized on a Graphene Field-Effect Transistor" by S. Balderston, J. Taulbee, E. Celaya, et al. *Nature Biomedical Engineering* (2021). Copyright, Springer Nature.

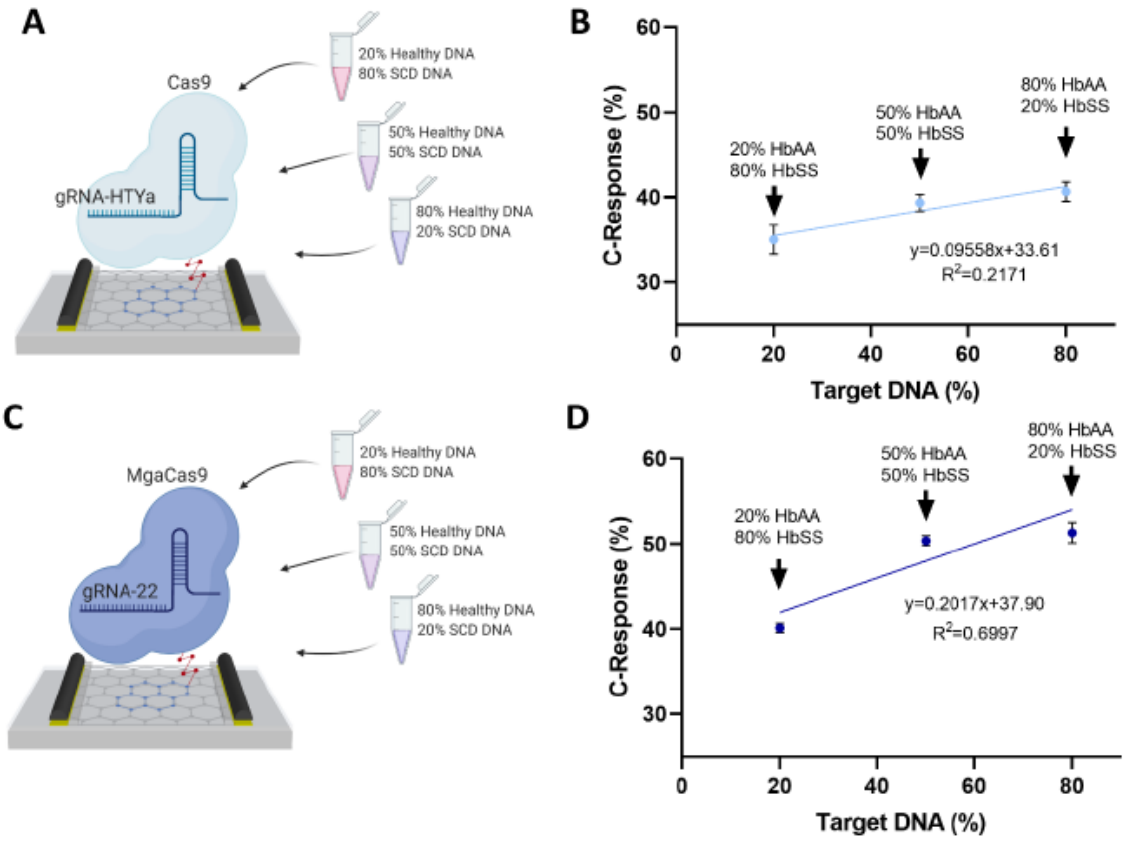

Figure A.2: SNP-Chip Cas9-HTYa Specificity. (**a**) Schematic of the specificity test where the nuclease active Cas9-HTYa construct was incubated with non-homogeneous DNA samples (60 ng μl^{-1}) containing different percentages of target DNA (HbAA) and nontarget DNA (HbSS). (**b**) Cas9-HTYa construct specificity and sensitivity endpoint analysis in the presence of different percentages of the target (HbAA) in a nontarget sample (HbSS). (**c**) Schematic of the specificity test where the MgaCas9-22nt gRNA construct was incubated with non-homogeneous DNA samples (60 ng μl^{-1}) containing different percentages of target DNA (HbAA) and nontarget DNA (HbSS). (**d**) MgaCas9-22nt gRNA construct specificity and sensitivity endpoint analysis in the presence of different percentages of the target (HbAA) in a nontarget sample (HbSS).

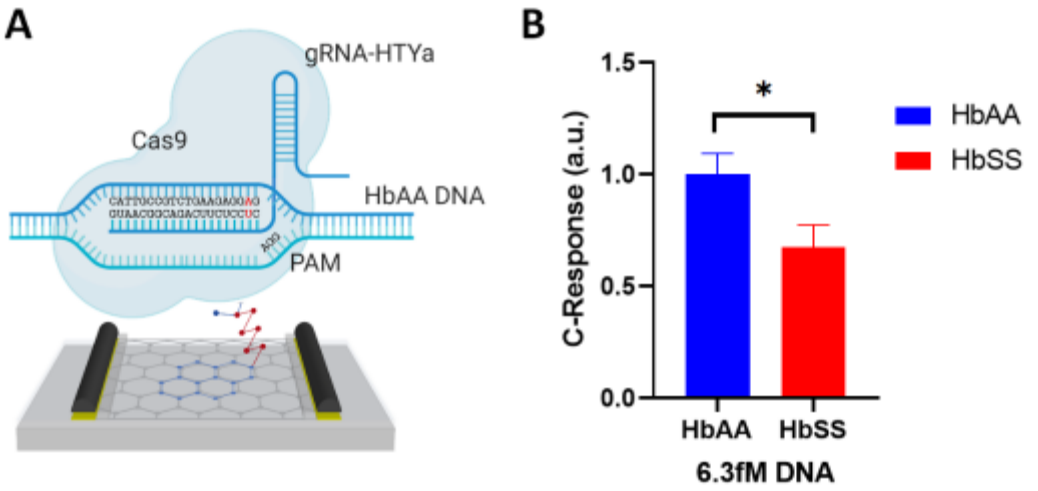

Figure A.3: (**a**) Schematic representation of the Cas9-HTYa SNP-Chip construct. (**b**) A concentration of 6.3 fM genomic DNA was tested on the Cas9-HTYa construct. Results indicated that that SNP-Chip was able to discriminate between HbAA and HbSS samples ($n \geq 9$) (ttest: $t = 2.337$, $df = 19$). Bar graph shows mean ± SEM. Data is normalized and presented as a ratio relative to the positive sample (HbAA). Significance is indicated by * for two-tailed $p < 0.05$.

	OXFORD NANOPORE	SNP-CHIP
SAMPLE PREPARATION	DNA Purification	DNA Purification
LIBRARY CONSTRUCTION	Yes	No
AMPLIFICATION	Yes (~8 PCR cycles) [116]	No
TIME TO SCAN HUMAN GENOME	48 Hours (8 readers) [116]	< 1 Hour (one reader)
HANDHELD	Yes	Yes
SNPS	Yes	Yes
TOTAL ANALYSIS TIME FOR WHOLE HUMAN GENOME SEQUENCING	> 83 Hours [116]	Few minutes
PRICE OF DISPOSABLES FOR WHOLE GENOME SEQUENCING	$28,000 (34 flow cells [116])	$40 (1 chip)
PRICE OF READER	$1,000	$400

Table A.1: Comparison between SNP-Chip and oxford nanopore single-nucleotide variation analysis time and cost. Although oxford nanopore has been used to detect SNPs in the bacterial genome and 100kb fragments of the human genome [145,183], these studies of nanopore SNP detection rely on smaller genomes (bacterial) or PCR-based amplification to simplify the DNA samples tested. This table compares SNP-Chip technology with oxford nanopore when employed to scan the entire human genome. Although the study referenced here still uses amplification, the purpose of amplification is library construction, not a simplification of the DNA sample.

	Highly specific SNP detection using 2D graphene electronics and DNA strand displacement [117]	Supramolecular Microgels with Molecular Beacons at the Interface for Ultrasensitive, Amplification-Free, and SNP-Selective miRNA Fluorescence Detection [146]	An amplification-free detection method of nucleic acids by a molecular beacon probe based on endonuclease activity [147]	Amplification-free SERS analysis of DNA mutation with single-base sensitivity [184]	SNP-Chip
TARGET	Oligo (47 nt)	ssDNA	E coli genomic DNA	Full genomic DNA (Human)	Full genomic DNA (Human)
TIME	8 hours	1 hour/ON	< 1 hour	40 min	1 hour
DETECTION	FET	Optical	Optical (Molecular Beacon)	Optical (SERS)	gFET
PRINCIPLE	Strand displacement competition	Hydrogel with molecular beacon	Endonuclease digestion upon beacon rearrangement with a perfect match	Beacon with nanogold particle monitored with SERS	CRISPR
SENSITIVITY	300 nM	12 fM/ON	1 pM	50 fM	6.3 fM

Table A.2: Comparison of SNP-sensitive DNA detection technologies. In the paper entitled "Highly specific SNP detection using 2D graphene electronics and DNA strand displacement" The principle is based on SNP detect on gFET using a probe/target DNA hybridization based on strand displacement to increase discrimination. The DNA probe is composed of two complementary DNA strands, one 47 nt, which is tether to the graphene surface via PBA and the other 40 nt. The difference of size (7 nt) constitutes the toehold that will allow the target DNA to initiate the hybridization. If no mismatches are present, the target will displace the competing strand more efficiently. In the presence of a SNP, this displacement is less efficient. There is big chance that their system won't work with double strand DNA. In the paper entitled "Supramolecular Microgels with Molecular Beacons at the Interface for Ultrasensitive, Amplification-Free, and SNP-Selective miRNA Fluorescence Detection" micro hydrogels, which are hydrogel layered over nanoparticles, are employed and functionalized with a molecular beacon (MB). SNP discrimination is standard in a MB. The mismatch is placed at the center of the probe. When the full match is present the MB open and fluoresces. When a mismatch is present, the MB open less frequently. The gel is used to increase the surface area ratio and decrease non-specific adsorption on surface. This technology requires a one-hour incubation for large quantities of DNA, but an overnight hybridization is required for concentration close to LOD. This technology uses miRNA, which are short single stranded nucleic acids. Long double strand amplicons will be more difficult to detect with this

technology. In the paper entitled “An amplification-free detection method of nucleic acids by a molecular beacon probe based on endonuclease activity” they use an endonuclease dependent molecular beacon assay (DEMBA) to detect SNPs. The beacon is designed to rearrange and create an endonuclease digestion site only when a full match target is present. Once digested, the fluorescent is released, and the target is freed, thus the target is available again to produce fluorescence (linear amplification). Although rapid and sensitive this technology is optical and can require bulky equipment, however the authors have attempted a lateral flow assay which has the potential to lower the cost of this technology. In the work entitled “Amplification-free SERS analysis of DNA mutation in cancer cells with single-base sensitivity” they use SERS to detect a gold particle that is pushed away from the surface when hybridized with a fully complimentary sample in a flow cell. This technology stated that detection time is 40 min, with an LOD of 50 fM with an overnight incubation. This is also a label free technology but using optics (SERS) instead of electronics which requires bulky instrumentation.